Patrycja K. Kruk

The role of astrocytic CD44 protein in epileptogenesis

Ph.D. thesis completed in
the Laboratory of Molecular and Systemic Neuromorphology
&
the Laboratory of Cell Biophysics
of the Nencki Institute of Experimental Biology
Polish Academy of Sciences

SUPERVISOR:
Dr hab. Joanna Dzwonek
Prof. Instytutu Nenckiego PAN

Warsaw, 2024

NATIONAL SCIENCE CENTRE
POLAND
2015/17/B/NZ4/02540

I would like to express my heartfelt gratitude to all those who have supported me throughout my PhD journey.

To Joanna Dzwonek, Ph.D., for her supervision and unwavering guidance, invaluable feedback, and encouragement. Your mentorship has been instrumental in shaping my research and academic growth.

To Prof. Grzegorz Wilczyński† & Prof. Jakub Włodarczyk, for providing a supportive and stimulating environment in which I could carry out my research. Your leadership and expertise were essential to the progress of my work.

To Małgorzata Śliwińska, Ph.D., who expertly conducted the electron microscopy imaging and was there to always lend a helping hand, and Christel Genoud, Ph.D. & Yannick Schwab, Ph.D., for generously sharing their knowledge of electron microscopy. Your insights and collaboration greatly enhanced the quality of this research.

To all members of the Laboratory of Molecular and Systemic Neuromorphology & the Laboratory of Cell Biophysics, for their invaluable support and teamwork. The stimulating atmosphere in both laboratories greatly contributed to my academic and personal growth, and I am grateful for the opportunity to work alongside such talented colleagues.

Mojej najbliższej rodzinie — Mamie i Siostrze — które swoją miłością, wsparciem i wiarą we mnie były stałym źródłem siły przez cały ten okres.

Moim przyjaciołom – Katarzynie Cieśluk i Michałowi Niziołkowi – za to, że zawsze byli przy mnie, oferując wsparcie emocjonalne i intelektualne, gdy najbardziej tego potrzebowałam.

Thank you All for your contributions to this work and for being part of this meaningful experience.

Lastly, I would also like to thank myself for not giving up. Instead of abandoning everything and moving to my native Bieszczady Mountains to raise goats, I stayed focused and completed this research.

TABLE OF CONTENTS

ABBREVIATION LIST

3D	three-dimensional
AAV	adeno-associated virus
AAV5	adeno-associated virus serotype 5
AD	Alzheimer's disease
ADAM-10	disintegrin and metalloproteinase 10
ADAM-17	disintegrin and metalloproteinase 17
ADHD	attention deficit hyperactivity disorder
AED	anticonvulsant drug, antiepileptic drug
AKT	protein kinase B, serine/threonine kinase
AsKO	astrocytic knockout
ATP	adenosine triphosphate
ATUM-SEM	automated tape-collecting ultramicrotome scanning electron microscopy
Aβ	amyloid-beta
BCA	bicinchoninic acid
BSA	albumin, bovine serum
CA	cornu ammonis
CD44	Cell-surface glycoprotein-44
CD44$^{fl/fl}$	mouse line with loxP sides flanking exon 3 of *Cd44* gene
CD44-ir	CD44 immunoreactivity
CD44s	standard CD44
CD44v	CD44 variants
Cdc42	Cell Division Cycle 42
CL	contralateral
CNS	central nervous system
CreER, CreERT	Cre recombinase and an estrogen receptor fusion protein
CreERT2	enhanced Cre recombinase and an estrogen receptor fusion protein
CSC	cancer stem cell
dd	double-distilled

DG	dentate gyrus
DNA	deoxyribonucleic acid
dNTP	deoxyribonucleotide triphosphate
ECM	extracellular matrix
EEG	electroencephalographic, electroencephalography
eGFP	enhanced green fluorescent protein
EM	electron microscopy
ER-LBD	estrogen receptor ligand binding protein
ERM	ezrin, radixin, moesin
FIB-SEM	from focused ion beam scanning electron microscopy
GA	glutaraldehyde
GAPDH	glyceraldehyde-3-phosphate dehydrogenase
GC	granule cell
GCD	granule cell dispersion
GCL	granule cell layer
GFAP	glial fibrillary acidic protein
GFAP-Cre^{ERT2}	mouse line with CreERT2 fusion protein
GFAP-ir	GFAP immunoreactivity
GFP	green fluorescent protein
GLT-1	glutamate transporter-1
HA	hyaluronan
HIER	heat-induced epitope retrieval
HRP	horseradish peroxidase
HS	hippocampal sclerosis
HSP90	heat shock protein 90
i.p.	intraperitoneally
IgG	immunoglobulin G
IL	ipsilateral
ILAE	International League Against Epilepsy
IQR	interquartile range
ITR	inverted terminal repeat
KA	kainic acid, kainate

LEC	lateral entorhinal cortex
LGI-1	leucine-rich glioma inactivated protein 1
LTD	long-term depression
LTP	long-term potentiation
MEC	entorhinal cortex
MERLIN	moesin- ezrin-radixin-like protein
MF	mossy fibers
MFS	mossy fiber sprouting
MgCl2	magnesium chloride
ML	molecular layer
MMP-9	matrix metalloproteinase 9
MRI	magnetic resonance imaging
MS	multiple sclerosis
MT1-MMP	membrane type 1-matrix metalloproteinase
MTLE	mesial temporal lobe epilepsy
mTOR	mechanistic target of rapamycin
mTORC1	mechanistic target of rapamycin complex 1
NDS	normal donkey serum
NDST	normal donkey serum in phosphate-buffered saline with Triton X-100
NFDM	non-fat dry milk
NFT	neurofibrillary tangle
OCD	obsessive-compulsive disorder
PAP	peripheral astrocyte process
PaS	parasubiculum
PB	phosphate buffer
PBS	phosphate-buffered saline
PBST	phosphate-buffered saline with Triton X-100
PCR	polymerase chain reaction
PD-L1	programmed death-ligand 1
PDS	postsnaptic density
PFA	paraformaldehyde
PI3K	phosphoinositide 3-kinase

PP	perforant pathway
PrS	presubiculum
PSD	post-synaptic density
PVDF	polyvinylidene difluoride
Rac1	Rac Family Small GTPase 1
RhoA	Ras Homolog Family Member A
ROI	region of interest
rOTO	reduced osmium – thiocarbohydrazide – osmium
S.E.M.	standard error of the mean
s100β	s100 calcium-binding protein β
SBEM	serial block-face electron microscopy
SDS-PAGE	sodium dodecyl sulfate-polyacrylamide gel electrophoresis
SE	*status epilepticus*
SEM	scanning electron microscopy
SFK	Src family kinase
SPO	synaptoporin
SRGN	serglycin
SUDEP	sudden unexpected death in epilepsy
TAE	Tris-Acetate-EDTA buffer
TAM	tamoxifen
TBS	Tris-buffered saline
TBST	Tris-buffered saline with Tween 20
TEMED	tetramethylethylenediamine
TL	temporal lobe
TLE	temporal lobe epilepsy
T-SSR	tyrosine-type site-specific recombinases
vEEG	simultaneous EEG and video recording
WHO	World Health Organization
WT	wild type
ZnT3	zinc transporter 3

ABSTRACT

Epilepsy is a widespread neurological disorder affecting millions worldwide, with temporal lobe epilepsy (TLE) being its most common drug-resistant form. Current treatments primarily target neuronal excitability, neglecting the significant contributions of glial cells, particularly astrocytes, in epilepsy progression. CD44, a cell-surface glycoprotein involved in cell adhesion, neuroinflammation, and synaptic plasticity, is highly upregulated in epilepsy models. This thesis investigates the role of astrocytic CD44 in epileptogenesis, aiming to elucidate its involvement in seizure development, hippocampal structural remodeling, and synaptic alterations. The central research question addresses whether astrocytic CD44 contributes to TLE's pathophysiological changes and whether its modulation could influence disease progression.

To explore this question, an astrocyte-specific CD44 knockout mouse model was generated using the Cre-loxP system. The kainate (KA) model of temporal lobe epilepsy was employed to induce *status epilepticus*, replicating TLE-like pathologies. Advanced methodologies were applied, including immunohistochemistry for assessing reactive astrogliosis, mossy fiber sprouting and granule cell dispersion, Western blot analysis for protein expression, and serial block-face electron microscopy (SBEM) for high-resolution examination of synaptic ultrastructure. Electroencephalographic (EEG) recordings further characterized seizure patterns and severity in CD44-depleted mice compared to controls. This comprehensive approach enabled the assessment of astrocytic CD44's role across molecular, cellular, and systemic levels in epileptogenesis.

The thesis findings demonstrate that astrocytic CD44 deletion influences both seizure patterns and hippocampal remodeling in a KA-induced model of TLE. Specifically, CD44-deficient mice showed a reduction in the frequency of behavioral seizures but an increase in electrographic non-convulsive episodes detectable only via EEG. While CD44 deletion did not significantly affect the latency to the first spontaneous seizure or the severity of convulsive seizures, it reduced hallmark structural changes of epileptogenesis, including reactive astrogliosis, mossy fiber sprouting, and granule cell dispersion. SBEM analyses showed increased dendritic spine number, reduced

postsynaptic density size, and decreased astrocytic ensheathment in the CD44-depleted epileptic brain compared to controls. These findings underscore the essential role of astrocytic CD44 in preserving synaptic integrity and stability during epileptic insults.

These results suggest that astrocytic CD44 plays a pivotal role in hippocampal remodeling and seizure propagation. By attenuating pathological astrocyte responses, CD44 deletion may mitigate some of the structural changes associated with TLE, positioning CD44 as a potential therapeutic target. This work underscores the importance of astrocyte-driven mechanisms in epilepsy and advocates for a broader perspective in designing future treatments, integrating neuronal and glial contributions to disease progression.

STRESZCZENIE

Epilepsja to powszechne zaburzenie neurologiczne dotykające miliony ludzi na całym świecie, z czego jej najczęstszą, lekooporną postacią jest padaczka skroniowa (TLE). Obecne metody leczenia koncentrują się głównie na regulacji pobudliwości neuronalnej, pomijając istotny wkład komórek glejowych, szczególnie astrocytów, w progresję epilepsji. CD44, glikoproteina powierzchniowa biorąca udział w adhezji komórek, procesach neurozapalnych i plastyczności synaptycznej, wykazuje znacznie zwiększony poziom regulacji pozytywnej w modelach padaczki. Niniejsza rozprawa doktorska bada rolę astrocytarnego CD44 w epileptogenezie, mając na celu wyjaśnienie jego udziału w rozwoju napadów padaczkowych, przebudowie hipokampa oraz zmianach w ultrastrukturze synaptycznej. Kluczowym jest pytanie czy astrocytarne CD44 przyczynia się do zmian patologicznych obserwowanych w TLE oraz czy jego modulacja może wpływać na przebieg choroby.

Aby zbadać to zagadnienie opracowano model myszy z delecją CD44 w astrocytach przy użyciu systemu Cre-loxP. Do indukcji stanu padaczkowego wykorzystano model padaczki skroniowej wywołanej iniekcją kwasu kainowego odtwarzając patologie charakterystyczne dla TLE. W badaniach zastosowano zaawansowane metody, takie jak immunohistochemię do oceny reaktywnej astroglejozy, bocznicowania włókien kiciastych i rozproszenia komórek ziarnistych, analizę Western blot do badania poziomu ekspresji białek oraz mikroskopię elektronową metodą seryjnych skrawków (SBEM) do obrazowania ultrastruktury synaptycznej w wysokiej rozdzielczości. Dodatkowo, rejestracje elektroencefalograficzne (EEG) pozwoliły na charakterystykę wzorców i nasilenia napadów u myszy pozbawionych CD44 w astrocytach. To kompleksowe podejście umożliwiło ocenę roli astrocytarnego CD44 na poziomie molekularnym, komórkowym i systemowym w epileptogenezie.

Wyniki pracy wykazały, że delecja CD44 w astrocytach wpływa na wzorce napadów oraz przebudowę hipokampa w modelu padaczki skroniowej wywołanej iniekcją kwasu kainowego. Myszy pozbawione CD44 wykazywały zmniejszoną częstotliwość napadów behawioralnych, ale zwiększoną liczbę napadów elektrograficznych, niekonwulsyjnych wykrywalnych tylko za pomocą EEG. Chociaż

delecja CD44 nie miała znaczącego wpływu na czas do pierwszego spontanicznego napadu ani na nasilenie dotkliwości napadów konwulsyjnych, to zmniejszyła charakterystyczne zmiany strukturalne związane z epileptogenezą – reaktywną astroglejozę, bocznicowanie włókien kiciastych oraz rozproszenie komórek ziarnistych. Analizy SBEM ujawniły zwiększoną liczbę kolców dendrytycznych, zmniejszony obszar zajmowany przez białka gęstości postsynaptycznej oraz obniżenie stopnia okalania synaps przez astrocyty w mózgu myszy z deficytem CD44 w porównaniu do grupy kontrolnej. Wyniki te podkreślają kluczową rolę astrocytarnego CD44 w zachowaniu integralności i stabilności synaptycznej podczas napadów epileptycznych.

Przedstawione wyniki dowodzą, że astrocytarny CD44 odgrywa kluczową rolę w procesach przebudowy hipokampa oraz reaktywnej astroglejozy podczas epileptogenezy. Sugerują one, że delecja CD44 może łagodzić niektóre zmiany strukturalne związane z TLE, czyniąc CD44 potencjalnym celem terapeutycznym. Badania te podkreślają znaczenie mechanizmów regulowanych przez astrocyty w kontekście epilepsji i wskazują na konieczność szerszego podejścia do projektowania przyszłych terapii, uwzględniających zarówno neuronowe, jak i glejowe aspekty progresji choroby.

1. INTRODUCTION

1.1. EPILEPSY OVERVIEW

1.1.1. Epidemiology and etiology

Epilepsy is one of the most common chronic neurological diseases affecting around 50 million people worldwide. It is characterized by recurrent seizures which are a result of excessive neuronal firing either in a part of the brain or throughout its entirety [1]. In 2014, the International League Against Epilepsy (ILAE) proposed to expand the already existing conceptual definition of epilepsy with its operational (practical) clinical definition presented in Figure 1.1 [2]. It describes epilepsy as a disease of the brain, rather than a disorder, and sets a group of conditions that are used by neurologists while diagnosing a patient.

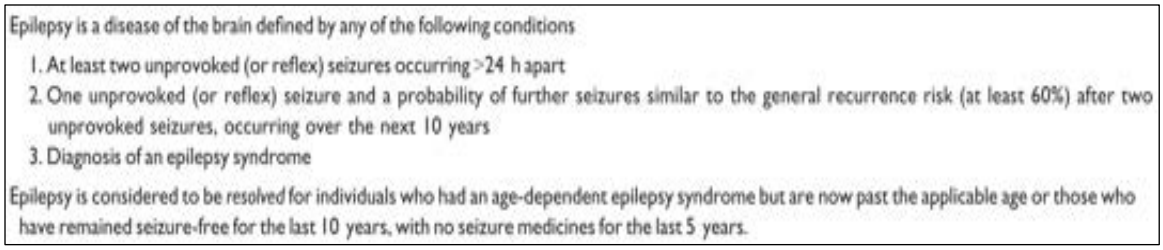

Figure 1.1. The operational clinical definition of epilepsy. Figure from Fisher et al. 2014 [2], modified.

Although one person can have more than one etiology of epilepsy, the main ones are divided into six categories: 1) structural, e.g., brain tumors/traumas, 2) metabolic, e.g., cerebral folate deficiency, 3) genetic, e.g., mutation in leucine-rich glioma inactivated protein 1, 4) infectious, e.g., cerebral toxoplasmosis or human immunodeficiency virus, 5) immune, e.g., antibody-mediated limbic encephalitis, and 6) unknown. Etiology-known epilepsy in children is usually caused by genetics and perinatal brain malformations [3]. In adults, without a genetic seizure background, most cases come from head traumas and brain tumors [4]. Still, close to 50% of cases are of an unknown origin.

It seems there is no gender predominance for epilepsy, although it does not affect all ages evenly. Most diagnosed patients form two groups: up to 9-year-old children and ~80-year-old adults [5, 6]. According to the World Health Organization (WHO), 80% of

people suffering from epilepsy come from low- and middle-income countries. To some extent, it may be a result of a higher risk of endemic infections, like malaria, and lower availability of medical care in those regions.

1.1.2. Classification

In 2017, the ILAE Classification of the Epilepsies was updated to indicate the up-to-date scientific understanding of epilepsy and help clinicians with the diagnostic process (Figure 1.2). It is now divided into three levels: I) seizure type, II) epilepsy type, and III) epilepsy syndrome [7]. Additionally, every step needs to consider epileptic etiologies.

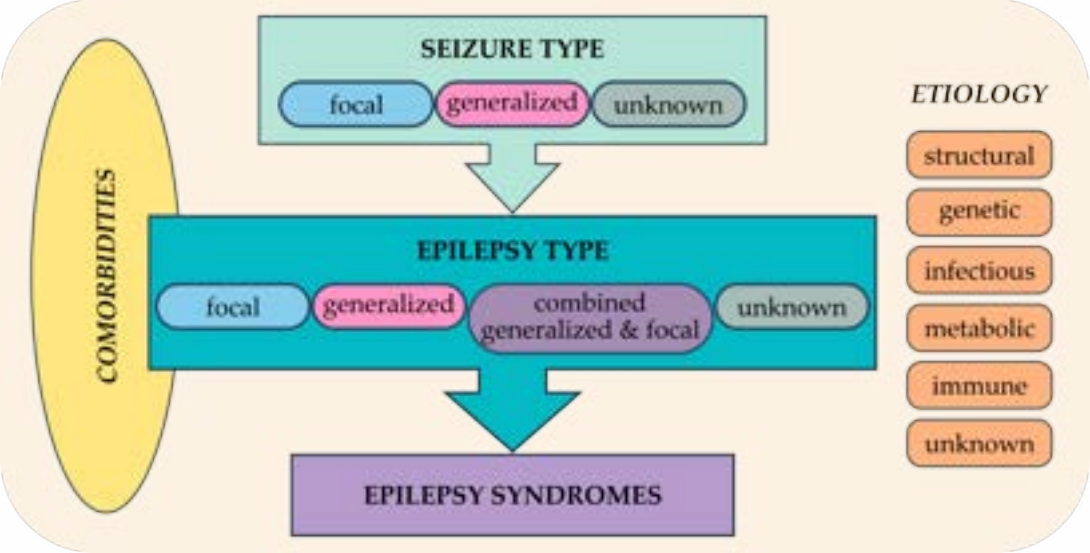

Figure 1.2. ILAE 2017 framework for the classification of epilepsies. Figure from Scheffer et al. [7], modified.

Seizure onsets are categorized into 1) focal, 2) generalized, 3) unknown, and 4) unclassified. Focal seizures, previously called "partial", are the ones starting from a specific locus. Symmetric or asymmetric activation of both hemispheres indicates a generalized seizure. Episodes that due to incomplete data cannot be classified to either of the previous groups are usually labeled with "unknown" onset.

Seizure analysis also includes a person's level of awareness and the presence of movements during an episode (motor or non-motor symptoms). Motor symptoms may involve short muscle twitching (myoclonus), jerking motions (clonic), weak or limp muscles (atonic), tense or stiff muscles (tonic), or epileptic spasms. Non-motor symptoms include "absence seizures", lack of activity (behavior arrest), or changes in cognition,

sensations, or automatic functions [8]. Epilepsy type classification shares many similarities to seizure onset examination and is subdivided into 1) focal, 2) generalized, 3) combined generalized and focal, and 4) unknown. Epilepsy syndrome is defined as a characteristic cluster of clinical and EEG features, often supported by specific etiological findings (structural, genetic, metabolic, immune, and infectious). Syndromes can have 1) generalized onset seizures, 2) focal onset seizures, 3) focal and generalized onset seizures, and 4) developmental and/or epileptic encephalopathy or progressive neurological degeneration [9]. The use of that multilevel process for epilepsy determination is crucial for patients and their clinicians. Along with an accurate diagnosis comes a better understanding of one's prognostics and treatment opportunities.

1.1.3. Management and mental health implications

Epilepsy is typically managed with daily anticonvulsant drugs (AEDs) after a second seizure occurs, though treatment may begin after a first seizure in individuals at high risk for future episodes. Encouraging self-management of the condition can be beneficial – reducing or eliminating factors that trigger seizures (blinking light avoidance, a proper amount of sleep at night, etc.). In cases where epilepsy is resistant to medication, alternative treatments may be explored, such as specialized diets (ketogenic), neurostimulator implants, or surgical intervention [10-14].

People with epilepsy often face social isolation and stigma [15]. Apart from the issues regarding for example driving permissions, educational and employment barriers, or parenthood difficulties, the mental health of people with epilepsy is usually quite impacted too. These problems may arise from coping with the condition or as side effects of medications. However, even those with well-managed epilepsy face an elevated risk. Common emotional health challenges for people with epilepsy include depression, anxiety, attention deficit hyperactivity disorder (ADHD), obsessive-compulsive disorder (OCD), and suicidal thoughts and behaviors [16-22]. Though rare, epilepsy can lead to life-threatening complications, such as:

- *Status epilepticus*: occurs when seizures last longer than five minutes or when a person has multiple seizures without fully regaining consciousness. It increases the risk of permanent brain damage and death [23].

- ❖ Sudden unexpected death in epilepsy (SUDEP): a small number of people with epilepsy are at risk for sudden death, with the exact cause unknown. Some studies suggest it may be linked to heart or respiratory issues [24, 25].

Those with frequent tonic-clonic seizures or poorly controlled episodes are at a higher risk for SUDEP. Approximately 1% of people with epilepsy die from this condition, with the highest risk found in individuals with severe, treatment-resistant epilepsy.

Considering all current therapeutic models that focus mostly on the neurons and their signaling, it is important to also look for other possible epilepsy treatment targets in the central nervous system (CNS).

1.2. HIPPOCAMPUS

1.2.1. Structure

The hippocampal formation, a critical component of the brain's limbic system, plays a pivotal role in various cognitive and neural functions and is associated with memories, emotions, and motivation. It is characterized by its unique horseshoe-shaped structure, nestled within the medial temporal lobe. It comprises several subregions – the hippocampus proper (cornu ammonis, CA; including CA1, CA2, CA3, sometimes CA4 subregions), the dentate gyrus (DG), and the parahippocampus (including presubiculum [PrS], parasubiculum [PaS], and subiculum) presented in Figure 1.3, each contributing to its complex functionality [26-28].

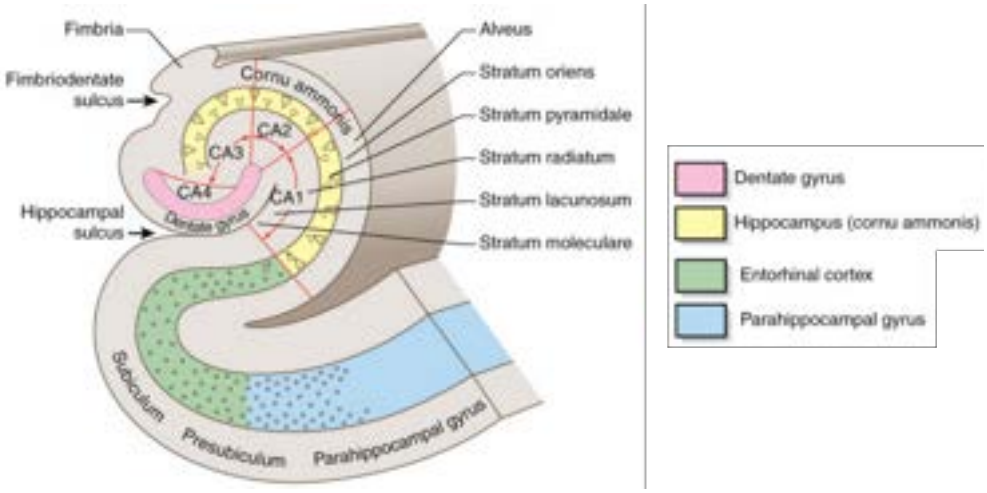

Figure 1.3. Hippocampal formation anatomy. Red arrows display the neuronal circuit between cornu ammonis subregions. Figure from Medical Dictionary: Hippocampus [27], modified.

1.2.2. Function

Essentially, hippocampal formation is responsible for memory formation, spatial navigation, and attention control (hippocampus), together with memory encoding and retrieval (parahippocampus). Each of its subregions takes upon slightly different functions that eventually create a well-organized network.

The dentate gyrus takes part in the mnemonic processing of spatial information, episodic and spatial memory forming, and instinctive exploration of new environments. The CA3 region receives input from the DG's granule cells and mossy fibers, and through the perforant pathway from the entorhinal cortex (MEC). When artificially activated, CA3 resembles the seizure-like neuronal activity [29]. It stores spatial data, including object and place memories [30]. Similarly to CA3, the CA2 region receives input from the MEC, but mostly encodes time information rather than spatial information, and contributes to the episodic autobiographical memory [31]. CA3 and CA2 send spatial and temporal data to the CA1 region, where the input is combined. That way it is possible to tell the difference between the memory of one event from another. Although both CA1 and CA3 regions are involved in context-dependent learning, only CA1 is necessary for contextual memory retrieval [32].

The subicular complex (subiculum, PrS, PaS) continually responds to an influx of information. It delivers input to the entorhinal-hippocampal spatial-memory system and is associated with memories, navigation, and the stress response [33, 34]. The MEC functions as an information-routing hub between the neocortex and the hippocampus and collaborates with the latter on memory formation, consolidation, and optimization in sleep [35]. The more detailed information flow across the hippocampal formation is described in Figure 1.4.

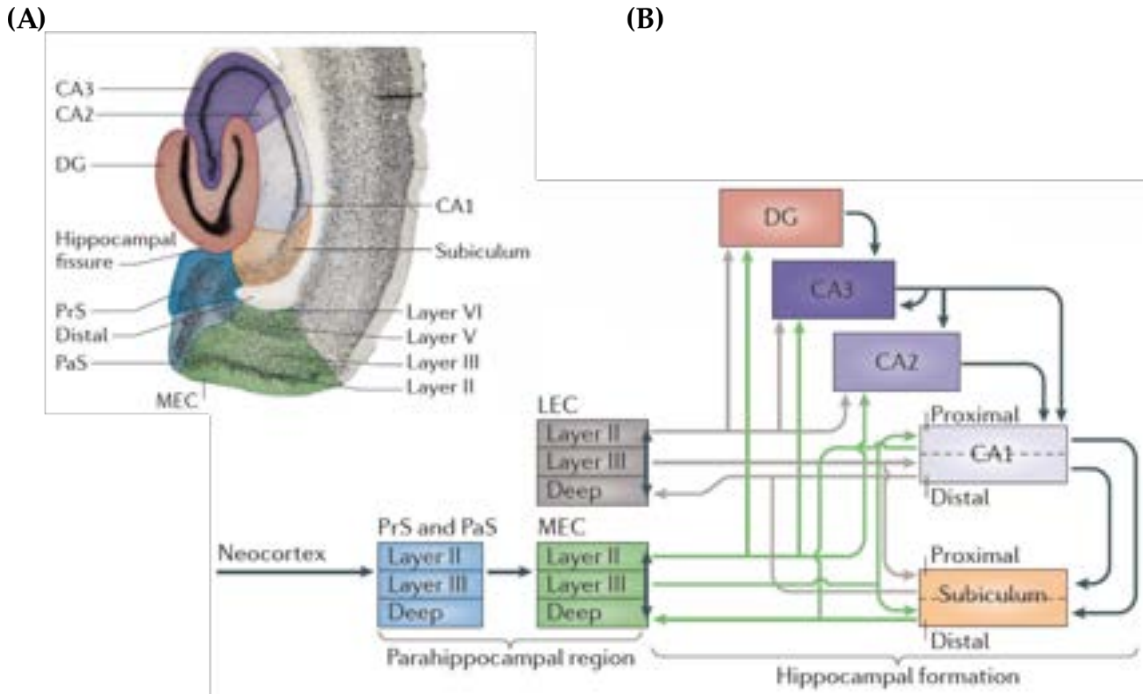

Figure 1.4. Anatomy of rodent hippocampal formation and information flow. (**A**) The right hemisphere of a rat brain. Horizontal section through the hemisphere. (**B**) The standard connectivity model. The MEC sends information to the hippocampal formation, with layer II targeting the DG, CA3, and CA2, while layer III projects to CA1 and the subiculum. Outputs from CA1 and the subiculum go to layer V of the entorhinal cortex. All layers of the entorhinal cortex appear to have reciprocal connections, as indicated by double-headed arrows. This connection pathway (green arrows) is mirrored by a similarly structured route originating from and terminating in the lateral entorhinal cortex (LEC; grey arrows). Both pathways converge on individual neurons within the DG, CA3, and CA2 but affect different neurons in CA1 and the subiculum. Projections to and from the MEC connect with neurons in CA1 near CA2 (proximal) and with those in the subiculum close to the PrS (distal), while the reverse is true for the LEC projections. Inputs that are specific to the MEC are derived from the PrS and the PaS. Figure from Moser et al. [28], modified.

1.2.3. Clinical significance

The hippocampus is believed to play a crucial role in many psychiatric and neurological diseases. As several examples of synaptic plasticity, like long-term potentiation (LTP) and long-term depression (LTD), have been described in its circuits, the hippocampus became a classic model for the study of neuroplasticity. Simultaneously, the high hippocampal neuroplasticity degree makes this structure vulnerable to conditions leading to cognitive deficits – chronic stress, aging, neurodegeneration, neuroinflammation, ischemia, or epilepsy [36].

For chronic diseases (like chronic epilepsy, neuropsychiatric or neurodegenerative disorders) the development time of pathological changes is longer and the alterations are more complex. Hippocampal neurodegeneration in Alzheimer's

disease (AD) starts early in AD development and displays both synaptic and intraneuronal molecular remodeling through intracellular neurofibrillary tangle (NFT) formation and extracellular amyloid-beta (Aβ) deposition [37]. The hippocampus is capable of generating epileptic seizures leading to temporal lobe epilepsy (TLE) associated with reactive astrogliosis and segmental neuronal cell loss in the pyramidal cells of CA1 and CA4 regions [38-40]. In multiple sclerosis (MS), a condition associated with both AD and epilepsy, the neuroinflammatory cascade leads to atrophy, demyelination, and degeneration of the white matter. MS patients exhibit cognitive dysfunction and memory/learning troubles indicating hippocampal memory system involvement [41-43].

1.3. TEMPORAL LOBE EPILEPSY

Presently available antiepileptic drugs work mainly by suppressing neuronal hyperexcitability but also cause numerous side effects that impair people's quality of life [44]. Additionally, almost a third of patients suffer from drug-resistant types of epilepsy [45], of which TLE is the most prevalent one. One of four main brain lobes, the temporal lobe (TL), is responsible for semantic knowledge, as well as auditory and visual functions [46]. Its damage often causes not only semantic and episodic memory deficiencies but also sensory hallucinations [47]. Some of the most important TL structures comprise the limbic node (incl. the hippocampus and amygdala) responsible for emotional reactions, unconscious body functions, learning and memory, and speech-associated Wernicke's and Broca's areas. Seizure onset in TLE can be initiated in the interconnected structures within the temporal lobe and adjoining regions, e.g., the hippocampus [48]. Based on the structural correlations, two types of TLE can be described [49]:

- mesial temporal lobe epilepsy (MTLE) – affects medial or internal parts of the TL and seizures usually start in the hippocampus or its surrounding area,
- neocortical/lateral temporal lobe epilepsy – affects the external part of the temporal lobe.

1.3.1. Mesial temporal lobe epilepsy and hippocampal sclerosis

MTLE accounts for approximately 80% of all temporal lobe seizures [50]. It is frequently discussed as an individual disorder due to some differences from the lateral

type of TLE that are seen in its etiology, imaging, and electrophysiology. Damages to mesial temporal lobes can lead to amnesia and failure to create or preserve new memories [51]. One of the most distinctive structural features of MTLE is hippocampal sclerosis (HS). It can be observed using brain magnetic resonance imaging (MRI) as scarring to the TL, sometimes seen as a shrinkage of the hippocampus.

1.3.2. Structural changes in mesial temporal lobe epilepsy

Epileptic seizures lead to morphological rearrangements of neuronal circuits that are accompanied by remodeling, pruning, and *de novo* formation of synapses in the hippocampus [52, 53]. Experimental animal models studying *status epilepticus* (SE) reveal that hippocampal dendritic spines are dynamically altered during the establishment and maintenance of spontaneous seizures. In addition to the widespread loss of spines, the remaining ones are increased size-wise and often form multisynaptic "giant" spines, with abundant postsynaptic densities (PSDs), creating connections with different presynaptic boutons [53-56]. The loss of neurons in the hippocampal area was described in both human specimens [57] and animal models [58-61] of temporal lobe epilepsy. In HS, pyramidal cells in the CA1, CA3, and CA4 areas are the most affected, while neurons in the CA2 region and DG granule cells are more insusceptible to seizure damage [62]. Those changes are also associated with reactive astrogliosis, a response of astrocytes to some CNS pathologies. During the activation, astrocytic cells increase size-wise, and strong upregulation of glial fibrillary acidic protein (GFAP) can be observed. This reaction aids in acute stress management, tissue damage prohibition, and homeostasis reinstatement [63]. Additionally, except for neuronal loss and astrogliosis, in MTLE-related HS visible changes can be noticed in the granule cell organization (granule cell dispersion, GCD), neuropeptide fiber networks, and mossy fiber sprouting (MFS) [64]. Although GCD does not have any agreed definition, it is recognized by a distinctive increase in the width of the granule cell layer (GCL), some granule cell (GC) loss, and patterns of GCs in the molecular layer. All that can be seen in almost half of MTLE/HS cases [65, 66]. Neuronal and astrocytic pathological changes alter the circuitry of the hippocampal formation, followed by MFS and molecular modifications in the expression of neurotransmitter receptors. In normal conditions, mossy fibers (MF; granule cell axons) extend with projections to mossy cells in the hilus and CA3 pyramidal

neurons (Figure 1.5-A). In the epileptic hippocampus, along with the loss of mossy cells and CA3 pyramidal cells, granule cell axons sprout through the GCL to the inner molecular layer (ML) of the DG creating aberrant synaptic connections (Figure 1.5-B) [67].

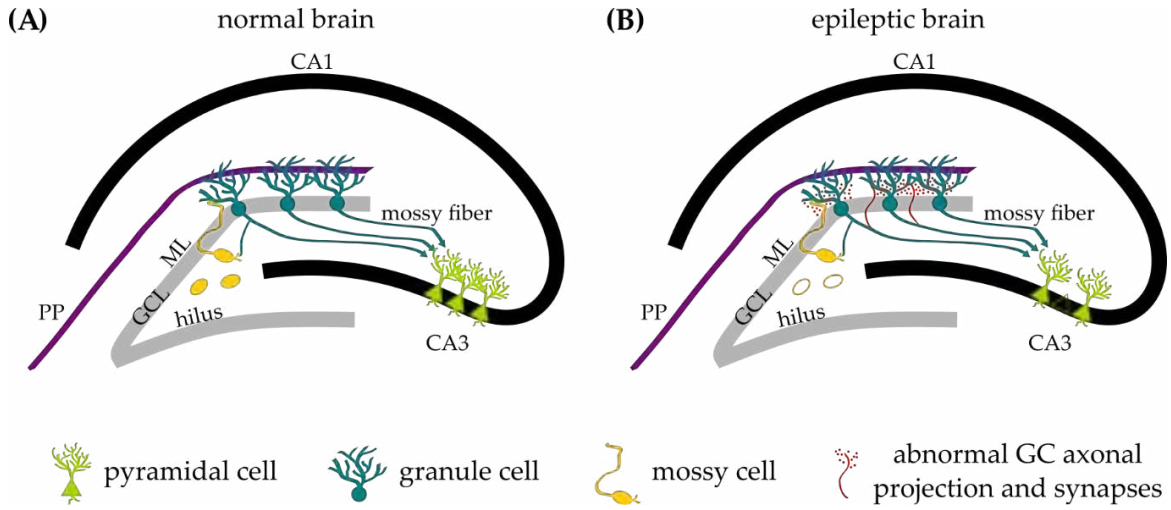

Figure 1.5. Hippocampal formation in the normal and epileptic brain. (**A**) In a healthy brain, the GCL of the DG is densely populated with small GCs. Above this layer lies the ML, which is largely devoid of cells and primarily contains the apical dendrites of GCs. This outer ML receives inputs from the entorhinal cortex via the perforant pathway (PP). GCs send out axons known as mossy fibers that project to the hilus, where they connect with mossy cells and CA3 pyramidal neurons. The axons of the mossy cells project to the dendrites of contralateral GCs in the inner ML. (**B**) In the epileptic hippocampus, the loss of mossy fiber targets in the hilus leads to MFS, where the abnormal axonal projections of GCs begin to extend and extensively innervate the inner ML of the DG. This abnormal growth is highlighted in red. Figure from Cavarsan et al. 2018 [67], modified.

1.4. ASTROCYTES

Astrocytes (syn. astroglia), a subtype of glial cells, are the most abundant cells in the central nervous system. They do not conduct electrical signals similar to those of neurons but can communicate with their environment and support the functioning of other cells around them. Astroglia takes part in promoting synapse formation and adult neurogenesis, blood flow regulation in the blood-brain barrier, neurotransmitter excess clearance, immune defense, and energy metabolism [68-71].

1.4.1. Structure

Astrocytes' name derives from a specific starlike appearance, although their shape and function can differ depending on the subtype, location, and stage of development. Historically, astrocytes have been divided into protoplasmic ones – found in the gray

matter of the hippocampus and cortex with numerous branches and short processes; and white matter's fibrous astrocytes – more elongated smooth cells with fewer processes that are long and unbranched [72]. Recent advancements in electrophysiology and imaging techniques allowed for a closer examination of the astrocytic cell structure. The astroglial complex branching system (Figure 1.6) is organized into sub-compartments:

i. primary branches radiating from the soma (1st order branches) and branchlets (2nd and 3rd order branches) which can be seen using optical microscopy,
ii. perisynaptic astrocytic processes (PAPs; syn. peripheral astrocyte processes, leaflets) that due to their size cannot be visualized with optical microscopy,
iii. endfeet specialized in enwrapping blood vessels [73].

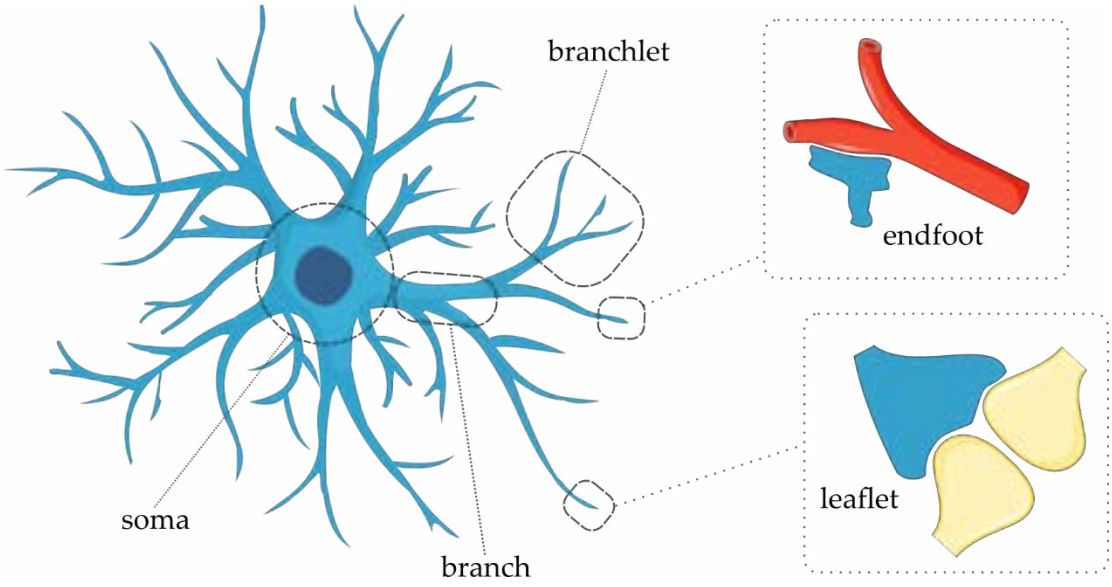

Figure 1.6. Astrocyte morphology and branching system. The schematic illustration of a protoplasmic astrocyte shows its cell body (soma) expanding into branches, branchlets, leaflets in close contact with synapses, and endfeet enwrapping brain vessels. Figure from Cabral-Costa & Kowaltowski [74], modified.

1.4.2. Function

Astroglia's main function is to maintain homeostasis in the CNS. In the hippocampus, one astrocyte can contact several neurons enwrapping ~100.000 individual synapses [75, 76]. Although they are mainly known for the control of the blood-brain barrier, nutrition transport, and synaptic plasticity, their capacity is much larger. They regulate CNS homeostasis at every stage of organization, from the molecular to systemic and organ (see graphical review in Figure 1.7) [72]. Astrocytes control synaptic transmission between presynaptic and postsynaptic neurons, acting as the third

component of the tripartite synapse [77, 78]. They communicate through gap junctions, allowing the direct transfer of ions and small molecules (such as catabolites, metabolites, and second messengers) between cells. This facilitates the propagation of calcium waves from one astrocyte to another. Astrocyte membranes also contain transport proteins responsible for neurotransmitter reuptake from synaptic clefts, including glutamate, GABA, and glycine. Beyond regulating the ionic environment and neurotransmitter supply, they can directly activate neuronal receptors by releasing gliotransmitters, such as chemokines, cytokines, and peptides [79-84]. Astroglia modulates synaptic transmission by releasing gliotransmitters – glutamate, d-serine, and adenosine triphosphate (ATP). Under normal conditions, they maintain a steady state within neuronal circuits. However, in response to nervous system injuries or pathological conditions, they shift to an "activated state", a process known as "reactive astrogliosis" [85].

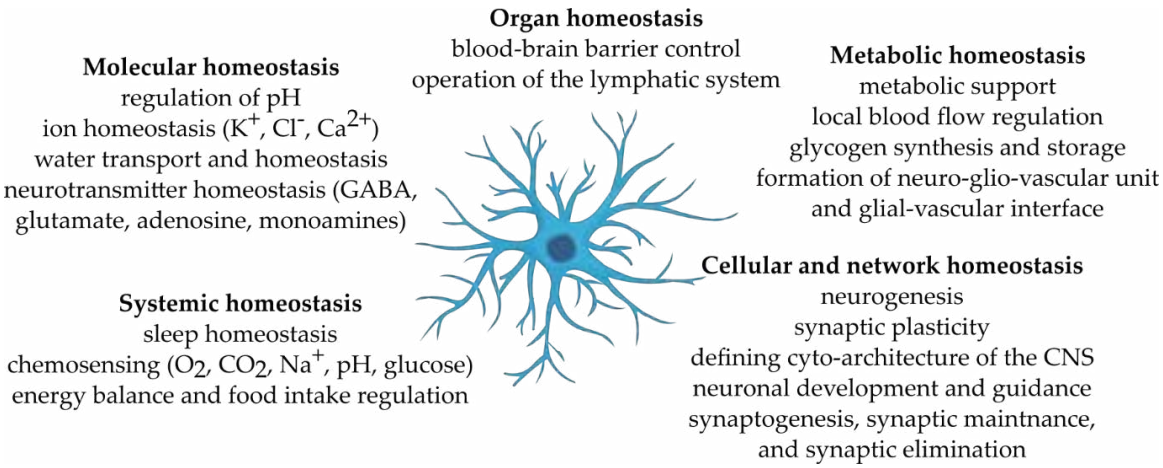

Figure 1.7. Summary of homeostatic functions of astroglia. Figure from Verkhratsky & Nedergaard [72], modified.

1.4.3. Tripartite synapse concept

Astroglial processes are closely associated with synaptic structures, and astrocytes express a whole variety of neurotransmitter receptors. This relationship gave rise to the concept of a synaptic triad, which later evolved into the tripartite synapse model (Figure 1.8) [78, 86]. The tripartite synapse emphasizes the role of glial cells, particularly astrocytes, in regulating synaptic transmission, positioning astroglial processes as essential components alongside presynaptic terminals and postsynaptic neurons. The tripartite synapse model primarily focuses on the rapid, bidirectional communication between neurons and astrocytes, where neurotransmitter-induced calcium signaling in

astrocytes leads to the release of gliotransmitters, a process known as "gliotransmission" [78, 87].

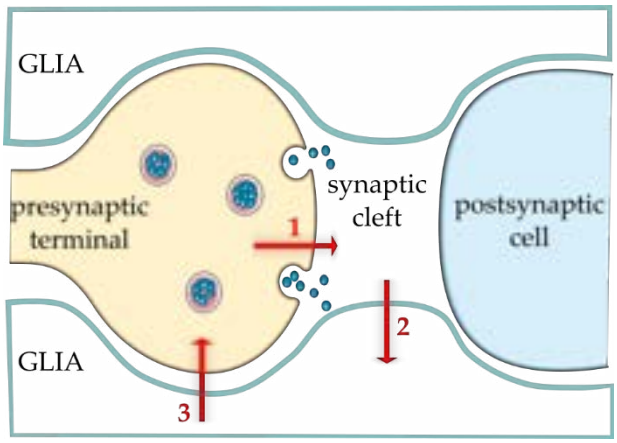

Figure 1.8. The original concept of the tripartite synapse. Throughout synaptic neurotransmission, neuronal cells release neurotransmitters from their terminals into the synaptic cleft, enabling communication with other neurons (1). In certain cases, these neurotransmitters may "spill over" into the vicinity, activating receptors on nearby astrocytes, leading to a rise in intracellular Ca^{2+} levels within the glial cells (2). This elevation in Ca^{2+} concentration triggers astrocytes to release their own neurotransmitter, typically glutamate (3). The released glutamate then influences the presynaptic nerve terminal, thereby modulating synaptic transmission. Figure from Araque et al. [78], modified.

However, the role of astrocytes extends beyond this. The previously described model further expanded into the multipartite synapse, which includes: the presynaptic terminal, the postsynaptic compartment (dendritic spine), the perisynaptic astrocytic process, microglial processes that periodically contact the synapse, and the extracellular matrix (ECM) within and beyond the synaptic cleft (Figure 1.9) [88-92]. Astrocytes are believed to shape synaptic networks, maintain ionic balance in the synaptic cleft, manage neurotransmitter activity, control spillover, and contribute to the elimination of synapses. These diverse functions are encapsulated in the concept of the "astroglial cradle," which views astrocytic coverage as crucial for supporting proper synaptic transmission [88].

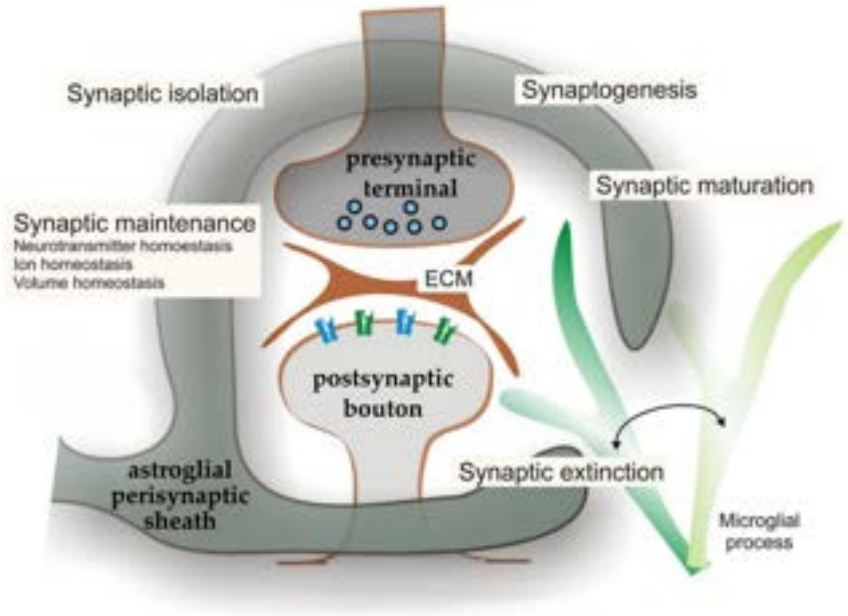

Figure 1.9. Astroglial cradle. The astroglial cradle supports and nurtures the multipartite synapse in the CNS. Most synapses in the brain and spinal cord consist of multiple components (presynaptic and postsynaptic elements, the PAP, a neighboring microglial process that intermittently contacts the synapse, and the ECM found in and around the synaptic cleft). Astrocytic perisynaptic sheaths surround these synaptic structures playing a crucial role in regulating, influencing, and assisting in synaptogenesis, along with the maturation, maintenance, and even elimination of synapses. Figure from Verkhratsky and Nedergaard [88], modified.

1.4.4. Astrocytes in epilepsy

Multiple studies show that alterations in astrocytic metabolism, channels, and transporters directly contribute to seizure susceptibility and epilepsy progression (reviewed in [85, 93]). In response to trauma, infections, neuropathologies, and neurodegenerative diseases (like epilepsy), astrocytes become reactive and undergo a process called reactive astrogliosis (syn. astrocytosis). From the structural point of view, it is a proliferation of astroglia that can be characterized by hypertrophied soma and processes (Figure 1.10). Very characteristic is also high GFAP, vimentin, and nestin expression. Depending on the severity degree, astrogliosis can be mild (slight changes in astrocytic hypertrophy and molecular profile) or severe (glial scar formation) [94]. A glial scar forms from a newly proliferated astroglia where a structure of thickly overlapping processes creates a border to inflammation and damaged tissue [95].

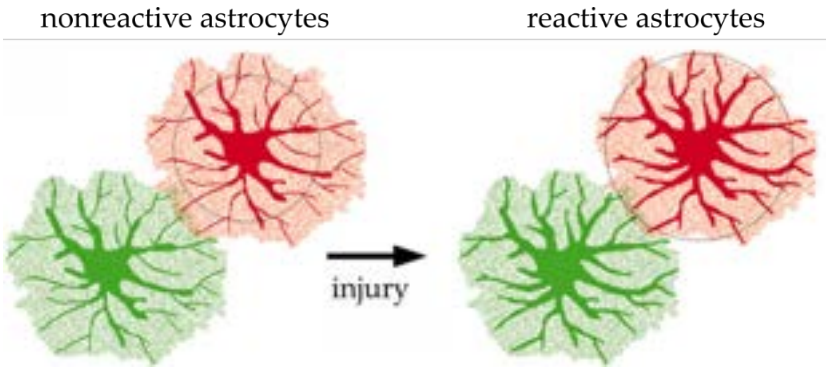

Figure 1.10. The domain of nonreactive and reactive astrocytes. A reactive astrocyte stays within its domain, but its main branches and processes become thicker. Figure from Wilhelmsson et al. [96], modified.

Reactive astrogliosis is a hallmark of epileptic foci in humans and experimental models [85]. As mentioned before, astrocytosis highly correlates with HS in TLE and can be found in most resected brain tissues from TLE patients [97]. In the epileptic brain, reactive astroglia display changed adenosine kinase and glutamine synthetase expression, and modulate Ca^{2+}-dependent gliotransmitter release (e.g., adenosine, glutamate, ATP) modifying synaptic transmission and neuronal excitability [93, 98]. Halassa et al. (2007) introduced the notion of the "astrocyte activation spectrum," proposing that enhanced gliotransmission may contribute to epilepsy, while reduced gliotransmission may be linked to schizophrenia [86]. Moreover, in temporal lobe epilepsy, several astrocytic cellular pathways have been pointed out as potential treatment targets such as the mTOR pathway, astrocytic GABA release, gap junction communication, or aquaporin 4-related potassium regulation (reviewed in [99]).

1.5. CD44

CD44 (syn. Cell-surface glycoprotein-44, MDU3, Pgp1, Inlu-related p80 glycoprotein, the hermes antigen) is a transmembrane glycoprotein, a major surface receptor for hyaluronan (HA) acting as a mediator between the cell and its extracellular microenvironment. Being the adhesion molecule expressed in different cell types, it plays an important role in many signaling pathways [100].

1.5.1. Structure and signaling

The human CD44 gene, located at the 11p13 locus, consists of 20 exons. The most common form, known as standard CD44 (CD44s), is encoded by exons 1–5 and 16–20. There are also numerous CD44 variants (CD44v), generated through extensive alternative splicing, which incorporates the "standard" exons along with various combinations of exons 6–15 [101-103]. In the CNS, the predominant isoform is expressed in the standard form [104, 105]. However, CD44 splice variants have also been identified in normal human brain tissue and in certain primary brain and peripheral nerve tumors [106-108].

The CD44 molecule consists of various functional domains. Its N-terminal extracellular domain contains motifs that serve as docking sites for different ligands, primarily HA, but also proteoglycans, cytokines, growth factors, matrix metalloproteinases, and ECM glycoproteins (Figure 1.11) [101, 109, 110]. This amino-terminal domain is connected to the plasma membrane by a short stem structure that includes proteolytic cleavage sites for metalloproteinases such as ADAM-10, ADAM-17, matrix metalloproteinase 9 (MMP-9), and membrane type 1-matrix metalloproteinase (MT1-MMP) [111, 112]. Cleavage of CD44 releases cells bound to HA, a key process in regulating cell migration. The stem region of CD44 is variable due to alternative splicing and the insertion of exons 6–15. The C-terminal cytoplasmic tail is essential for intracellular signaling. It binds to cytoskeletal components such as ankyrin and the ERM proteins — ezrin, radixin, moesin, and moesin-ezrin-radixin-like protein (MERLIN) [113]. It also interacts with signaling molecules, including Src family kinases (SFKs), small Rho GTPases, such as Ras Homolog Family Member A (RhoA), Cell Division Cycle 42 (Cdc42), and Rac Family Small GTPase 1 (Rac1) [101, 114-117]. Additionally, the CD44 cytoplasmic tail can be cleaved by γ-secretase and moved to the nucleus, where it functions as a transcriptional regulator [111].

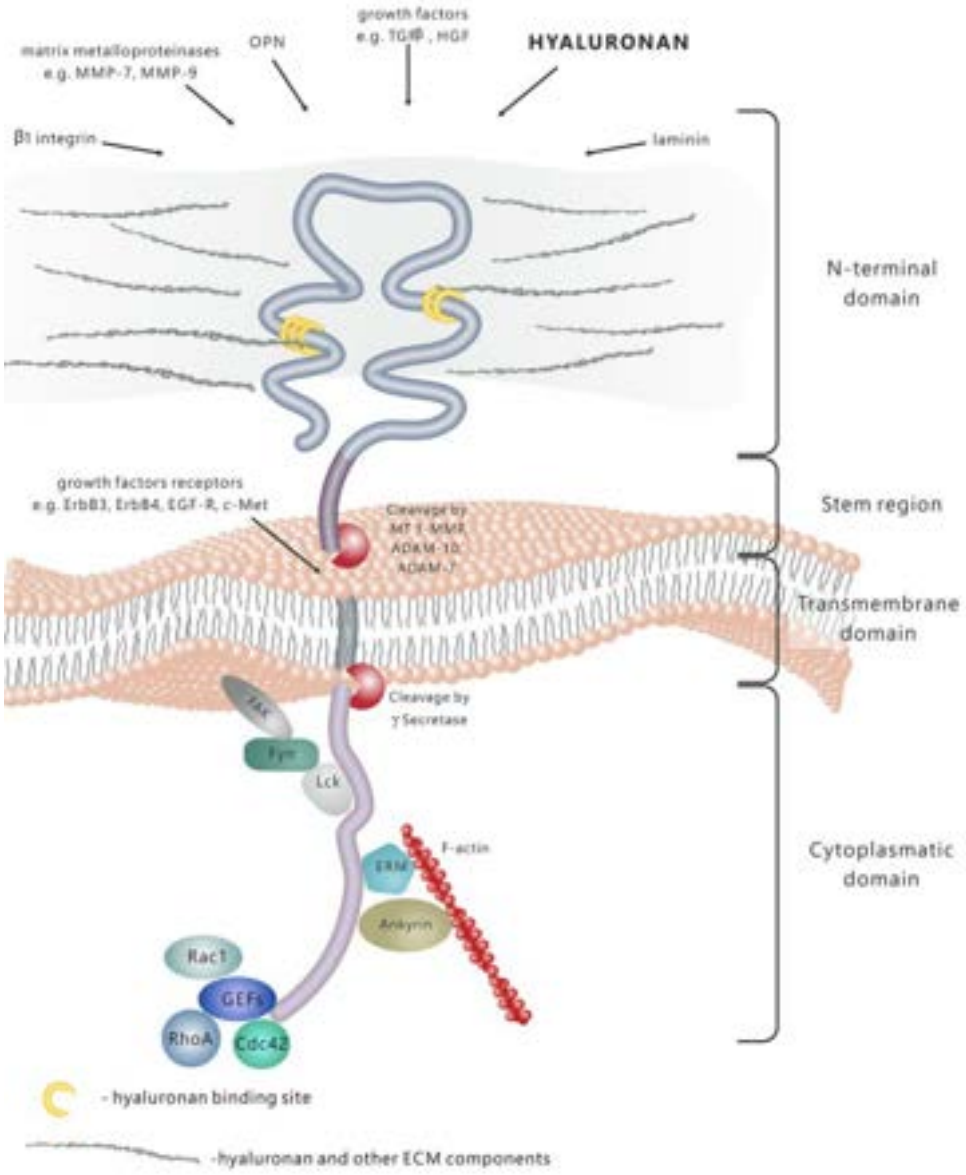

Figure 1.11. CD44 structure and signaling. CD44 is a transmembrane molecule made up of several distinct domains. Its N-terminal extracellular domain binds to different ligands, such as HA, proteoglycans, cytokines, growth factors, matrix metalloproteinases, and ECM glycoproteins,. Upon proteolytic cleavage in the stem region, the extracellular domain is released into the extracellular space. The transmembrane domain stabilizes the molecule within the plasma membrane, while the cytoplasmic domain is crucial for signal transduction. It achieves this by interacting with various molecules, including cytoskeletal components, kinases, and guanine nucleotide exchange factors (GEFs), which activate small Rho GTPases. Figure from Dzwonek & Wilczynski [100].

CD44 expression is closely associated with the morphological characteristics of astrocytes. Studies have shown that astrocytes lacking the CD44 adhesion protein exhibit a distinctive stellate-like morphology. Likewise, CD44-negative glial cells in the human brain display numerous branches and short processes (protoplasmic astrocytes). In contrast, astrocytes with high CD44 expression are more elongated, with fewer long and unbranched processes, and are typically fibrous astrocytes [115, 118].

1.5.2. Function

As CD44 protein can be found in a large number of mammalian cell types, its association with various cellular and molecular mechanisms has been intensively studied. CD44's critical role in both normal physiological processes and pathological activities (like cell proliferation, migration, adhesion, inflammation, angiogenesis, and cytoskeleton rearrangement) has led to an extensive investigation of its potential primarily in cancer, metabolism, and nervous system research [100, 102, 119].

CD44 is recognized as a cancer stem cell (CSC) marker. It regulates tumor initiation, chemoresistance, promotes programmed death-ligand 1 (PD-L1) expression eliciting immunosuppression in cancers, and suppresses tumor protein p53-induced cellular death [120, 121]. It regulates glucose metabolism in cancer cells and metabolic tissues (pancreas, liver, adipose tissue, skeletal muscles) [102]. CD44 has been observed to have an inhibitory role in adipogenesis, at least in 3T3-L1 cells. The deletion of CD44 bolsters the accumulation of lipids during adipocyte differentiation, while the re-expression of CD44 abolishes this effect, suggesting a CD44-specific effect that could have implications beyond its role in cancer [122].

As previously mentioned, CD44 is identified as a receptor for HA and other matrix molecules found in astrocytes in the human CNS. It is also present in astrocytes and cerebellar GC but not cortical neurons in the adult mouse [123]. It is widely used as an astrocyte-specific cell surface marker [124]. CD44 is also involved in signaling pathways that affect astrocyte functions. For instance, serglycin (SRGN) induces CD44-AKT (serine/threonine kinase) signaling, which triggers the proliferation of human spinal cord-derived primary astrocytes and boosts the expression of genes related to epithelial-mesenchymal transition, impeding astrocyte maturation [125]. Glycoprotein nonmetastatic melanoma protein B, expressed by astrocytes, binds directly to CD44 and acts as an important factor in attenuating astrocyte-induced neuroinflammatory responses [126]. Through osteopontin binding, CD44 is believed to be involved in astrocytic migration to degenerative motor neuron sites [127].

Those and other findings underscore the diverse roles of CD44 in astrocytes, from its involvement in the CNS and cancer to its potential impact on cellular responses to mechanical stimuli and its role in metabolic processes.

1.5.3. CD44 in epilepsy

CD44 is highly upregulated during injury and is considered one of the most crucial proteins associated with epilepsy [100, 128-130]. In humans, transcriptome analysis of epileptic patients has identified *Cd44* as one of the top five most significant Hub-Bottleneck genes linked to the pathogenesis of epilepsy [131]. Recent clinical studies show its increase in all recruited subjects with epilepsy in comparison to the control group [132]. Unlike other neurodegenerative diseases, like Alzheimer's disease that seem to be entwined with the higher risk of epilepsy, not much is known about the role of CD44 in epileptogenesis [130, 133-138].

Strong CD44 reactivity was observed in both pilocarpine- and kainate-induced SE, as well as in several epilepsy-related neurological disorders [128, 139, 140]. Significant upregulation of hippocampal CD44 expression can be seen in both rat and mouse models of epilepsy after kainate-induced SE, which suggests either a native immune reaction or an ongoing re-organization of synapses [141, 142]. Both are likely explanations. The latter has a reflection in other studies suggesting CD44's contribution to the dendritic spine functional and structural plasticity [116].

1.6. OVERVIEW OF APPLIED METHODOLOGIES

1.6.1. Transgenic animals

To study functional changes of genetic alterations *in vivo*, modern science has been providing scientists with various gene modification tools and transgenic animal models. Transgenic animals are currently the primary instrument for studying gene function in physiology, disease development and progress, and novel drug therapies or delivery targets. Alterations introduced in animals are based on either a loss/gain of function or a modification of a specific gene and consequently the protein it is coding. The house mouse (*Mus musculus*) is the most utilized organism in neurodegenerative research, mostly due to the low maintenance cost, short lifespan, usually large litter, and high phylogenetic similarities to humans [143, 144].

Changes introduced in the genome can be permanent or conditionally induced. Once activated, permanent modification cannot be reversed, e.g., gene deletion in a germline. Whereas, a conditional modification, although irreversibly introduced in the deoxyribonucleic acid (DNA), is activated only in the presence of specific recombinases. One of the commonly used techniques for conditional deletion of a certain gene sequence is the Cre-loxP system.

1.6.2. Cre-loxP system

The Cre-loxP system is a broadly used tool for gene editing that allows studying genes of interest under spatial (cell/tissue) and/or temporal (specific time) control. It is based on two main pillars: 34 bp sequence of loxP sites and Cre recombinase (cyclization recombinase). The loxP sites consist of an 8 bp core sequence surrounded by two 13 bp inverted palindromic repeats. They are recognized by Cre – a recombinase belonging to a family of tyrosine-type site-specific recombinases (T-SSRs). After a single Cre recombinase identifies two directly repeated loxP sites, it excises the sequence between them. It generates two DNA fragments – a removed circular one and an inactivated gene of interest with a remaining loxP sequence left from the recombination (Figure 1.12A). Although the Cre-loxP system is mostly used for genetic excision, it can also be applied to invert or translocate DNA, depending on the location and orientation of loxP sites [145-147].

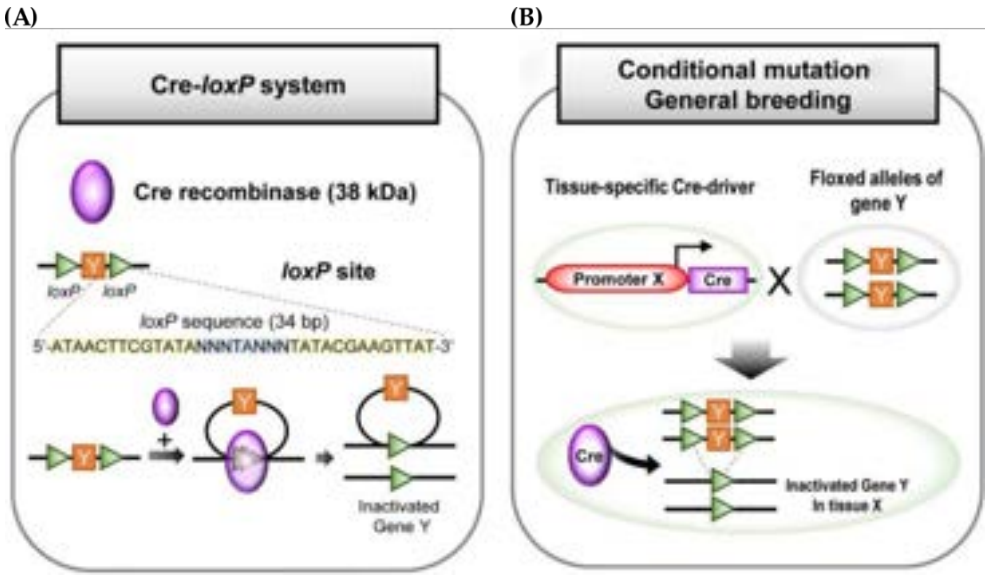

Figure 1.12. Mechanism of the Cre-loxP system. (**A**) Cre recombinase recognizes loxP sites and cuts out the sequence between them. (**B**) General breeding strategy for conditional mutation –

cross-breeding one animal having tissue-specific Cre-driver with another having loxP floxed alleles of the gene of interest. Expression of Cre recombinase in the offspring will be limited only to a specific cell type where it will excise flanked loci and inactivate the gene of interest. Figure from Kim et al. [148], modified.

To generate a conditional knockout offspring (double transgenic line) a mouse strain expressing Cre recombinase in a certain cell type (targeted with a cell-specific promoter) is cross-bred with another strain containing a gene sequence flanked (floxed) with loxP sites (Figure 1.12B). It is important to notice, that Cre recombinase in this spatially controlled gene alteration is present and active in the offspring starting from fetal life throughout every developmental stage.

A more sophisticated version of this technique allows scientists to control the activity of Cre recombinase in time. This spatiotemporal regulation is based on an inducible Cre system that requires an exogenous inducer such as tamoxifen (TAM). Tamoxifen-dependent Cre is formed by creating a fusion protein of Cre recombinase and an estrogen receptor (known as Cre^{ER} or Cre^{ERT}) containing a mutated estrogen receptor ligand binding domain (ER-LBD). This enhanced domain allows for selective binding of tamoxifen, an estrogen receptor modulator, instead of endogenous estrogen hormone. A newer variant of the TAM-inducible Cre system – Cre^{ERT2} – is an enhanced version of its predecessor shown to be around 4-fold more efficiently induced than Cre^{ERT} [149-151]. Inactive Cre^{ERT} is present in the cytoplasm as a complex formed with HSP90 (heat shock protein 90). The administration of tamoxifen disrupts the complex, binds to Cre^{ERT}, and causes its translocation to the nucleus where eventually Cre interacts with loxP sites (Figure 1.13). To achieve a sufficient level of recombination, animals have to be intraperitoneally (i.p.) injected with TAM for several consecutive days. The tamoxifen-depended Cre-loxP system can be successfully used in fully developed mice which provides an opportunity to study the consequences of gene editing in selected tissues of adult animals.

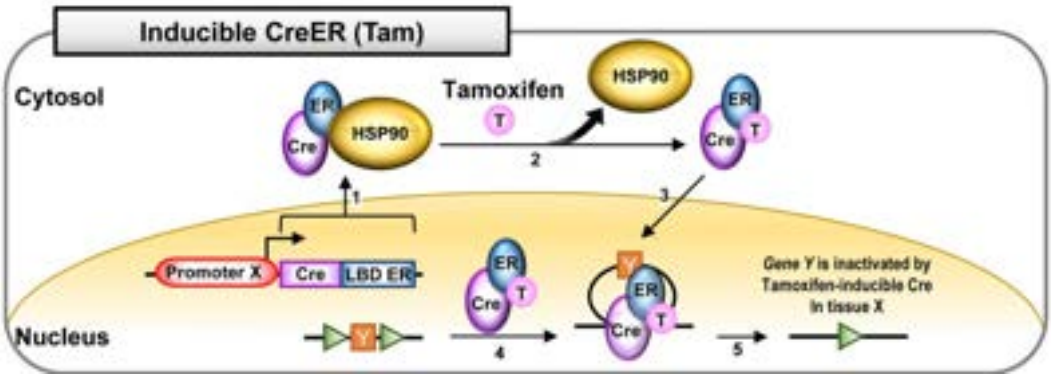

Figure 1.13. Mechanism of action of tamoxifen-inducible Cre-loxP system. Cre recombinase is transcribed as a CreER fusion protein and remains in the cytoplasm in a complex with HSP90 (1). TAM administration disturbs CreERT-HSP90 interaction (2) and, by binding to the ER domain, leads to the translocation of CreER to the nucleus (3). In the nucleus, CreER recognizes loxP sites and deactivates gene Y in tissue X. Figure from Kim et al. [148], modified.

Apart from the previously described, the Cre-loxP system can also be utilized in single transgenic animals carrying just the loxP-flanked loci. Here, Cre recombinase is introduced through a viral vector carrier directly into the investigated tissue. This method has its advantages – it is less expensive and time-consuming because there is no need to generate a double transgenic mouse line. However, one of the main disadvantages may be the fact that the recombination is limited only to targeted cells in the area where the vector was injected, e.g., in the hippocampal dentate gyrus instead of the whole brain. Among the viral vectors in genetic modification techniques, AAVs (adeno-associated viruses) are the most commonly used ones. Modified AAVs are relatively small, replication-defective, nonenveloped vectors with linear single-stranded DNA. Even though their small size holds some limitations [152], those viruses are frequently chosen due to their low immunogenicity [153]. In studies with animal models, AAVs induce a long-term (weeks to months) expression of the gene of interest, with a relatively small (0.1%) random integration in the genome [154, 155]. Neuroscientific research employs different characteristics of AAV serotypes (viral variations sharing distinctive surface structures/receptors) and their capabilities to infect a specific group of cells (tropism), as well as delivery direction (anterograde and retrograde). Nine main AAV serotypes and their properties are shown in Table 1.1. AAV tropism can be further adjusted by designing recombinant versions of multiple serotypes [156].

Table 1.1. AAV serotype family properties. The number of * presents a comparative AAV expression level: * low, ** general, *** high. The capability to transport in an indicated direction is shown as +. Table from Haggerty et al. [156], modified.

	Transport Direction		Expression by Brain Region			Cell-Type Expression		
Serotype	Anterograde	Retrograde	Striatum	Hippocampus	Cortex	Neurons	Astrocytes	Microglia
rAAV1	+	+	*	*	*	***	*	**
rAAV2	+	+	*	*	*	+		
rAAV5	+		***	***	*	**	*	
rAAV6	–	+	*	*	**	**		
rAAV7	+	+	**	**	***	**	**	**
rAAV9	+	+	**	*	***	***		

AAV vectors in combination with the Cre-loxP system and transgenic animals provide a way to effectively manipulate selected groups of cells. AAV vectors can (i) be used as carriers of loxP-floxed gene sequences into transgenic lines with Cre recombinase or (ii) insert Cre sequence into transgenic animals with loxP-flanked loci resulting in *in vivo* recombination [157-160].

1.6.3. Kainate model of mesial temporal lobe epilepsy

Mouse intrahippocampal kainic acid (KA) injection is one of the commonly used models of human MTLE that provides several key pathological and behavioral characteristics. Its histological outcomes closely resemble HS observed in human MTLE, particularly the loss of cells in the hilus and hippocampal neuronal layers, including the highly vulnerable CA1 region, astrogliosis, mossy fiber sprouting, and granule cell dispersion. This model is more often associated with nonconvulsive behavior during the acute SE but a more severe representation of Racine-type convulsive behavior has also been described [161-165]. Due to that, EEG monitoring is usually required for the full data acquisition. As EEG abnormalities change in time and severity, occurring both while awake and asleep, it is important to use 24-hour monitoring techniques (e.g., depth electrode recordings) [165, 166]. Moreover, since mice are widely used in gene expression and deletion studies, a mouse model could assist in identifying genes potentially involved in the pathophysiology of epilepsy.

1.6.4. Serial block-face electron microscopy

Electron microscopy (EM) has been used to study the ultrastructure of biological samples for many years now. Recent advancements in volume EM allow nanometer-scale

imaging of tissues and cells in three dimensions (3D) in an automated way. Automated volume imaging techniques, primarily utilizing scanning electron microscopy (SEM), enable quicker and more dependable acquisition of serial images across tissue volumes, while also offering enhanced z-resolution [167]. One of the three main volume SEM methods, aside from focused ion beam SEM (FIB-SEM) and automated tape-collecting ultramicrotome SEM (ATUM-SEM), is serial block-face EM (SBEM).

The SBEM system consists of a scanning electron microscope and a diamond-knife microtome mounted on the inner side of the microscope's vacuum chamber door along with additional hardware and software to manage the acquisition process [168]. The user places the sample into the SBEM microtome holder and performs a manual alignment to bring the sample surface to the knife's cutting edge. Afterward, the SBEM chamber is evacuated, imaging parameters are configured, and the automated acquisition process begins. After imaging the region of interest (ROI) on the sample surface, the sample is raised by the specified slice thickness (typically between 25–200 nm), and the knife cuts away the entire surface of the block face. Following each cut, the ROI is imaged on the newly exposed surface. This cut-and-image cycle operates repeatedly, allowing the acquisition of thousands of serial images with no user intervention [167, 168].

As resin-embedded, stained biological tissue has low conductivity, making it susceptible to charging effects, irregular contrast, and image distortions during SBEM imaging, it is crucial to prepare it properly beforehand. Samples take ~5 days to prepare (Figure 1.14, left panel). A fixated tissue sample is stained with heavy metals such as osmium, lead, and uranium, enhancing image contrast for SBEM and increasing the sample's conductivity to minimize charging. SBEM samples require *en bloc* staining, e.g., the rOTO protocol (reduced osmium – thiocarbohydrazide – osmium) [169-172]. Osmium staining can be supplemented with uranyl acetate and lead aspartate to further increase heavy metal content, improving image contrast. Following staining, a graded series of ethanol is used to remove the remaining water from the sample, which is then embedded in epoxy resin, replacing the ethanol. One of the commonly used resins, Durcupan [173], provides sufficient penetration and stability during electron beam exposure and sectioning with a diamond knife. The last steps of sample preparation require proper trimming (usually to a truncated pyramidal shape centered on the region of interest) and coating with a metallic layer to prevent charging. A proper preparation

process is essential for the sample to endure vacuum, high energy, and electron beam current endurance, provide adequate image contrast, and maintain sufficient hardness for slicing. The ultrastructure of analyzed tissue should also be preserved as closely to the *in vivo* state as possible [167, 174]. The next step is the SBEM acquisition (Figure 1.14, middle panel) generating a series of consecutive digital images that need to be precisely aligned and positioned within a virtual volume allowing for the 3D image analysis (Figure 1.14, right panel).

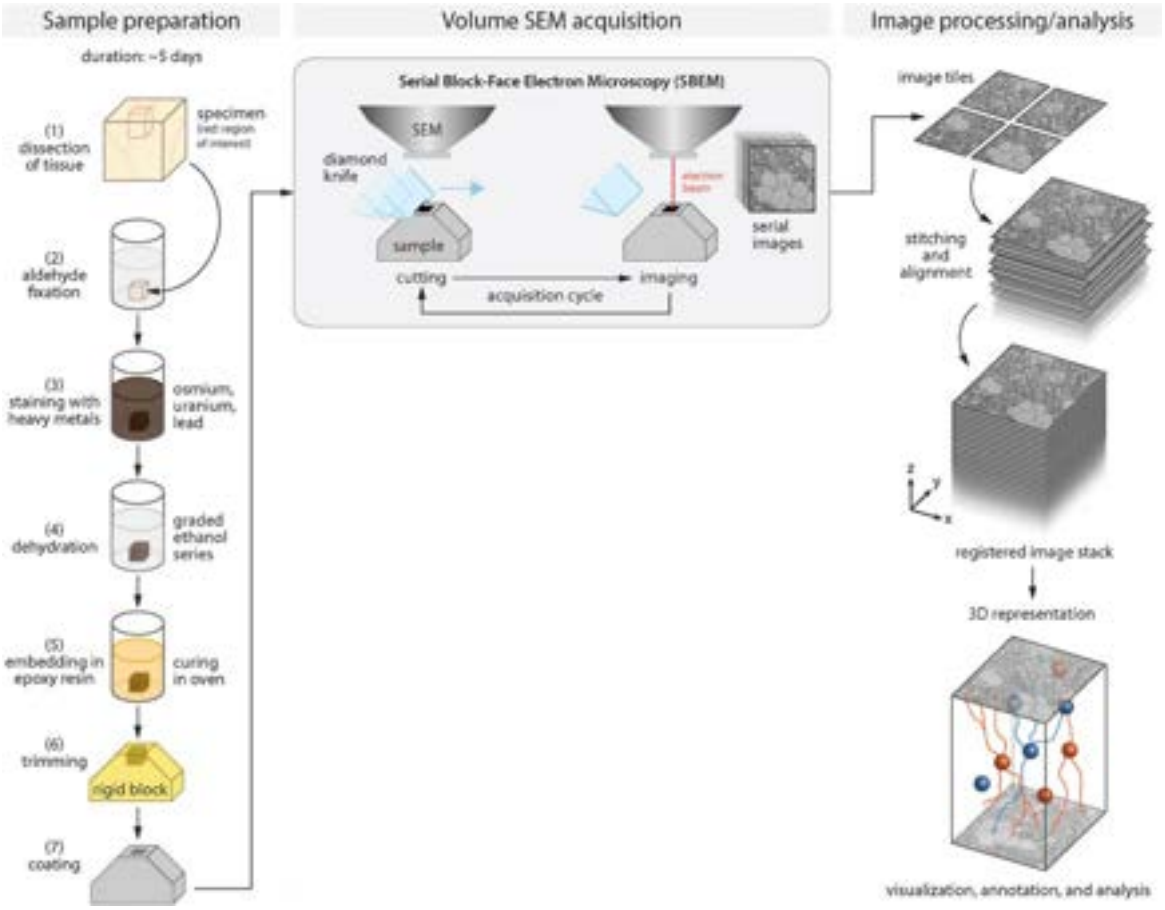

Figure 1.14. Schematic illustration of SBEM workflow from tissue to dataset. Samples go through a series of tissue preparation steps (left panel) and then undergo the image acquisition process using SBEM (middle panel). The collected images are transformed into a 3D representation of the sample volume ready for analysis (right panel). Figure from Titze & Genoud [167], modified.

2. AIMS OF THE STUDY

Not much is known about the function of CD44 transmembrane glycoprotein in the development of epilepsy. This study aimed to **determine the role of astrocytic CD44 in kainate-induced *status epilepticus*, its influence on seizure development, and structural and ultrastructural hippocampal changes accompanying epileptogenesis**.

To address the question of CD44's role in epileptogenesis, the study employed transgenic mouse lines providing the experimental CD44 knockout model for *in vivo* studies, the kainate model of mesial temporal lobe epilepsy for *status epilepticus* induction, serial-block face scanning allowing for three-dimensional reconstruction of synaptic connections, and other analytical techniques.

The specific study aims were as follows:

1) Generate a transgenic mouse line with astrocyte-specific conditional CD44 knockout that allows for temporal control of gene deletion.
2) Identify the role of astrocytic CD44 on seizure development and pattern during epileptogenesis.
3) Analyze the possible changes in temporal lobe epilepsy hallmarks – reactive astrogliosis, granule cell dispersion, and mossy fiber sprouting – in the epileptic hippocampus of CD44-depleted mice.
4) Determine the influence of astrocytic CD44 depletion on synaptic ultrastructure during epileptogenesis.

3. MATERIALS AND METHODS

All procedures throughout the study without clearly specified working temperatures were performed at room temperature (20-24°C).

3.1. Animals

3.1.1. Transgenic lines

In this study, all transgenic mouse lines had a C57BL/6 genetic background. Animals were kept and bred at the Animal House of the Nencki Institute of Experimental Biology throughout the experimental period. Mice were treated according to the ethical standards of European and Polish regulations, had free access to food and water, and were kept in individually ventilated cages (temperature: 21-23°C, humidity: 50-60%) under a 12-hour light/12-hour dark cycle. All experimental procedures were performed following the European Communities Council Directive of November 24, 1986 (86/609/EEC), Animal Protection Act of Poland, and approved by the 1st Local Ethics Committee in Warsaw (permission no. 860/2019 and 273/2017).

CD44$^{fl/fl}$

A homozygous line with loxP sites flanking (fl/fl) exon 3 of the *Cd44* gene. The line was developed and kindly provided by V. Orian-Rousseau [175] from the Karlsruhe Institute of Technology, Germany. CD44$^{fl/fl}$ line was used for cross-breeding with the GFAP-Cre^{ERT2} line to obtain a double transgenic line with a global CD44 knockout in astrocytes and for AAV-mediated *Cd44* gene deletion.

GFAP-Cre^{ERT2} (B6.Cg-Tg(GFAP-cre/ERT2)505Fmv/J, The Jackson Laboratory, #012849)

A heterozygous line with the Cre-ER^{T2} fusion protein (Cre-ERT2; Cre recombinase fused to a G400V/M543A/L544A triple mutation of the human estrogen receptor ligand binding domain) driven by the human GFAP promoter [176, 177]. Developed by F. M. Vaccarino [178] from Yale University, USA. GFAP-Cre^{ERT2} was used as an initial line for cross-breeding with the CD44$^{fl/fl}$ line to obtain double transgenic animals with a total CD44 knockout in astrocytes.

GFAP-Cre^{ERT2}xCD44$^{fl/fl}$

A double transgenic line was generated by crossing homozygous CD44$^{fl/fl}$ and heterozygous GFAP-Cre^{ERT2} mice (see 4.1.1 for more details on the breeding strategy). Animals born in the F_1 generation were heterozygous for both gene alterations and were subsequently bred again with homozygous CD44$^{fl/fl}$ mice. Generated offspring had a homozygous mutation in the *Cd44* gene and heterozygous insertion of Cre recombinase under the GFAP promoter. GFAP-Cre^{ERT2}xCD44$^{fl/fl}$ line was used in experiments that required a conditional TAM-inducible total CD44 knockout in astrocytes.

3.1.2. Genotyping

All newborn mice were routinely genotyped to help select animals for study cohorts and set aside those for future breeding. Genomic Mini kit (A&A Biotechnology, #116-250) was used to purify genomic DNA from mouse tail tissue samples. A 5-mm-long tail sample was immersed in a mixture of 10 mM Tris buffer pH 8.5 (100 µl) with lysis solution (50 µl) and proteinase K (20 µl). Samples were incubated at 50°C overnight or until fully digested. Further purification steps were performed on minicolumns with DNA-binding resin and comprised alternate centrifuging and washing with the provided washing solution. The DNA eluted with sterile water was ultimately used as a polymerase chain reaction (PCR) template.

PCR Mix Plus Red kit (A&A Biotechnology, #2005-100P) was used for the DNA fragment amplification. PCR Mix Plus Red contained *Taq* DNA polymerase, stabilizers, PCR anti-inhibitors, and red dye for easy tracking of electrophoresis. The final composition of the reaction mix is presented in Table 3.1.

Table 3.1. Reaction mix components for the PCR genotyping.

COMPONENT	IN REACTION MIX [25 µl total volume]
2x PCR Mix Plus Red	1x
primer 1	0.2 µM
primer 2	0.2 µM
DNA template	< 250 ng/reaction
ultrapure water	up to 25 µl

Primer sequences (Table 3.2) and PCR conditions (Table 3.3) for genotyping were provided originally with each transgenic line.

Table 3.2. Primer list for PCR genotyping.

TRANSGENE NAME	PRIMER SEQUENCE	PRODUCT SIZE
$CD44^{fl/fl}$	forward 5′GGG AGC ATT GGC TGA CAA CA 3′ reverse 5′TTA CTC TGA TCA TGG CTC TC 3′	WT 292 bp mutant 346 bp
GFAP-Cre^{ERT2}	forward 5′ GCC AGT CTA GCC CAC TCC TT 3′ reverse 5′ TCC CTG AAC ATG TCC ATC AG 3′	mutant ~250 bp

Table 3.3. PCR conditions for the genotyping of transgenic lines.

TRANSGENIC LINE	STEP	TEMPERATURE [°C]	TIME [m:ss]	NUMBER OF CYCLES
$CD44^{fl/fl}$	preheating	97	∞	1
	initial denaturation	94	5:00	
	denaturation	94	1:00	35
	annealing	59	1:00	
	elongation	72	2:00	
	final extension	72	5:00	1
	cooling	4	∞	
GFAP-Cre^{ERT2}	preheating initial denaturation	97 94	∞ 2:00	1
	denaturation	94	0:20	10
	annealing	65	0:15	
	elongation	68	0:10	
	denaturation	94	0:15	28
	annealing	60	0:15	
	elongation	72	0:10	
	final elongation	72	1:00	1
	cooling	4	∞	

PCR products were separated using the agarose gel electrophoresis technique in Tris-Acetate-EDTA pH 8.3 (TAE; Thermo Scientific, #B49) running buffer with Midori Green Advance DNA Stain (NIPPON Genetics EUROPE, #MG04) on 2% agarose gel (80 V constant voltage, 45 min). Two types of controls were used: (i) a positive control (sample with the DNA template from a founder mouse) and (ii) a negative control (reaction mix

without DNA template). Product size was determined based on the used marker – O'GeneRuler 1 kb DNA Ladder, ready-to-use (Thermo Scientific, #SM1163).

3.2. Transgene activation in the TAM-inducible Cre-loxP system

Cohorts of 9- to 17-week-old GFAP-Cre^{ERT2}xCD44$^{fl/fl}$ mice were i.p. injected with 100 µl (per dose) of 10 mg/ml tamoxifen prepared as follows: 10 mg TAM (Sigma-Aldrich, #T5648) + 100 µl ethanol (POCH, #39648011) + 900 µl sunflower seed oil from *Helianthus annuus* (Sigma-Aldrich, #S5007). TAM solution was freshly fixed before administration to each experimental cohort, stored at 4°C, and warmed up to room temperature right before the injection. The administration took place twice a day at regular intervals (every 10-12 hours), for 10 days over 2 weeks (protocol: injections for 5 days → 2-day pause → injections for 5 days). Post-administration time for mouse recovery and activation of Cre-dependent deletion of CD44 lasted 4 weeks. After that time mice were sacrificed for further analysis.

3.3. Surgical procedures

For all surgeries, mice were anesthetized with a mix of ketamine and medetomidine (80mg/kg and 1 mg/kg, respectively; i.p. injection), and then subcutaneously injected with antibiotic (enrofloxacin, 2.5 mg/kg), anti-inflammatory (tolfenamic acid, 2.0 mg/kg), and analgesic (butorphanol, 3.3 mg/kg) drugs. When animals were in a state of deep anesthesia (no reflex movement in response to paw stimulation, no corneal reflex) they were placed in a stereotaxic frame (Stoelting) on a heating pad to maintain a constant body temperature throughout the procedure. The scalp was shaved and disinfected with 3% iodine solution (Apteczka Babuni), and the eyes were protected from drying with 2 mg/g eye gel (Bausch+Lomb). After the skin on the scalp was cut open, positions for drilling holes were determined based on coordinates from a mouse brain atlas (Allen Brain Atlas) and intersections of skull sutures (bregma and lambda). Details of the injections are described in the following sections (see 3.3.1, 3.3.2), as they differed based on the type of the surgical procedure. Each injection was followed by a 15-minute wait time before the micropipette/syringe removal to properly distribute the administered solution in the brain structure.

3.3.1. CD44 transgene activation via AAV vectors

To induce the Cre-mediated *Cd44* recombination, 2-month-old CD44$^{fl/fl}$ mice (male and female) were stereotaxically injected with:

a) AAV serotype 5 vector with inverted terminal repeat (ITR) where a human mini *gfaABC1D* promoter (developed by M. Brenner [179]) drives the expression of enhanced green fluorescent protein (eGFP) attached to the N-terminus of Cre recombinase (AAV5.*gfaABC1D*::eGFP-Cre; construct by Bryan Roth; UNC Vector Core) to produce astrocytic CD44 knockout (**AsKO**) animals, or

b) AAV serotype 5 vector with ITR where a human mini *gfaABC1D* promoter [179] drives the expression of eGFP (AAV5.*gfaABC1D*::eGFP; construct by Bryan Roth; Addgene plasmid #50473; UNC Vector Core) to produce control (**CTRL**) mice.

For more details on the final vector concentration administered into the brain and the GFP immunosignal location visible on immunofluorescence micrographs see Table 3.4.

Table 3.4. Description of AAV vectors used for the transgene activation.

VECTOR NAME	FINAL CONCENTRATION	GFP IMMUNOSIGNAL
AAV5.*gfaABC1D*::eGFP-Cre	2.05×10^{12} vg/ml[1]	in the nucleus
AAV5.*gfaABC1D*::eGFP	4.55×10^{12} vg/ml	in the cytoplasm

AVV vectors were injected into the DG molecular layer of both hippocampi (coordinates: AP –2.0 and ML ±1.4 from bregma, DV –1.5 below the dura; 500 nl per injection), with glass micropipettes (Blaubrand intraMark, #BR708707) at a slow steady rate. Injection sites were confirmed post-mortem before histochemical analysis. In the end, the wound was sutured with absorbable sutures (Braun Novosyn, #1048420), and an anesthetic gel with 20 mg/g lidocaine (Jelfa) was applied to it. Animals were given a 0.5 mg/kg medetomidine reversing agent – atipamezole hydrochloride (CP-PHARMA, Revertor 5 mg/ml), and placed in separate cages on a heating pad until awoken. The recovery time after the surgery lasted 4 weeks.

[1] AAV titer is given as a "physical" titer in viral genomes per ml (vg/ml). It indicates a concentration of the viral vector.

3.3.2. Induction of status epilepticus

The study on the effects of KA-induced SE in $CD44^{fl/fl}$ animals was divided into three experiments:

1) To examine the changes in the *Cd44* expression level during the KA-induced epileptogenesis, 3-month-old $CD44^{fl/fl}$ mice (male and female) underwent intrahippocampal administration of KA. Animals were stereotaxically injected with: (i) 70 nL of 20mM solution of kainic acid (Tocris Bioscience, #0222) in 0.9% sodium chloride (+KA group) or (ii) saline (control) to the left CA1 region of the dorsal hippocampus (coordinates: AP –1.8, ML +1.7, DV –2.1, relative to bregma). Injections were performed at a 50 nl/min flow rate with a NanoFil syringe (World Precision Instruments). Injection sites were confirmed post-mortem before histochemical analysis. In the end, the wound was sutured with absorbable sutures (Braun Novosyn, #1048420), and an anesthetic gel with 20 mg/g lidocaine (Jelfa) was applied to it. Animals were i.p. injected with a 0.5 mg/kg medetomidine reversing agent – atipamezole hydrochloride (CP-PHARMA, Revertor 5 mg/ml), and placed in separate cages on a heating pad until awoken. Mice were sacrificed 4 days after the surgery.
2) To examine the ultrastructural brain alterations caused by the KA-induced epileptogenesis in CD44 AsKO or CTRL animals, 4 weeks after the AAV vector injections $CD44^{fl/fl}$ mice underwent a second surgery for stereotaxic administration of KA. The injection and aftercare were the same as described above. Mice were sacrificed 4 days after the surgery.
3) To induce SE for the EEG analysis, 4 weeks post-AAV vector injections, CD44 AsKO or CTRL animals underwent a second surgery with a stereotaxic administration of KA. The KA injection was the same as described above but mice additionally underwent an electrode implantation procedure (see 3.3.3) before the end of the surgery.

3.3.3. Electrode implantation

Implantation of electrodes was done immediately after KA administration during the surgery session for EEG monitoring. Two stainless-steel screw electrodes (1.6 mm Ø; Bilaney Consultants GmbH) were positioned bilaterally over the frontal cortex, and two more over the cerebellum (reference and ground electrodes). A bipolar hippocampal electrode (Bilaney Consultants GmbH) was implanted into the left hippocampal granular layer of the DG (coordinates: AP –2.0 and ML +1.3 from bregma, DV –1.7 below the dura). The implantation site was confirmed post-mortem. All electrodes were attached to a pedestal (Bilaney Consultants GmbH) and secured with dental acrylate (Duracryl Plus, Spofa Dental, Czech Republic). The skin around the solid dental acrylate was rubbed with the lidocaine gel. After the surgery, mice were given a medetomidine reversing agent (atipamezole hydrochloride 0.75 mg/kg; i.p.) to facilitate awakening from anesthesia.

3.4. Electroencephalography and video monitoring

For simultaneous EEG and video monitoring (vEEG), animals were placed separately in plexiglass cages and connected to a digital acquisition system with commutators (SL6C, Plastic One). vEEG was carried out continuously with TWin Clinical Software for EEG (Grass Technologies) and I-PRO WV SC385 digital cameras (Panasonic) for 4 weeks (24/7). After that, mice were sacrificed and their brain tissue was used for immunohistochemical analysis.

3.4.1. Analysis of the vEEG recording

Spontaneous seizure episodes were analyzed by browsing manually through EEG recordings on a computer screen. An encephalographic episode was defined as a high amplitude (over 2× baseline) discharge lasting ≥ 10 s. The behavioral severity of each detected spontaneous seizure was analyzed from the matching video recordings. Seizure severity was estimated according to Racine [180], Schauwecker and Steward [181], and Ndode-Ekane and Pitkanen [182] with minor modifications: grade 0 — electrographic seizure with no detectable motor manifestation; grade 1 — rigid posture or immobility; grade 2 — stiffened, extended, and often arched tail; grade 3 — partial body clonus, head

bobbing, or whole-body clonic seizures; grade 4 — rearing, severe whole-body continuous clonic seizures while retaining posture; grade 5 — continuous rearing and falling, with severe clonic seizures; grade 6 — generalized tonic-clonic seizures with jumping. Spontaneous seizures were defined as episodes appearing after 24 hours post-KA administration. During the analysis, various parameters were characterized: seizure latency (time to the first spontaneous seizure), frequency (total number of episodes divided by recording days), seizure score (behavioral severity), and average seizure duration.

3.5. Western blot protein analysis

3.5.1. Hippocampal dentate gyrus dissection and tissue preparation

Dissection of the hippocampal dentate gyrus was performed based on the protocol from Hagihara et al. [183] with minor modifications. The animal was anesthetized with isoflurane and sacrificed using a cervical dislocation method. The brain was dissected from the skull and cut along the longitudinal fissure of the cerebrum. Both hemispheres were submerged in RNAlater Stabilization Solution (Invitrogen, #AM7021) overnight at 4°C for easier diencephalon removal and safer tissue storage. After that, dentate gyri were isolated from both hippocampi.

Both dentate gyri from each animal were combined and placed in an ice-cold working solution of RIPA Lysis and Extraction Buffer (Thermo Scientific, #89900) with Phosphatase Inhibitor Cocktail II (Thermo Scientific, #P5726) and SIGMA*FAST*™ Protease Inhibitor Cocktail (Sigma-Aldrich, #S8830). Homogenization was done using the TissueLyser II system (Qiagen) twice for 60 s at 30 Hz. Tissue suspension was then centrifuged at 6000×g for 20 min at 4°C. The supernatant was stored at –20°C for further use.

3.5.2. Determination of protein concentration

For the determination of protein concentration, Pierce™ BCA Protein Assay Kit (Thermo Scientific, #23225) was used. Its detection method uses a 2-step process of

combined reduction of Cu^{2+} to Cu^{1+} by protein in an alkaline medium and selective colorimetric detection of the cuprous cation (Cu^{1+}) by bicinchoninic acid (BCA). The BCA/copper complex exhibits maximum absorbance at 562 nm.

The standard curve was prepared with albumin (BSA, bovine serum) diluted in the lysis buffer solution used for the tissue lysate preparation. All samples and standard points were done in two replicates on a 96-well plate. Absorbance measurements were carried out in a spectrophotometer at 562 nm wavelength. The concentration of each sample was determined based on a standard curve equation.

3.5.3. Electrophoretic protein separation

Lysates were separated based on protein size using the sodium dodecyl sulfate-polyacrylamide gel electrophoresis (SDS-PAGE) system developed by Laemmli [184]. The whole procedure was performed with the Mini-PROTEAN® Tetra Cell system (Bio-Rad). Proteins were separated on 1.5 mm hand-casted 10% TGX™ FastCast™ Acrylamide Kit (Bio-Rad, #1610173) gels prepared according to the enclosed instruction where tetramethylethylenediamine (TEMED; Bio-Rad, #1610800) was used to catalyze acrylamide polymerization.

First, lysates were mixed with Laemmli Sample Buffer (Bio-Rad, #1610747) and incubated for 5-10 min at 95°C. Each well was loaded with 20 μg of the protein sample mix (or 7.5 μg for low-concentration samples), and PageRuler Prestained Protein Ladder (Thermo Scientific, #26616) was loaded as a marker. Electrophoresis was performed in a Tris-Glycine-SDS running buffer (BIORAD, #1610772) at a constant voltage of 80-100 V.

3.5.4. Western blot technique

Protein transfer was done on Trans-Blot Turbo Mini 0.2 μm PVDF Transfer Packs (Bio-Rad, #1704156) containing filter paper, transfer buffer, and 0.2 μm polyvinylidene difluoride (PVDF) membrane. The transfer was performed using the semi-dry Trans-Blot Turbo Transfer system (Bio-Rad) at 1.3 A, 25 V for 10 min. Next, the membrane was incubated in a 5% NFDM blocking buffer [5% non-fat dry milk (NFDM) in Tris-buffered saline (TBS; Merck, #T5912) with 0.05% Tween 20 (BioShop, #TWN510)] for 1 hour after

which it was left overnight at 4°C in a primary antibody in 5% NFDM blocking buffer. The next day, the membrane was washed 3 × 10 min with TBS + Tween 20 and incubated for 2 hours in horseradish peroxidase-conjugated (HRP-conjugated) secondary antibody in 5% NFDM blocking buffer. The detailed list of all used antibodies is presented in Table 3.5. After the incubation, the membrane was washed 3 × 10 min with TBS + Tween 20, and then protein signals were detected on an X-ray film with Amersham™ ECL Prime Western Blotting Detection Reagent (GE Healthcare, #28980926).

Table 3.5. List of antibodies used for Western blotting.

PRIMARY ANTIBODIES			
Immunogen	**Host Species & Isotype**	**Supplier, Catalog Number**	**Working Concentration**
CD44	sheep IgG	R&D Systems, AF6127	1:2500
GAPDH	rabbit IgG	Abcam, ab9485	1:5000
SECONDARY HRP-CONJUGATED ANTIBODIES			
Reactivity	**Host Species & Isotype**	**Supplier, Catalog Number**	**Working Concentration**
sheep	donkey IgG	R&D Systems, HAF016	1:5000
rabbit	goat IgG	Abcam, ab97051	1:10000

3.5.5. Densitometric analysis of protein expression

For densitometric calculations, a scan of the X-ray film was analyzed using Ohgane and Yoshioka's Band/Peak Quantification macro/plugin [185] available for Fiji software [186], which automatically estimates background level based on the mean or median intensity around a boundary of the ROI. CD44 protein expression level was normalized to glyceraldehyde-3-phosphate dehydrogenase (GAPDH).

3.6. Immunohistochemistry of brain slices

3.6.1. Tissue preparation

Animals were first anesthetized with isoflurane, then intraperitoneally injected with pentobarbital (100 mg/kg) for deep anesthesia. Transcardial perfusion was done with phosphate-buffered saline pH 7.4 (PBS; Merck, #524650) to clear out blood from the circulatory system, followed by 4% paraformaldehyde (PFA; Sigma-Aldrich, #8187151000) to preserve the brain for immunostaining. Brains were dissected and post-fixed in 4% PFA overnight at 4°C, submerged in 30% sucrose solution for 24 hours at 4°C for cryopreservation, then embedded in Tissue Freezing Medium (Leica, #14020108926) for cryosectioning, snap-frozen in isopentane, and stored at –80°C before cutting. After cryosectioning, 40-µm-thick coronal brain slices were stored in an anti-freeze medium [0.1 M phosphate buffer pH 7.4 + 30% ethylene glycol + 20% glycerol] at –20°C.

3.6.2. Immunohistochemical staining

Free-floating brain slices were washed for 3 × 10 min with PBS. To recover antigen reactivity, heat-induced epitope retrieval (HIER, antigen retrieval) in a pre-heated sodium citrate buffer pH 6.0 [10mM sodium citrate + 0.05% Tween 20 (BioShop, #TWN510)] was performed for 30 min at 80℃. After cooling down to room temperature, slices were washed for 3 × 10 min with phosphate-buffered saline pH 7.4 + 0.1% Triton X-100 (PBST) and then blocked in 5% normal donkey serum in PBST (NDST) for 1 hour. A subsequent overnight incubation with the primary antibody in 5% NDST was carried out at 4℃. The next day, slices were washed for 3 × 5 min and 2 × 10 min with PBST, followed by a 2-hour incubation with the secondary antibody in 5% NDST. For complex stainings with more than one protein target, the procedure was repeated without antigen retrieval and blocking steps. The detailed list of used antibodies is shown in Table 3.6. After incubations, slices were washed for 3 × 5 min and 2 × 10 min with PBST and co-stained with Hoechst nuclear stain (1:500; Invitrogen, H3570) in PBST for 10 min. In the end, slices were washed

again for 3 × 10 min with PBST, mounted on glass slides with VECTASHIELD Antifade Mounting Medium without DAPI (Vector Laboratories, #H1000), and stored at –20°C.

Table 3.6. List of antibodies used for immunohistochemistry.

PRIMARY ANTIBODIES			
Immunogen	**Host Species & Isotype**	**Supplier, Catalog Number**	**Working Concentration**
CD44	sheep IgG	R&D Systems, AF6577	1:500
GFAP	chicken IgG	Abcam, ab4674	1:500
s100β	rabbit IgG	Abcam, ab52642	1:100
ZnT3	rabbit IgG	Synaptic Systems, 197002	1:500

SECONDARY ANTIBODIES			
Reactivity, Conjugate	**Host Species & Isotype**	**Supplier, Catalog Number**	**Working Concentration**
sheep IgG, Alexa Fluor 488	donkey IgG	Invitrogen, A-11015	1:500
sheep IgG, Alexa Fluor 555	donkey IgG	Invitrogen, A-21436	1:500
chicken IgG, Alexa Fluor 647	donkey IgG	Jackson ImmunoResearch, 703-606-155	1:500
rabbit IgG, Alexa Fluor 647	donkey IgG	Jackson ImmunoResearch, 711-606-152	1:500

3.6.3. Fluorescent microscopy imaging

Microscopic imaging of fluorescent specimens was done using Leica AF 7000 fluorescent microscope (objective lenses: HCX PL APO 10.0×/0.40 DRY, HCX PL APO 20.0×/0.70 DRY) and Zeiss LSM 800 with Airyscan confocal microscope (objective lenses: EC Plan-Neofluar 10x/0.30, Plan-Apochromat 63x/1.40 Oil DIC M27). The fluorescent microscope's Leica LAS AF software was used to set up the tile scanning of large areas (e.g., a whole hippocampus) and automatic tile stitching. Setup of the sequential image

acquisition of multichannel Z-stack scans on the confocal microscope was done with the Zeiss ZEN 2.6 software. Scan setups were consistent for all samples in each experiment. Confocal image stacks of the hippocampal hilus were acquired with a dry 10x objective (36 µm depth, 3.84 µm interval, 0.33 µm pixel size, 2424×2424 resolution). Stacks from the oil 63x objective (multiple depths, 0.20 µm interval, 0.08 µm pixel size, 1024×1024 resolution) were collected from the granular and inner molecular layers of the hippocampal DG.

3.6.4. Fluorescent microscopy image analysis

Images were analyzed with Fiji software as maximum projections of the z-plane stacks. Fractions of virally transfected astrocytes were calculated from s100 calcium-binding protein β (s100β)-immunostained slices. For the astrogliosis evaluation, the area of astrocytes was determined by outlining individual astroglial cells observed as a GFAP immunosignal. Because GFAP protein is localized mostly in the soma, major primary, and secondary branches [187, 188], undetectable terminal astrocytic processes are excluded in this analysis. Mossy fiber sprouting was analyzed by particle counting of zinc transporter 3 (ZnT3) immunopositive puncta, excluding all objects with a diameter below 0.5 µm (the minimum size of a mossy fiber terminal) [189, 190]. The percentage of MFS was calculated with the formula: (area of ZnT3-immunopositive puncta / area of the examined layer) × 100. Comparative analyses were performed only in the case of images taken with the same acquisition parameters.

3.7. **Three-dimensional serial block-face scanning electron microscopy**

3.7.1. SBEM tissue preparation and staining

Animals were first anesthetized with isoflurane, then intraperitoneally injected with pentobarbital (100 mg/kg) for deep anesthesia. Transcardiac perfusion was done with PBS to clear out blood from the circulatory system, followed by 4% PFA + 2.5% glutaraldehyde (GA; Sigma-Aldrich, #G5882) in PBS to preserve the tissue for electron microscopy. Brains were dissected and post-fixed by immersion in the same

fixative overnight at 4°C, then cut into 100-μm-thick coronal sections on a vibratome and stored in PBS with 0.1% sodium azide (Sigma-Aldrich, #2002) at 4°C. The molecular layer region of the hippocampus was cut out from each slice, along with a small piece of granular layer for orientation, with a razor blade.

Sample staining was performed according to the rOTO and Walton's lead aspartate staining protocol kindly provided by Prof. Christel Genoud (University of Lausanne), which is a slightly modified version of Deerinck's et al. protocol of *en bloc* staining for SBEM [191]. It was designed to accentuate the membrane contrast and improve the signal for backscatter electron imaging of epoxy-embedded mammalian tissue at low accelerating voltages. Small fragments (< 2×2 mm) of the ML of the DG, along with a part of the granular layer for orientation, were cut out from the coronal slices and washed for 5 × 3 min in cold 0.1 M phosphate buffer pH 7.4 (PB). They were postfixed in a freshly prepared solution of 1.5% potassium ferrocyanide (Sigma-Aldrich, #P3289) with 2% aqueous osmium tetroxide (Electron Microscopy Sciences, #19150) in PB for 1 hour on ice. Next, samples were washed for 5 × 3 min with double-distilled (dd) H_2O and immersed in a freshly prepared and filtered 1% aqueous thiocarbohydrazide (Sigma-Aldrich, #223220) solution for 20 min. Afterward, tissues were rinsed for 5 × 3 min with dd H_2O, postfixed in 2% aqueous osmium tetroxide for 30 min, and rinsed again for 5 × 3 min with dd H_2O. Then, they were left for an overnight incubation in 1% aqueous uranyl acetate. The next day, samples were washed for 5 × 3 min with dd H_2O and immersed in a freshly prepared lead aspartate aqueous solution pH 5.5 [0.066 g lead nitrate (Electron Microscopy Sciences, #17800) + 10 ml dd H2O + 0.04 g aspartic acid pH 3.8 (Thermo Scientific, # 105045000)] for 20 min at 60°C, then washed again for 5 × 3 min with dd H_2O. Next, they were dehydrated using graded dilutions of ethanol (POCH, #39648011) – 20%, 50%, 70%, 100%, $100\%_{anhydrous}$ – for 5 min each. After the last ethanol incubation, fragments were infiltrated with a 1:1 (v/v) solution of Durcupan resin (Sigma-Aldrich, #44610) with anhydrous ethanol for 30 min, and then 100% Durcupan resin for another 1 h. The resin was then replaced with a fresh one and left to incubate overnight. The next day, Durcupan resin was replaced again for an additional 1 h infiltration, after which samples were flat embedded between Aclar sheets (Electron Microscopy Sciences, #50425), and put in an oven at 65°C for at least 48 h for the resin to

polymerize. After the resin hardened, Aclar sheets were separated and the resin-embedded pieces were taken out, glued to aluminum pins (Gatan 3View system Scanning Electron Microscopy pin stubs, Micro to Nano, #10-002-006-50), and trimmed both on the ultramicrotome (Leica Ultracut R) and manually with a razor blade. Before mounting in the microscope's chamber, samples were covered with conductive silver paint (Ted Pella, #16034).

3.7.2. SBEM imaging

Sample imaging was done with SigmaVP (Zeiss) scanning electron microscope equipped with the 3View2 chamber (Gatan) using a backscatter electron detector. DigitalMicrograph software was used to set the same imaging settings for all scanned samples: 2.5 kV EHT, 20 μm aperture, 7-9 Pa variable pressure, 15000× magnification, 7 μs pixel dwell time, 5x5 nm pixel size (3072×3072 camera array). Scans were taken in the ML of the hippocampal DG. Every collected image stack comprised 200 sections (60 nm slice thickness).

3.7.3. SBEM image processing and analysis

Scans were aligned using the TrakEM plugin in Fiji software and normalized with Microscopy Image Browser software [192]. The reconstruction of synaptic connections and astrocytic leaflets was done using Reconstruct software [193]. For 3D reconstruction, areas from each sample taken for analysis were randomly picked and processed using the unbiased brick method [194]. For every specimen, reconstructed structures were limited to bricks of size 6 μm × 6 μm × 6 μm. Dendritic spines were defined as dendritic protrusions having an electron-dense region, the approximate core of post-synaptic density (PSD), close to the membrane adjacent to an axonal bouton with synaptic vesicles. Astrocytes and their leaflets were identified by characteristic features: an irregular stellate shape, numerous glycogen granules, bundles of intermediate filaments, or a relatively clear cytoplasm. After identifying and reconstructing PSD areas, dendritic spines, and axonal boutons, parts of astrocytic leaflets located in their proximity were drafted. PSD surface area and volume were measured by outlining darkened electron-dense regions on

every section with a particular PSD. Following the work of Ostroff et al. [195], an astroglial leaflet localized in a proximity ≤ 20 nm from a PSD was considered as one having contact with the synapse. Reconstruct software was used to extract PSD parameters and PSD to leaflet distance.

3.8. **Statistical analysis**

Data statistical analysis was performed using GraphPad Prism software (GraphPad Software Inc.). All data were tested for normal distributions with the Shapiro-Wilk test. Differences in semiquantitative scores between groups were analyzed using Fisher's test. For other comparisons, the following tests were used: the parametric Student's t-test (groups with equal variances), Student's t-test with Welch's correction or Welch's ANOVA (groups without equal variances) for data with symmetric distribution; the nonparametric Mann–Whitney test for data with asymmetric distribution; or two-way ANOVA test. Data on graphs are presented as mean ± standard error of the mean (S.E.M.) in parametric analyses or as median with interquartile range (IQR) in nonparametric analyses. Differences between groups were considered significant if p-value < 0.05, where levels of significance were flagged as follows: $p<0.05$ (*), $p<0.01$ (**), $p<0.001$ (***). All figures were prepared using Inkscape (Free and Open Source Software licensed under GPL).

4. RESULTS

4.1. Generation of conditional TAM-inducible total astrocyte-specific CD44 knockout mice using the Cre-loxP system

The function of astrocytic CD44 in adult mice is still quite unknown. To better understand the impact of CD44 depletion in the brain, a double transgenic line was generated where a conditional deletion of CD44 in astrocytes could be induced with TAM under Cre-loxP system control. The initial goal was to create animals in which a total deletion of CD44 in astrocytes in the brain could be achieved in a time-controlled manner using repeated intraperitoneal TAM injections activating the Cre-loxP system.

4.1.1. Breeding strategy for the generation of a GFAP-Cre^{ERT2}xCD44$^{fl/fl}$ mouse

To generate a mouse with the desired experimental genotype of TAM-inducible total knockout of CD44 in astrocytes (referred to in the text as GFAP-Cre^{ERT2}xCD44$^{fl/fl}$), a series of crossbreeding of heterozygous and homozygous animals was required. An animal with a homozygous genotype has two identical copies (alleles) of a gene, whereas one with a heterozygous genotype has two different alleles of a gene. For a better description, in this subsection, a plus sign "+" next to the genotype name will represent a modified allele, and a minus sign "-" will represent an unmodified allele (i.e., homozygote +/+, heterozygote +/-, no transgene -/-).

First, a homozygous CD44$^{fl/fl(+/+)}$ female was crossed to a heterozygous GFAP-Cre$^{ERT2(+/-)}$ male (Figure 4.1). Following classical Mendelian genetics, half of the offspring would inherit the GFAP-Cre$^{ERT2(+/-)}$ genotype, and all pups would receive a single copy of the floxed *Cd44* allele (CD44$^{fl/fl(+/-)}$). Next, a sexually mature (around 8 weeks old) heterozygous GFAP-Cre$^{ERT2(+/-)}$xCD44$^{fl/fl(+/-)}$ male was backcrossed to a homozygous CD44$^{fl/fl(+/+)}$ female resulting in 25% of the offspring having the desired GFAP-Cre$^{ERT2(+/-)}$xCD44$^{fl/fl(+/+)}$ genotype (astrocyte-specific heterozygous Cre and homozygous double loxP-floxed CD44 mice).

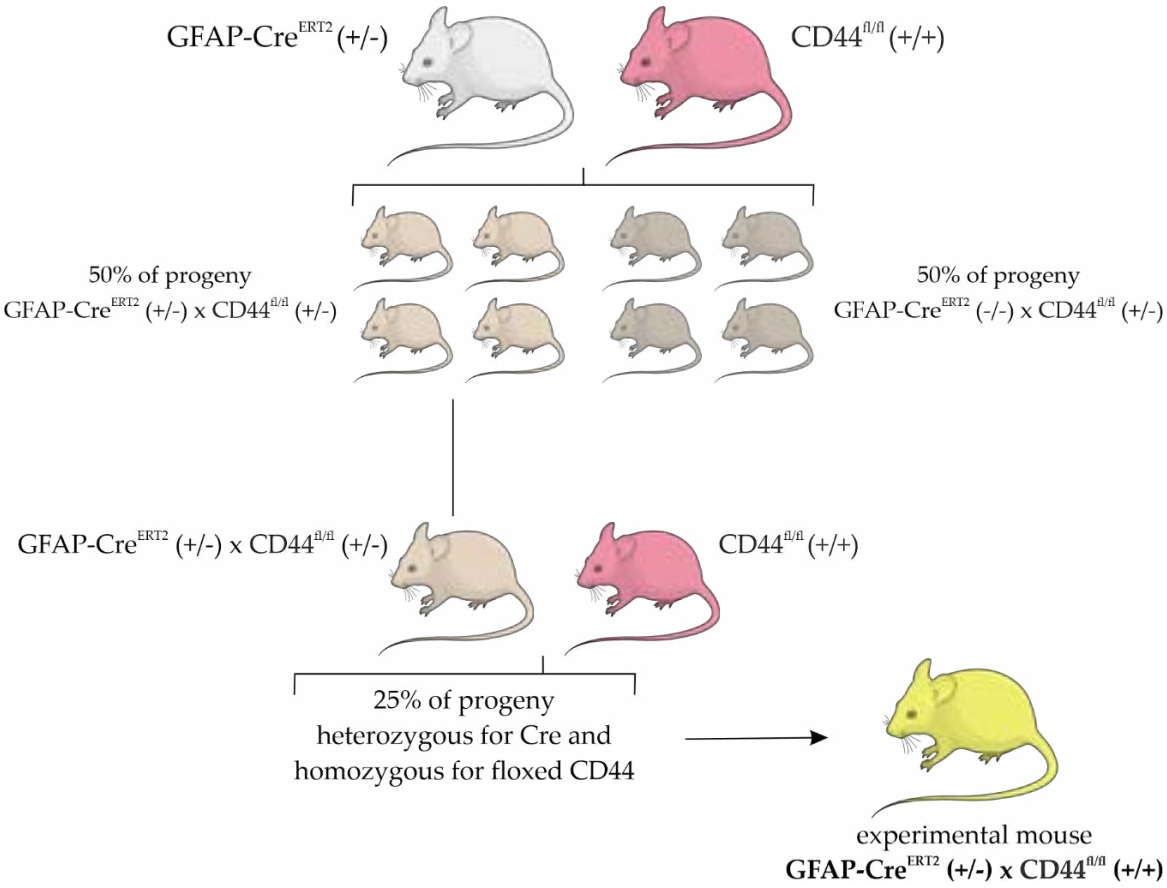

Figure 4.1. Breeding strategy for generating astrocyte-specific CD44 knock-out mice. To generate a GFAP-CreERT2xCD44$^{fl/fl}$ mouse, first, a heterozygous GFAP-Cre^{ERT2} male is bred with a homozygous CD44$^{fl/fl}$ female resulting in 50% chances of the pups inheriting GFAP-Cre^{ERT2} transgene and all pups inheriting one copy of the floxed *Cd44* allele (CD44$^{fl/fl}$ heterozygotes). Next, a male with both heterozygous GFAP-Cre^{ERT2} and CD44$^{fl/fl}$ transgenes is crossed with a homozygous CD44$^{fl/fl}$ female resulting in 25% chances of generating a pup with the genotype necessary to conditionally knock out CD44 in astrocytes.

4.1.2. Verification of CD44$^{fl/fl}$ and GFAP-Cre^{ERT2} genotypes

Before cross-breeding, CD44$^{fl/fl}$ and GFAP-Cre^{ERT2} litters were genotyped postnatally with PCR based on total DNA isolated from tail biopsies of approximately 21-day-old mice. The amplified DNA fragments were separated by the agarose gel electrophoresis to provide precise genotype identification (Figure 4.2).

Animals from the CD44$^{fl/fl}$ line were born: (i) homozygotes with two equally altered *Cd44* gene alleles (346 bp single band), (ii) heterozygotes with different copies (alleles) coding for CD44 (294 bp and 346 bp double band), or (iii) wild types (WTs) without any gene alteration (292 bp single band). As the GFAP-Cre^{ERT2} line was maintained heterogeneous, the transgene was detected by the presence of a single band (~250 bp) on

a gel. WT mice without the GFAP-Cre^{ERT2} transgene, as well as negative controls that did not contain DNA matrix, gave blank results.

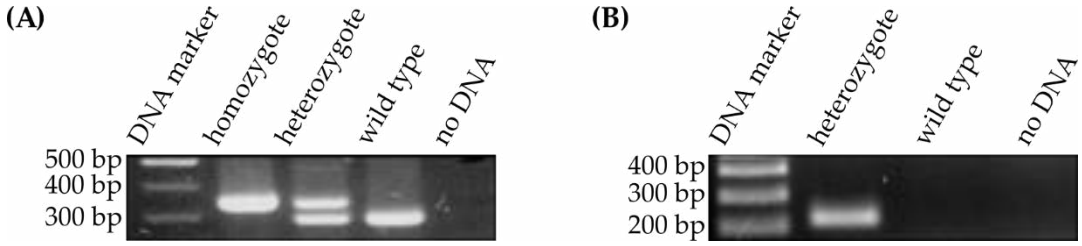

Figure 4.2. PCR amplification of genotype-specific DNA fragments. (A) PCR amplification of CD44$^{fl/fl}$ mice where a single upper (346 bp) band corresponds to a homozygous genotype, a double (294 bp + 346 bp) band corresponds to a heterozygous genotype, and a lower single (294 bp) band indicates a WT animal. (B) PCR amplification of GFAP-Cre^{ERT2} mice where a single (~250 bp) band corresponds to a heterozygous genotype, and an absence of any detectable signal indicates a WT animal. Negative control (no-DNA sample) gave no signal in either case.

GFAP-Cre^{ERT2}xCD44$^{fl/fl}$ animals were genotyped twice based on two separate reactions described above to verify both the presence of the *Cd44* loxP-flanked gene and the GFAP-Cre^{ERT2} gene sequence.

4.1.3. Tamoxifen administration in GFAP-Cre^{ERT2}xCD44$^{fl/fl}$ mice

Double transgenic GFAP-Cre^{ERT2}xCD44$^{fl/fl}$ animals with astrocyte-specific inducible Cre^{ERT2} were intraperitoneally injected with tamoxifen (details in subsection 3.2). CreERT2 remains in the cytosol in an inactive form bound by heat shock protein 90 (HSP 90). After administration, TAM binds to CreERT2 releasing HSP90 from the complex. In the nucleus, the active complex of CreERT2 and TAM recognizes and binds to loxP sequences flanking exon 3 of the *Cd44* gene which is ultimately cut out. Exon 3 cleavage leads to a rise of a new stop codon in the protein sequence resulting in the production of a shortened non-functional CD44 protein. The graphical representation of the Cre-mediated modification of *Cd44* is shown in Figure 4.3.

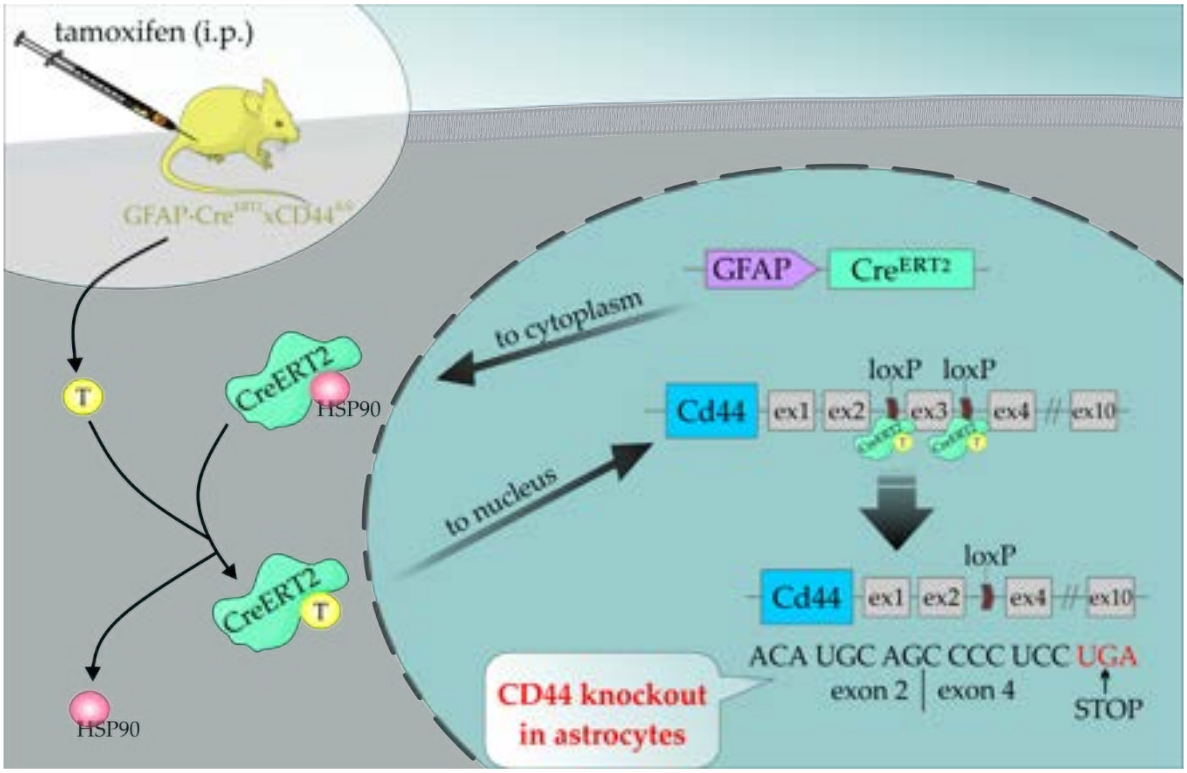

Figure 4.3. Astrocyte-specific knockout of CD44 using TAM-inducible Cre-loxP system. CreERT2 recombinase is expressed under the astrocyte-specific GFAP promoter. The inactive form of CreERT2 is sequestered in the cytoplasm by heat shock protein 90 (HSP90) and becomes activated when bound to the administered tamoxifen (T). In the nucleus, the CreERT2-T complex recognizes and binds to loxP sites activating the cleavage of the floxed exon 3 (ex3) of the *Cd44* gene. This leads to the inability to produce a fully functional CD44 protein.

4.1.4. Validation of the Cre-loxP system action

The analysis of the Cre-loxP system was performed to verify its action *in vivo* in animals from the GFAP-Cre^{ERT2}xCD44$^{fl/fl}$ line. After 4 weeks, needed for the mouse recovery and activation of Cre-dependent depletion of CD44, mice were sacrificed. I conducted an immunohistochemistry analysis using the anti-CD44 antibody to visualize CD44 expression in astrocytes in the ML (Figure 4.4-A). Additionally, another cohort was used for the Western blot analysis (Figure 4.4-B,C). Western blot showed no differences in the CD44 expression between TAM-injected GFAP-Cre^{ERT2}xCD44$^{fl/fl}$ animals and controls.

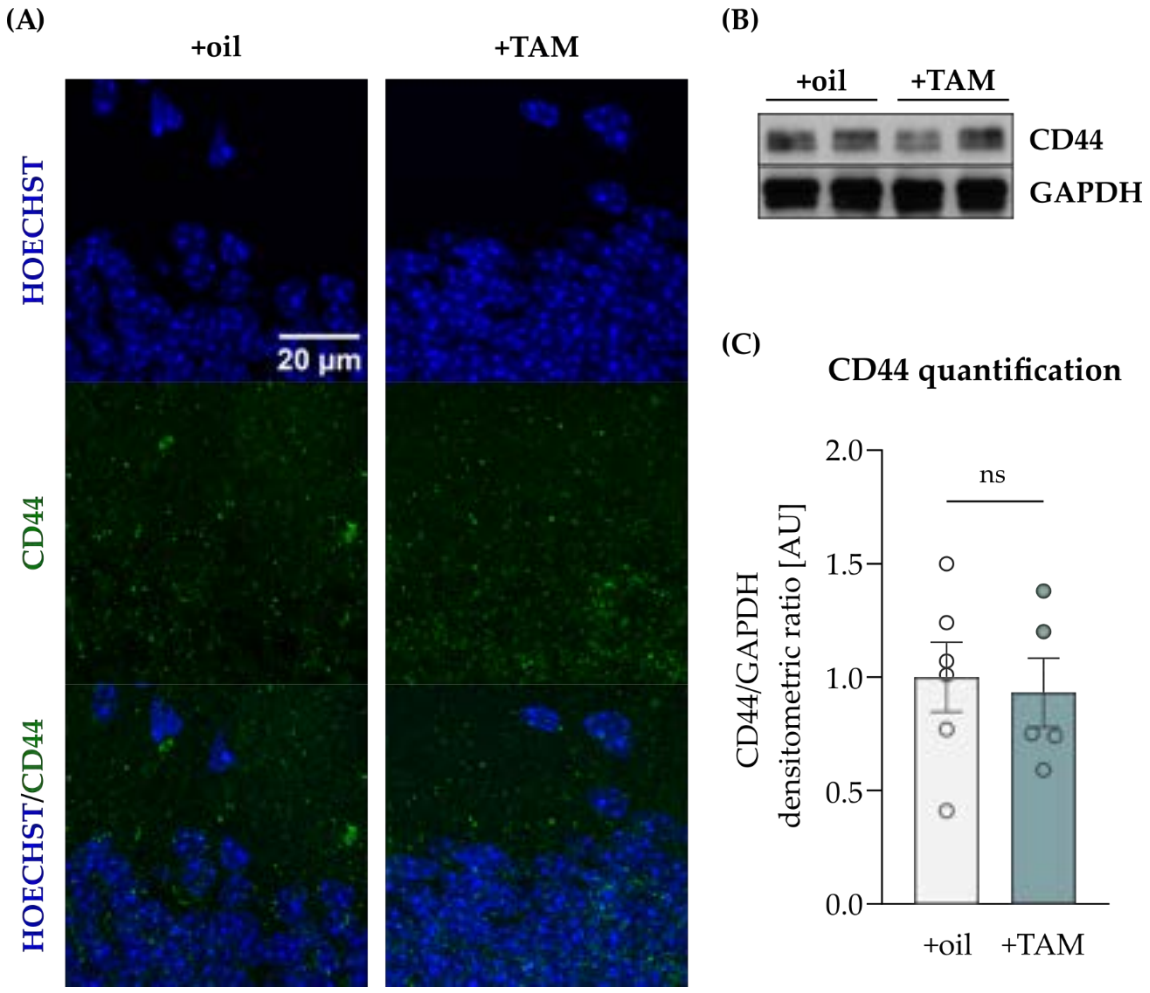

Figure 4.4. Validation of the TAM-induced Cre-loxP system action in $Cre^{ERT2}xCD44^{fl/fl}$ mice. (**A**) High-power view of the ML in close proximity to GCL, immunostained for CD44 (green) and Hoechst (nuclei, blue) in oil- or TAM-injected mice. Scale bar: 20 µm. (**B**) CD44 level in protein extracts from DG of GFAP-$Cre^{ERT2}xCD44^{fl/fl}$ animals (Western blot). GAPDH was used as the loading control protein. (**C**) Quantitative analysis of Western blot results (Student's t-test, p=0.763, data presented as mean ± S.E.M.).

The injection model has been modified in terms of the time of TAM exposure (5 constitutive days) or duration of mouse recovery and activation of the Cre-loxP system (8 weeks), but no significant changes have been achieved.

These results demonstrate that the conditional TAM-inducible Cre-loxP system is not reliable for generating a total astrocyte-specific CD44 knockout mouse line and using it for the experiments to follow.

4.2. Generation of animals with astrocytic CD44 depletion through the AAV5-mediated expression of *gfa*ABC1D::eGFP-Cre recombinase in the hippocampi of CD44$^{fl/fl}$ mice

The lack of CD44 deletion phenotype in GFAP-Cre^{ERT2}xCD44$^{fl/fl}$ line compelled me to look for another model of CD44 depletion in astroglia. I focused on an AAV-mediated expression of Cre recombinase where the deletion of CD44 in astrocytes in the brain could be achieved in a site- and time-controlled manner. This genetic approach allowed for a deletion of CD44 specifically in hippocampal astrocytes, which was crucial, as the hippocampus is the essential brain area in the development of TLE.

This approach was performed by a stereotaxic delivery of an adeno-associated viral serotype 5 (AAV5) vector carrying Cre recombinase into the molecular layer of the dentate gyrus in CD44$^{fl/fl}$ mice (Figure 4.5-A). The Cre recombinase, N-terminally appended with eGFP as a fluorescent marker, was expressed in astrocytic nuclei under the control of the astrocyte-specific GFAP promoter. In the figures, these mice are referred to as AsKO. As a control (CTRL), CD44$^{fl/fl}$ mice were injected with AAV5 encoding only eGFP under the GFAP promoter, leading to eGFP expression in the astrocytic cytoplasm. To assess viral transduction efficiency, I measured the percentage of s100β-positive cells that were also eGFP-positive. The analysis showed transduction efficiencies of 84.1 ± 3.51% for AAV5.*gfa*ABC1D::eGFP and 74.22 ± 3.07% for AAV5.*gfa*ABC1D::eGFP-Cre (data presented as mean ± S.E.M.).

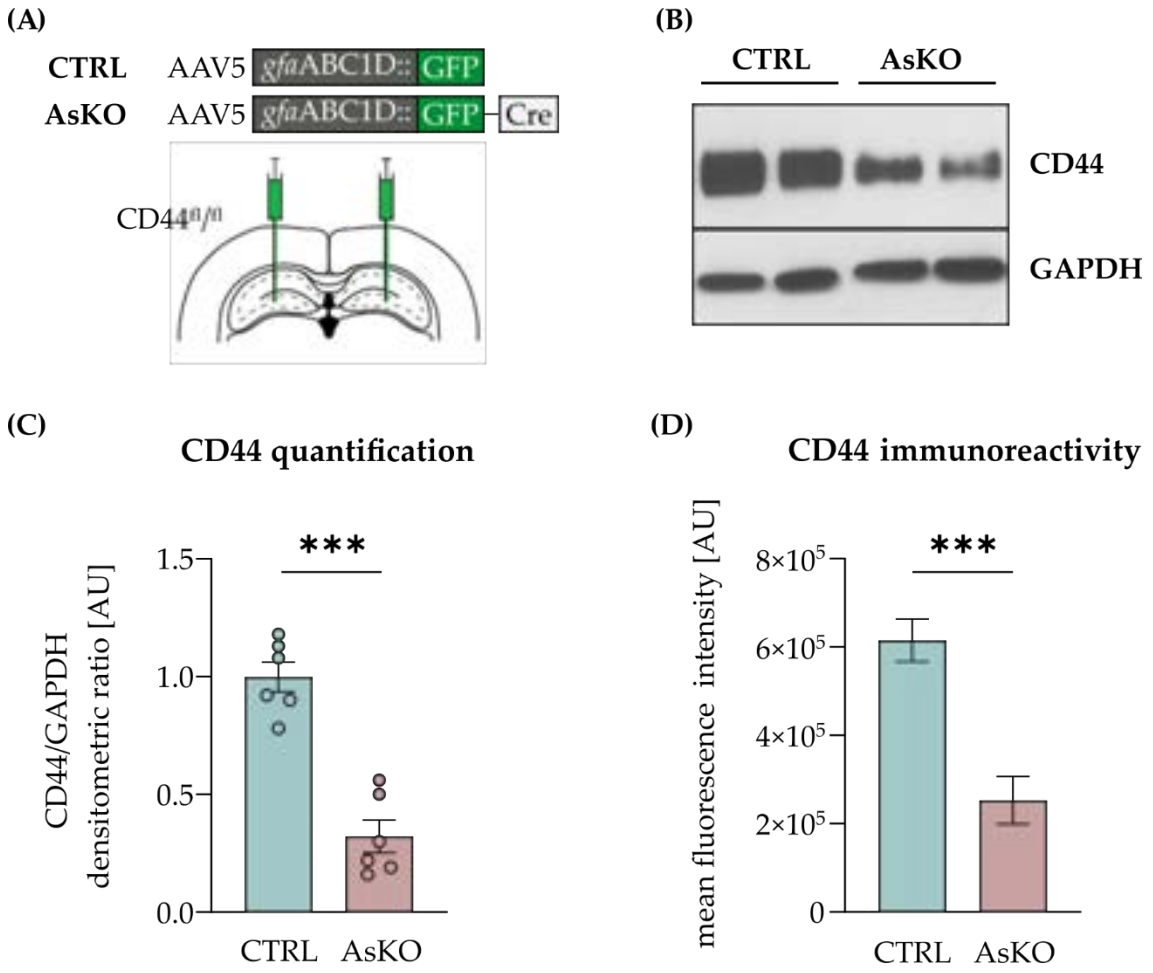

Figure 4.5. GFAP-Cre recombinase viral approach to target CD44 in adult dentate gyrus astrocytes and its analysis. (**A**) Scheme of the bilateral intrahippocampal administration of AAV vectors (CTRL: AAV5.*gfa*ABC1D::eGFP; eGFP localizes in the cytoplasm of astrocytes, and AsKO: AAV5.*gfa*ABC1D::eGFP-Cre; eGFP-Cre localizes in cell nuclei of astrocytes) into the brains of $CD44^{fl/fl}$ mice. (**B**) CD44 level in protein extracts from the DG of CTRL and AsKO animals (Western blot). GAPDH was used as the loading control protein. (**C**) Quantitative analysis of Western blot results (n=6 independent animals, Student's t-test, ***p<0.001, data presented as mean ± S.E.M.). (**D**) CD44-immunoreactivity in astrocytic s100β profiles from the ML of the DG in CTRL and AsKO mice (Student's t-test, ***p<0.001, data presented as mean ± S.E.M.). See Figure 4.6 for representative immunofluorescence micrographs.

Four to five weeks after AAV injection, Western blot analysis revealed a significant reduction of CD44 expression in the dentate gyrus of Cre recombinase-expressing mice compared to controls (see Figure 4.5-B,C). Immunohistochemical analysis confirmed decreased CD44 expression in infected astrocytes (stained with anti-s100β antibody) in the molecular layer of the dentate gyrus in the AsKO group, unlike the CTRL group (Figure 4.5-D and Figure 4.6).

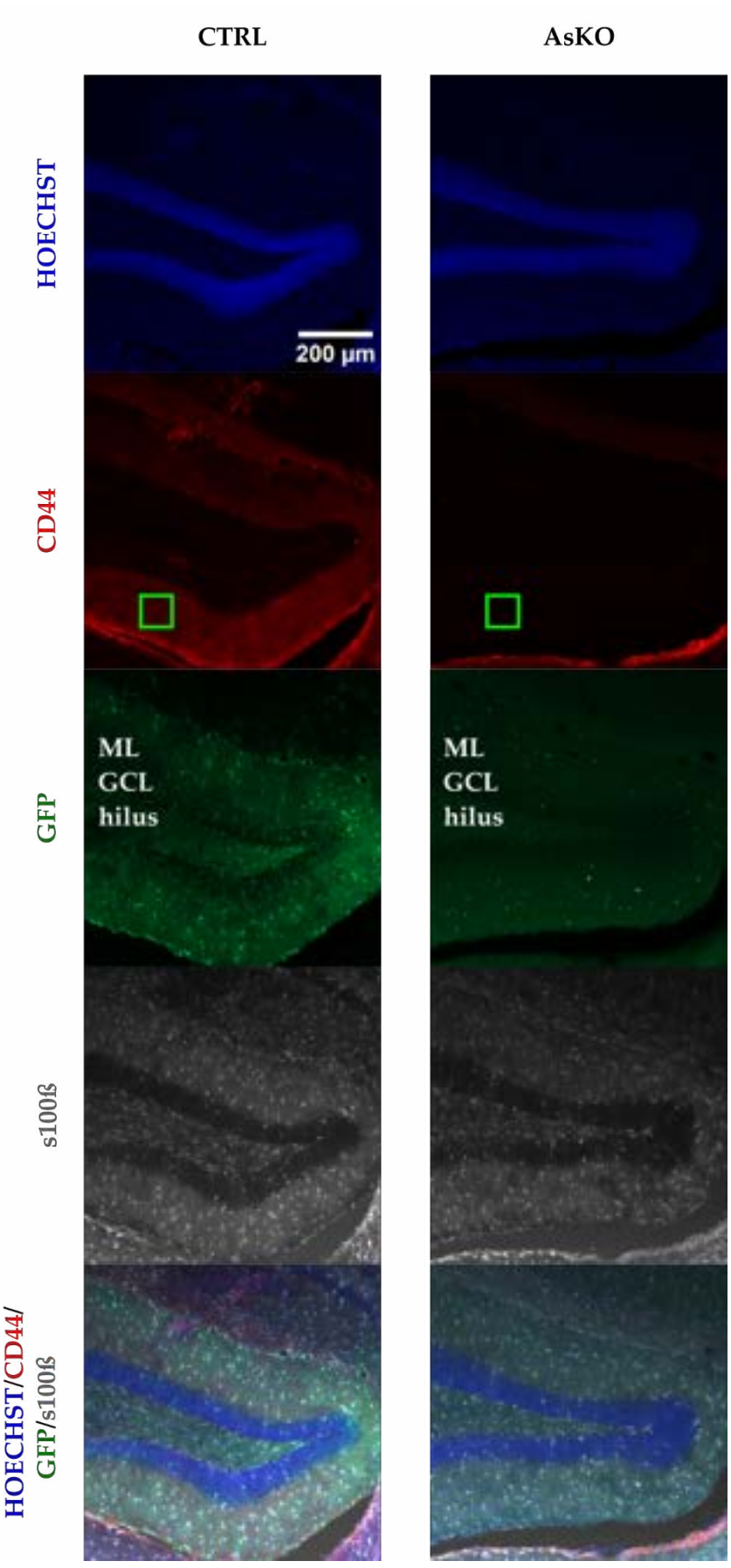

(B)

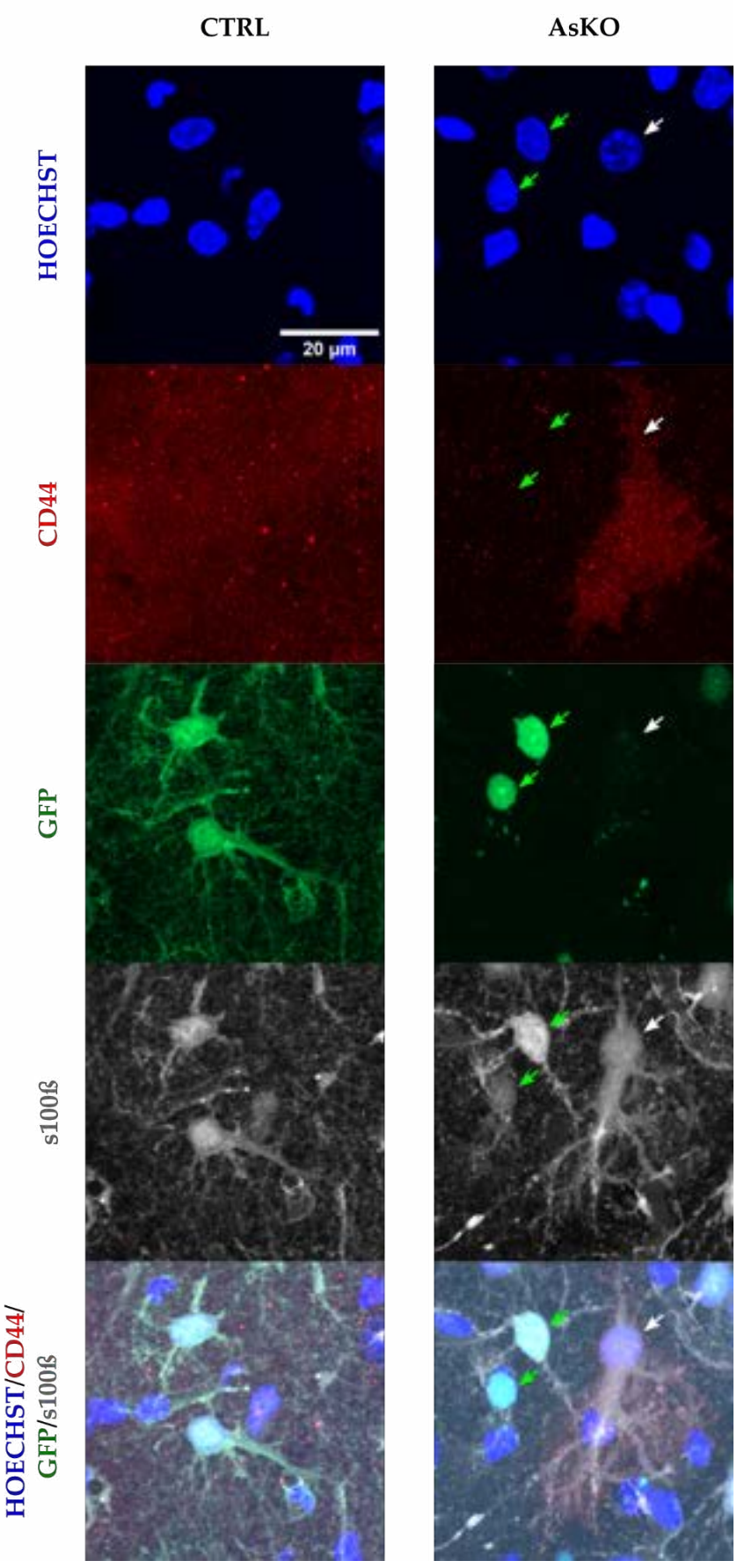

Figure 4.6. Immunofluorescence micrographs of the AAV5-mediated astrocytic CD44 depletion in the hippocampus of CTRL and AsKO mice. Representative images of CD44 (red), GFP (green), s100β (astrocyte, white), and Hoechst (nuclei, blue) expression 4 weeks after GFAP-Cre recombinase injection with matching triple stain images shown at (**A**) a lower magnification or (**B**) the close-ups reflecting green squares on panel (A). Arrows point to astrocytes (s100β staining) – green arrow for GFP-expressing and white arrow for non-expressing, respectively. ML—molecular layer, GCL—granular layer. Scale bar: (A) 200 μm and (B) 20 μm.

Those results show that the AAV5-mediated expression of *gfa*ABC1D::eGFP-Cre recombinase leads to the deletion of CD44 in the hippocampal astrocytes of $CD44^{fl/fl}$ mice.

4.3. Determination of the CD44 receptor role in epileptogenesis using kainate-induced *status epilepticus* model in $CD44^{fl/fl}$ mice

The next phase was to study the CD44 role in epileptogenesis in mice with its astrocytic knockout. The $CD44^{fl/fl}$ mouse line, intrahippocampally injected with AAV-mediated Cre recombinase, provided sufficient deletion of astrocytic CD44 in the hippocampal formation. This design allowed for a local CD44 depletion in the hippocampus and analysis of the structural and ultrastructural alterations caused by the KA-induced SE. The general scheme of the experimental procedure is shown in Figure 4.7.

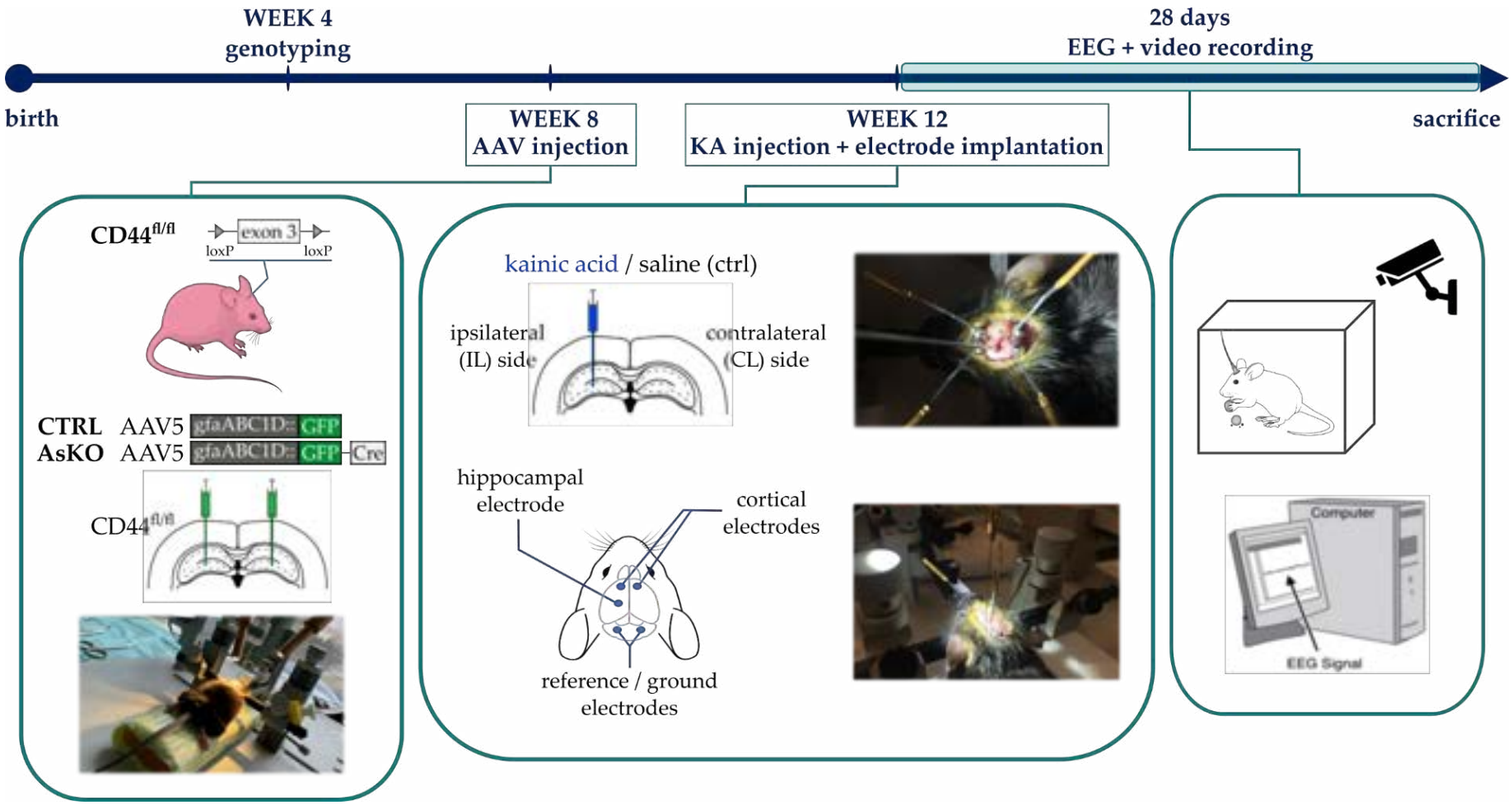

Figure 4.7. A scheme of the overall experimental procedure for KA-induced SE in CD44$^{fl/fl}$ mice. 8-week old CD44$^{fl/fl}$ mice were intrahippocampally injected with AAV-vectors (CTRL: AAV5.*gfa*ABC1D::eGFP; AsKO: AAV5.*gfa*ABC1D::eGFP-Cre) and left for recovery and mutation activation for 4 weeks. Then, animals were injected with KA into the left side of the hippocampus and implanted with EEG electrodes. Immediately after the surgery, all mice were placed in separate cages, plugged into the 24-hour EEG monitoring system, and video recorded for the next 28 days.

4.3.1. CD44 expression analysis in mice with KA-induced SE

Studies show that KA-induced SE is strongly associated with the increased abundance of CD44 in astrocytes [142, 196]. In this study, the first step on the path to investigate the role of CD44 in epilepsy development and progression was verifying if and how its expression changes in the hippocampus of the $CD44^{fl/fl}$ mouse line (without active CD44 knockout) following KA-induced seizures. SE was triggered in $CD44^{fl/fl}$ mice via intrahippocampal KA injections (n=4 per group). Sham saline injections served as controls to account for mechanical injury caused by the needle and fluid infusion. This model closely mimics many morphological and functional features of TLE in humans [165]. Immunohistochemical staining was performed on 4-day post-surgery slices, using anti-CD44 and anti-GFAP antibodies to visualize CD44 expression in astrocytes (Figure 4.8 and Figure 4.9).

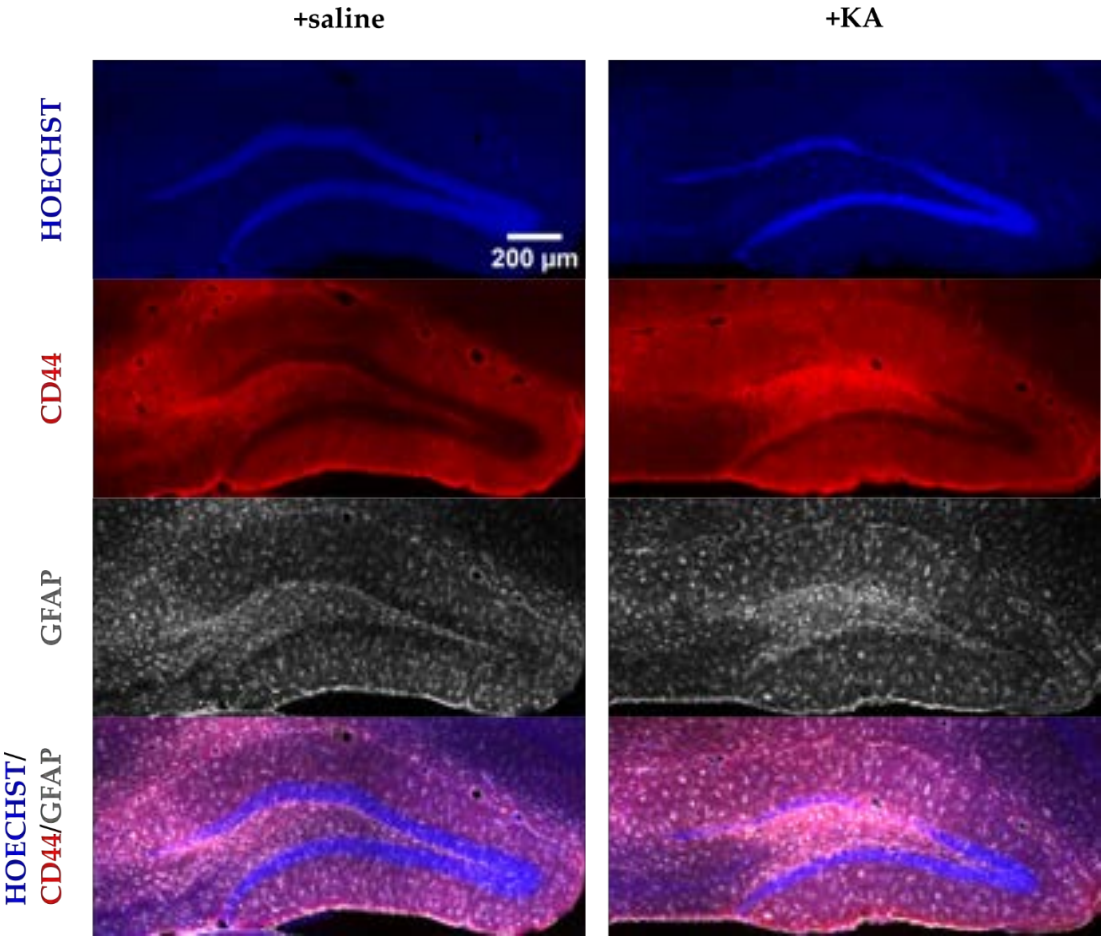

Figure 4.8. Immunofluorescence micrographs of the hippocampus in $CD44^{fl/fl}$ mice following KA-induced SE. Representative images of CD44 (red), GFAP (astrocytes, white), and Hoechst (nuclei, blue) expression in the hippocampus of saline- or KA-injected mice. Scale bar: 200 µm.

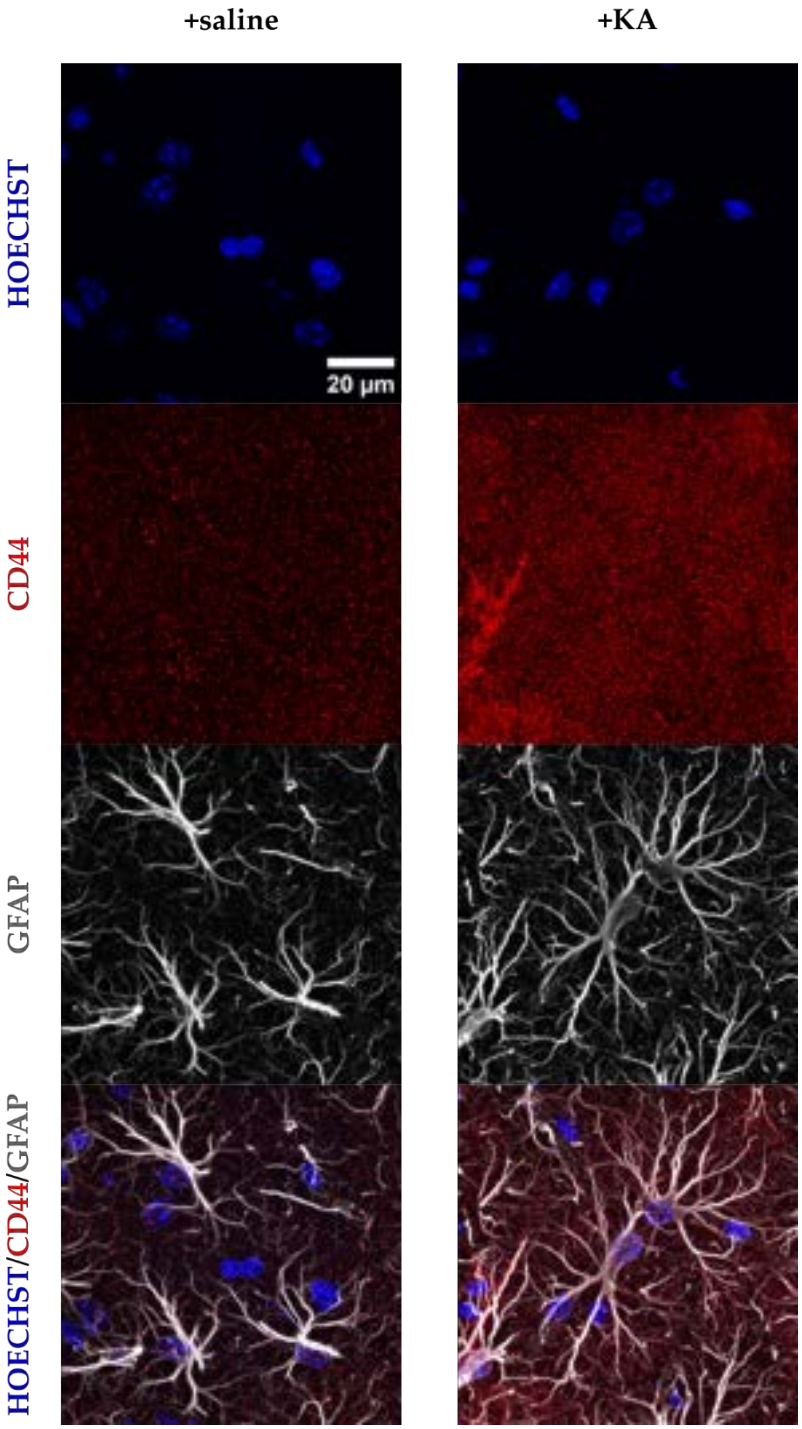

Figure 4.9. Immunofluorescence micrographs of the hippocampal ML in CD44$^{fl/fl}$ mice following KA-induced SE. High-power view of the ML immunostained for CD44 (red), GFAP (astrocytes, white), and Hoechst (nuclei, blue) in saline- or KA-injected mice. Scale bar: 20 µm.

I compared CD44 levels in the hippocampi of control vs. KA-injected mice. The GFAP-positive astrocytic profile area increased significantly four days after KA-induced SE (Figure 4.10-A). Additionally, while CD44 expression remained low in saline-treated controls, a noticeable upregulation of CD44 was observed in

the hippocampal astrocytes of CD44$^{fl/fl}$ mice in the molecular layer of the dentate gyrus (Figure 4.10-B).

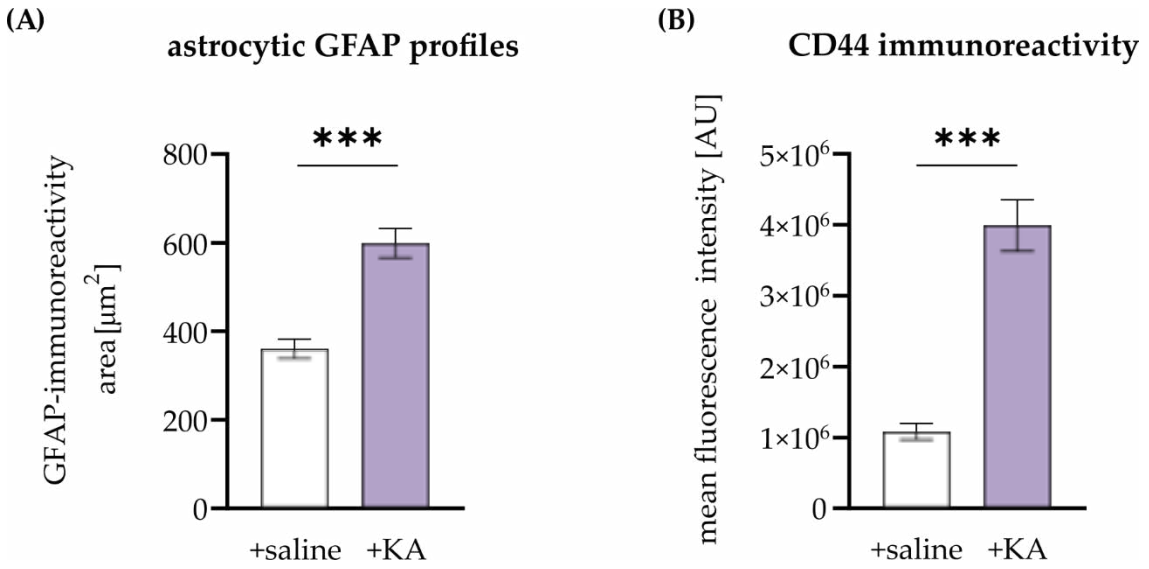

Figure 4.10. Analysis of the GFAP and CD44 expression in hippocampal astrocytes in the ML of CD44$^{fl/fl}$ mice following KA-induced SE. (**A**) Astrocytic GFAP area in CD44$^{fl/fl}$ mice 96 h after saline or KA administration (n=4 independent animals in each group, Student's t-test, ***p<0.001, data presented as mean ± S.E.M.). (**B**) CD44-immunoreactivity in astrocytic GFAP profiles 96 h after saline or KA administration (n=4 independent animals in each group, Student's t-test, ***p<0.001, data presented as mean ± S.E.M.).

These results confirm that intrahippocampal kainate injection results in an increase in CD44 expression and enlargement of the GFAP-positive astrocytic area in the ML of the hippocampal DG.

4.3.2. Seizure pattern analysis in CD44 AsKO mice during KA-induced epileptogenesis

To examine the role of CD44 in epileptogenesis, 2-month-old mice with CD44 deficiency in hippocampal astrocytes (n=12 independent animals per group) received intrahippocampal kainic acid injections and underwent continuous video-EEG monitoring for 4 weeks (Figure 4.11). Same as for AAV surgeries, saline injections served as controls to account for mechanical injury caused by the needle and fluid infusion.

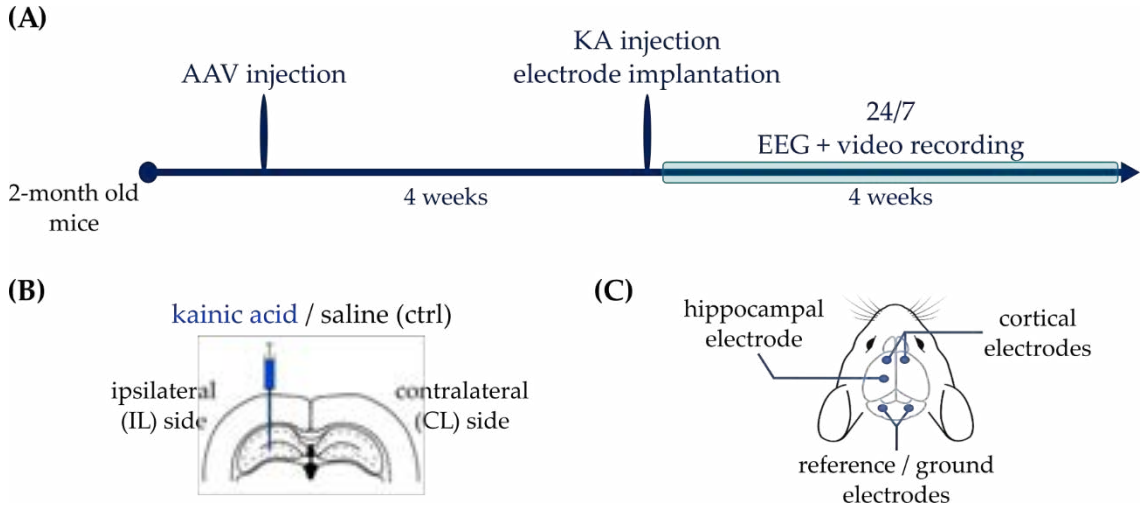

Figure 4.11. KA-induced *status epilepticus* model. (**A**) Schematic representation of the experimental design. (**B**) KA (AsKO cohort) or saline (CTRL cohort) was always injected into the left side (ipsilateral, IL) of the hippocampus. The right side (contralateral, CL) was not treated. (**C**) Location of the electrode placement for EEG monitoring.

Both CTRL+KA and AsKO+KA groups developed seizures during the observation period. When assessing seizures with visible behavioral signs (grades 1–6, as outlined in Analysis of the vEEG recording), there were no significant differences between the groups in the latency to the first spontaneous seizure (Figure 4.12-A), the severity of symptomatic seizures (Figure 4.12-B), and the average seizure duration (Figure 4.12-C),

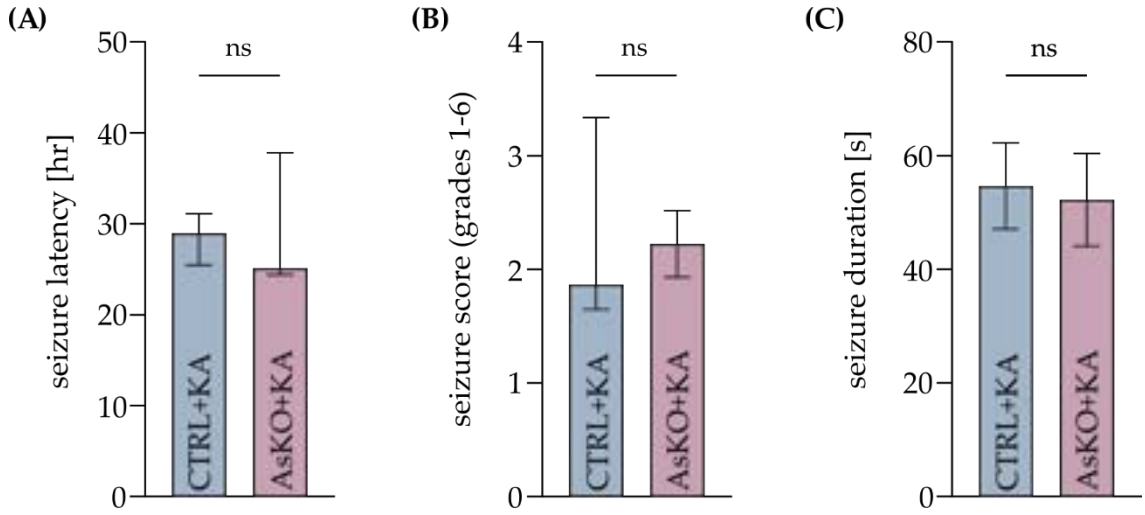

Figure 4.12. Seizure parameters not affected by astrocytic CD44 deletion after KA-induced SE. (**A**) Seizure latency to the first spontaneous seizure was not affected by CD44 knockout (Mann-Whitney test, p=0.217, data presented as median with IQR). (**B**) The average seizure score (for seizures of grades 1–6) was not different in the AsKO compared to the CTRL group (Mann-Whitney test, p=0.699, data presented as median with IQR). (**C**) The mean duration of spontaneous seizures did not differ between the AsKO and CTRL groups (Student's t-test, p=0.832, data presented as mean ± S.E.M.).

However, by the fourth week, CD44-deficient mice (AsKO) exhibited a significantly lower average number of behavioral seizures per day in comparison to controls (Figure 4.13-A). Interestingly, the number of electrographic grade 0 seizures (detected by EEG but without visible behavioral symptoms) was significantly higher in the knockout mice than in the controls (Figure 4.13-B), with 84% of all seizures in the CD44 knockout group being grade 0, compared to 33% in control mice (Figure 4.14).

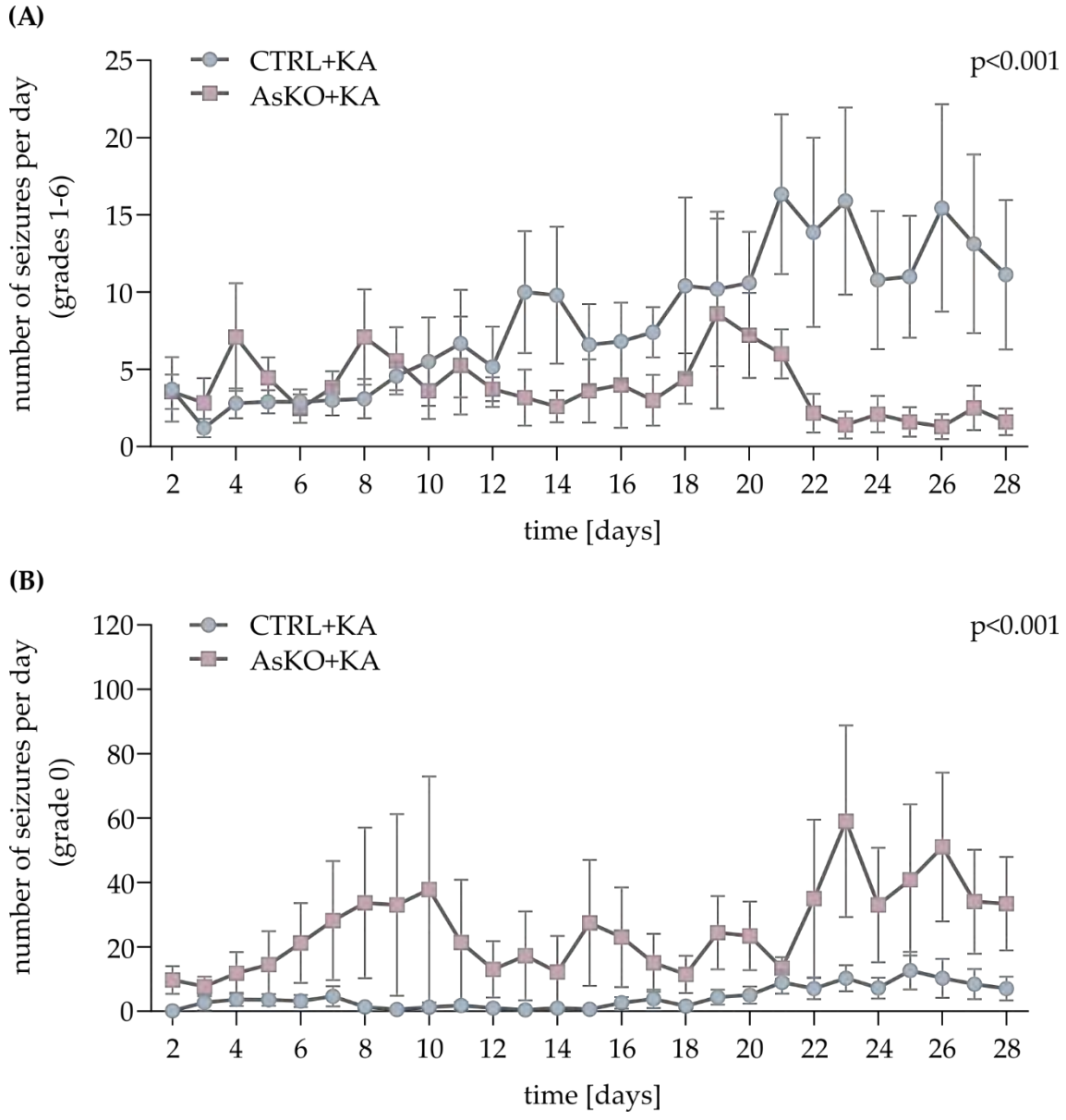

Figure 4.13. Changes in the seizure number between CTRL+KA and AsKO+KA animals during epileptogenesis. (**A**) Knockout animals developed a lower number of behavioral seizures (grades 1–6) per day in comparison to CTRL+KA mice (two-way ANOVA, genotype effect ***p<0.001, data presented as mean ± S.E.M.). (**B**) CD44 knockout mice developed a higher average number of seizures of grade 0 per day than CTRL+KA animals (two-way ANOVA, genotype effect ***p<0.001, data presented as mean ± S.E.M.).

The difference in the total number of seizures, including non-behavioral events, between the AsKO+KA and CTRL+KA groups (Figure 4.14) was primarily due to the significantly higher number of grade 0 seizures in the AsKO+KA group (Figure 4.13-B).

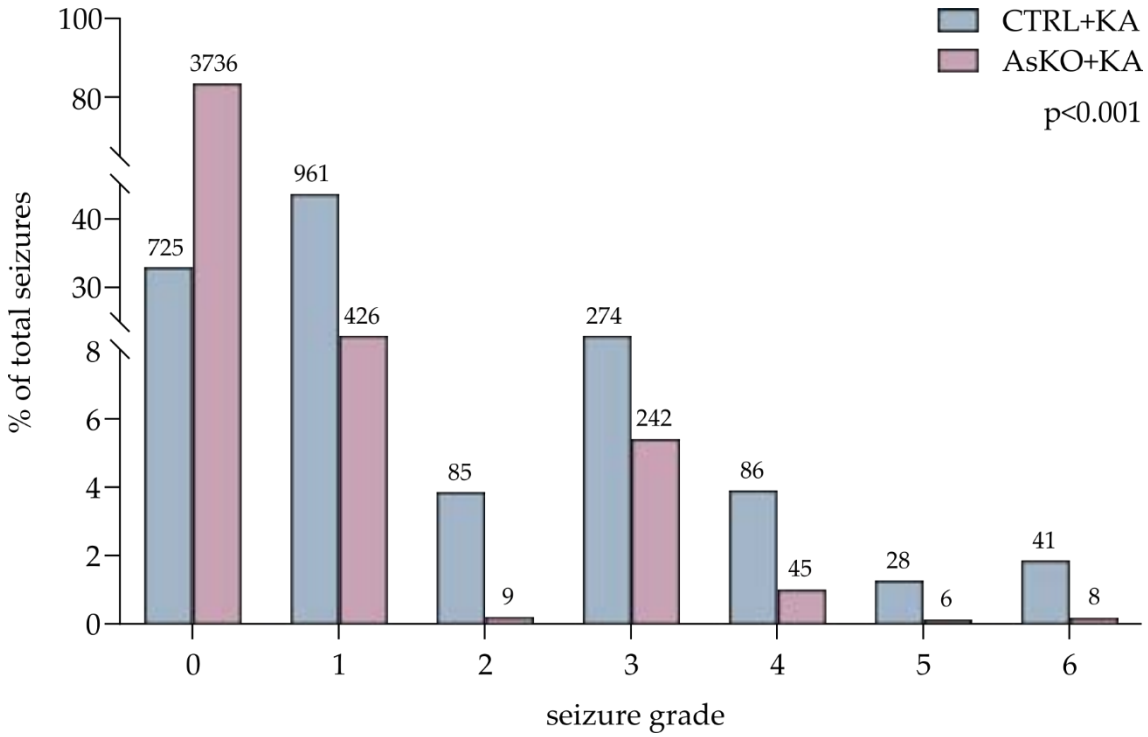

Figure 4.14. The severity of behavioral seizures in CTRL+KA and AsKO+KA animals during epileptogenesis. Data presented as a percentage of each seizure type (grades 0–6) out of all episodes per group. The majority of seizures in AsKO+KA mice were less severe than in the CTRL+KA animals (Fisher's exact test, ***p<0.001).

These findings demonstrate that the absence of CD44 in astrocytes results in a reduced number of behavioral (grade 1-6) seizures and an increased number of EEG-seen-only (grade 0) seizures per day. It also raises the overall percentage of grade 0 episodes at the expense of behavioral seizures.

4.3.3. Reactive astrogliosis in the ML of the dentate gyrus during epileptogenesis in mice with astrocytic CD44 depletion

As previously mentioned, reactive astrogliosis occurs in the mouse hippocampus in response to seizures (reviewed in [82]). Given that CD44 is upregulated in astrocytes following *status epilepticus*, it was crucial to investigate how CD44-deficient astrocytes respond to KA-induced SE. To evaluate reactive astrogliosis, I performed GFAP

immunohistochemical staining on hippocampal sections from CTRL and AsKO mice, 4 weeks after either saline (Figure 4.15) or kainate (Figure 4.16) injection.

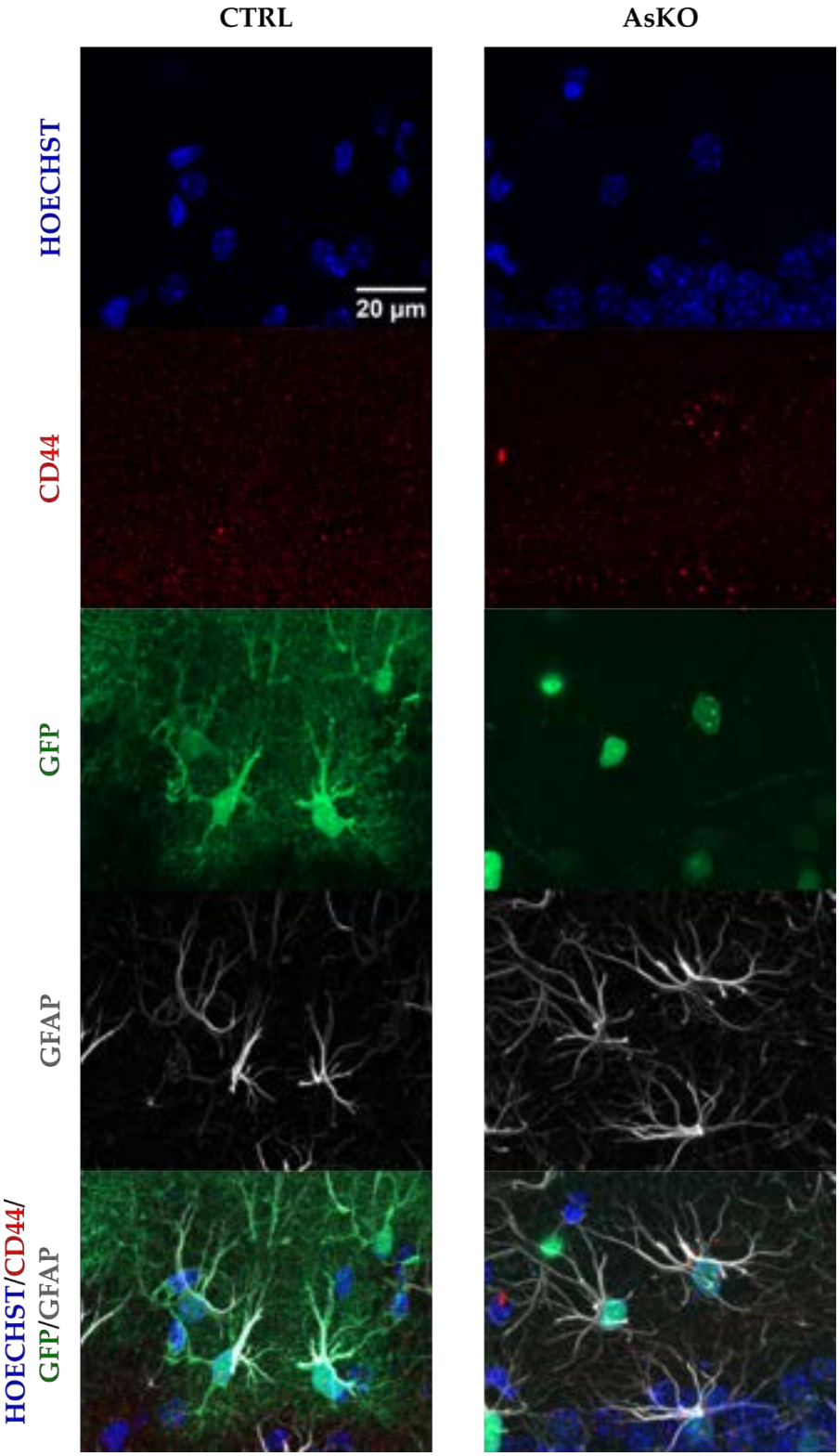

Figure 4.15. Immunofluorescence micrographs of the ML of the DG in CTRL and AsKO mice post-saline injections. Representative images of the GFAP (astrocytes, white), CD44 (red), GFP

(green), and Hoechst (nuclei, blue) expression in the hippocampal ML of the DG in CTRL and AsKO mice 4 weeks post-saline administration. Scale bar: 20 μm.

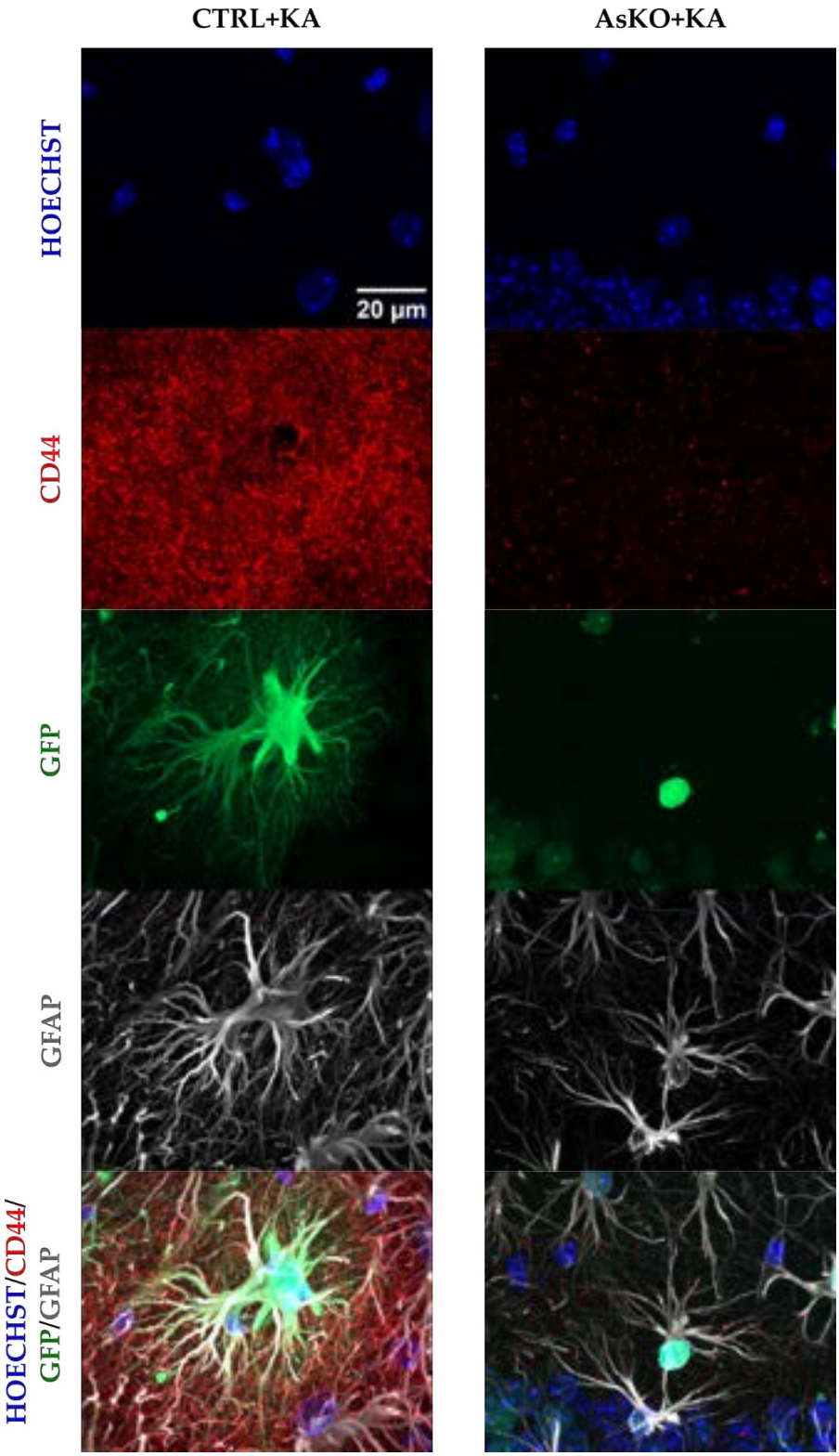

Figure 4.16. Immunofluorescence micrographs of the reactive astrogliosis in the ML of the DG in CTRL+KA and AsKO+KA mice. Representative images of the GFAP (astrocytes, white), CD44 (red), GFP (green), and Hoechst (nuclei, blue) expression in the hippocampal ML of the DG in CTRL and CD44 AsKO mice 4 weeks post-KA administration. Scale bar: 20 μm.

For quantification, I measured the average area of the GFAP immunoreactivity (GFAP-ir) per astrocyte which indicates the level of reactive astrogliosis (Figure 4.17). Results showed that CD44 deletion did not significantly affect GFAP-ir in naïve, saline-treated mice, but seizure-induced astrogliosis was reduced considerably in AsKO+KA animals compared to CTRL+KA mice.

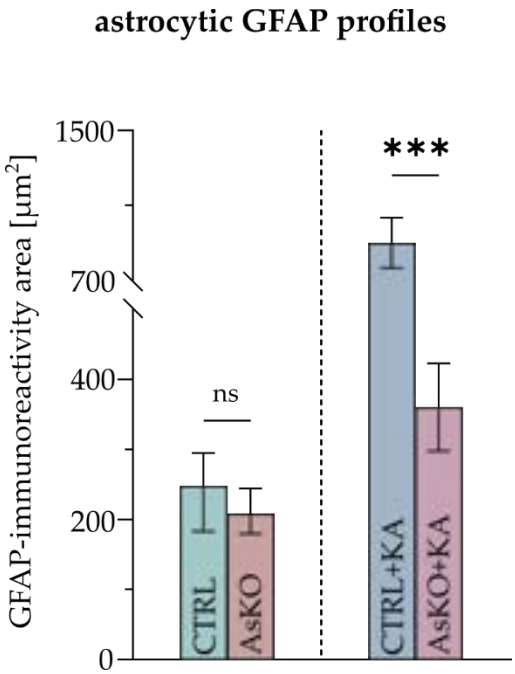

Figure 4.17. Quantitative analysis of astrocytic GFAP profiles in the ML of the DG. GFAP-immunoreactive area (µm²) 4 weeks after administration of saline (Mann-Whitney test, p=0.230, data presented as median with IQR) or KA (Student's t-test, ***p<0.001, data presented as mean ± S.E.M.).

Those results demonstrate that the absence of CD44 in astrocytes results in a decreased size of the GFAP-positive area of astrocytes in the epileptic ML of the DG in the hippocampus.

4.3.4. Astrocytic CD44 expression in the ML of the dentate gyrus after KA administration

In addition to GFAP staining, the CD44 expression in astrocytes was assessed (Figure 4.18) based on the same immunohistochemical staining (Figure 4.15, Figure 4.17). CD44 immunoreactivity (CD44-ir) was significantly lower in AsKO mice compared to CTRL mice after saline (***p<0.001) or KA administration (**p=0.001). In the CTRL+KA group, CD44 upregulation following seizures remained evident and was even more pronounced than at 4 days post-kainate injection (shown in Figure 4.10). However, no

significant increase in CD44-ir was observed in AsKO+KA mice compared to untreated AsKO mice.

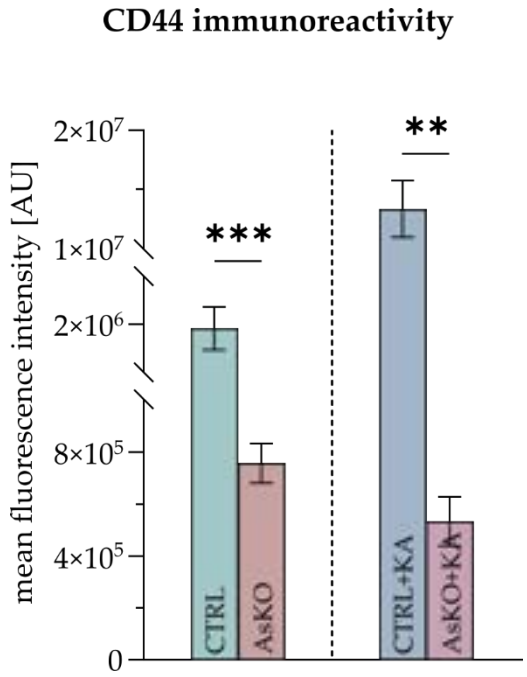

Figure 4.18. Quantitative analysis of CD44 immunoreactivity in GFAP astrocytic profiles in the ML of the DG. CD44 immunoreactivity 4 weeks after administration of saline (***p<0.001) or KA (**p=0.001). Student's t-test with Welch's correction, data presented as mean ± S.E.M.

These findings confirm that astrocyte-specific CD44 deletion lowers CD44 expression in the molecular layer of the hippocampus, which does not increase with the seizure occurrence and during epileptogenesis.

4.3.5. Mossy fiber sprouting and granule cell dispersion in GCL and ML of the dentate gyrus during epileptogenesis

As mossy fiber sprouting is a common histopathological finding in MTLE [197, 198], its analysis in animals with astrocytic CD44 deletion in the hippocampus may shed some light on the seizure pattern changes after KA-induced SA. As previously mentioned, in regular conditions, ZnT3 is mostly accumulated in the hilus but with the progression of mossy fiber sprouting its expression is more spread radiating through the granular cell layer into the molecular layer of the hippocampus. It is also correlated with the granule cell dispersion.

For this thesis, MFS alterations were studied with ZnT3 immunohistochemical staining on hippocampal sections from cohorts of 5 independent CTRL and AsKO mice, 4 weeks after either saline or kainate injection. Figures below present ZnT3 expression in the hippocampus (Figure 4.19), granular cell layer (Figure 4.20), and molecular layer (Figure 4.21) of the dentate gyrus. The GCD quantification was done by examining the irregular distribution of GCs within the GCL based on micrographs of Hoechst immunostaining. For each mouse, the distance from the hilar border to the outer edge of the GCL's upper blade was measured and its first- and third-quarter fragments were used to calculate an average GCL width for both the ipsilateral and contralateral hemispheres.

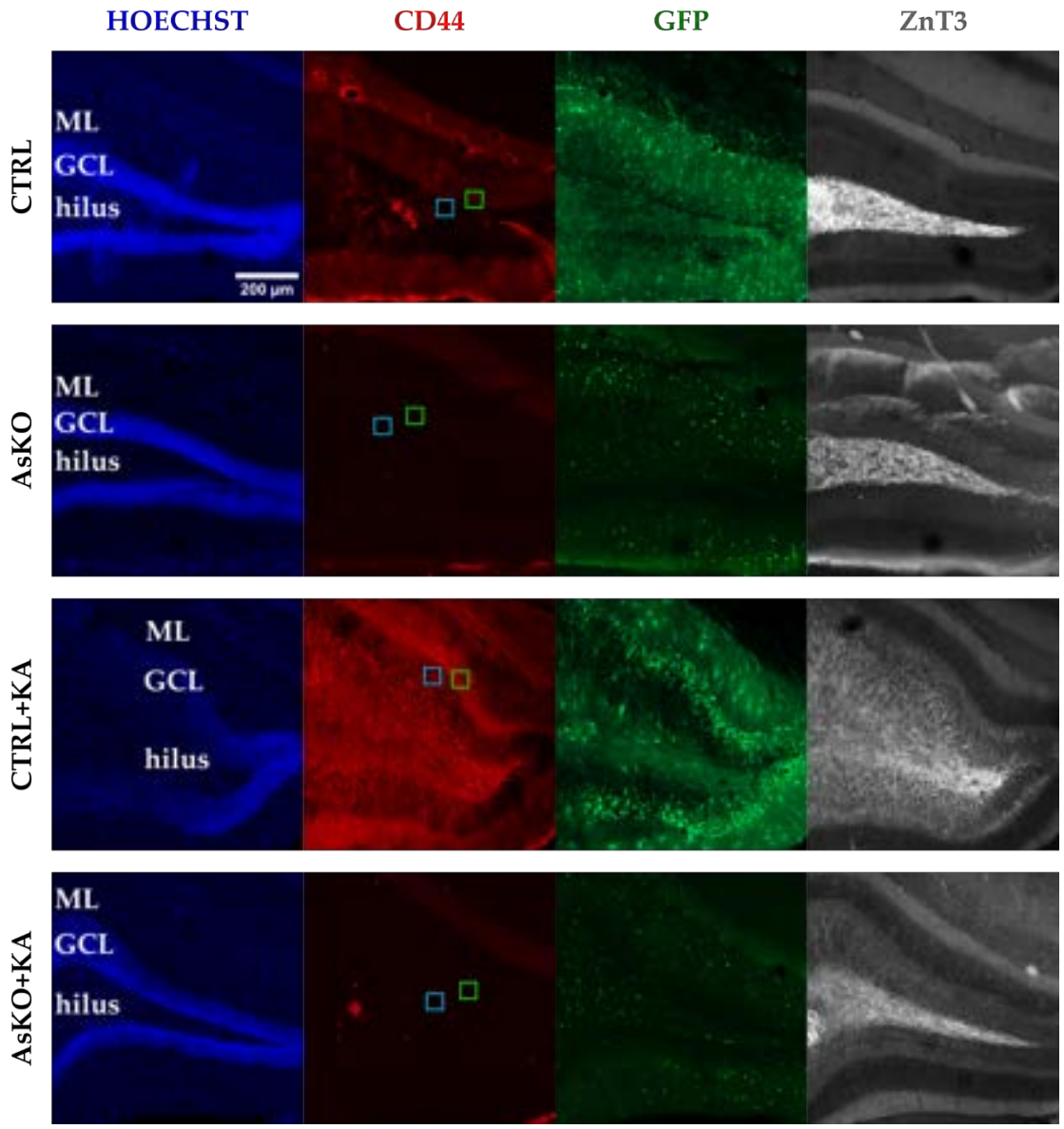

Figure 4.19. Mossy fiber sprouting in the hippocampus of CD44 AsKO mice. Representative images of the ZnT3 (MFS, white), CD44 (red), GFP (green), and Hoechst (nuclei, blue) expression in CTRL

and AsKO mice 4 weeks after saline or KA administration. Squares show the location of the close-up images of the GCL (blue, Figure 4.20) and the ML (green, Figure 4.21). Scale bar: 200 μm.

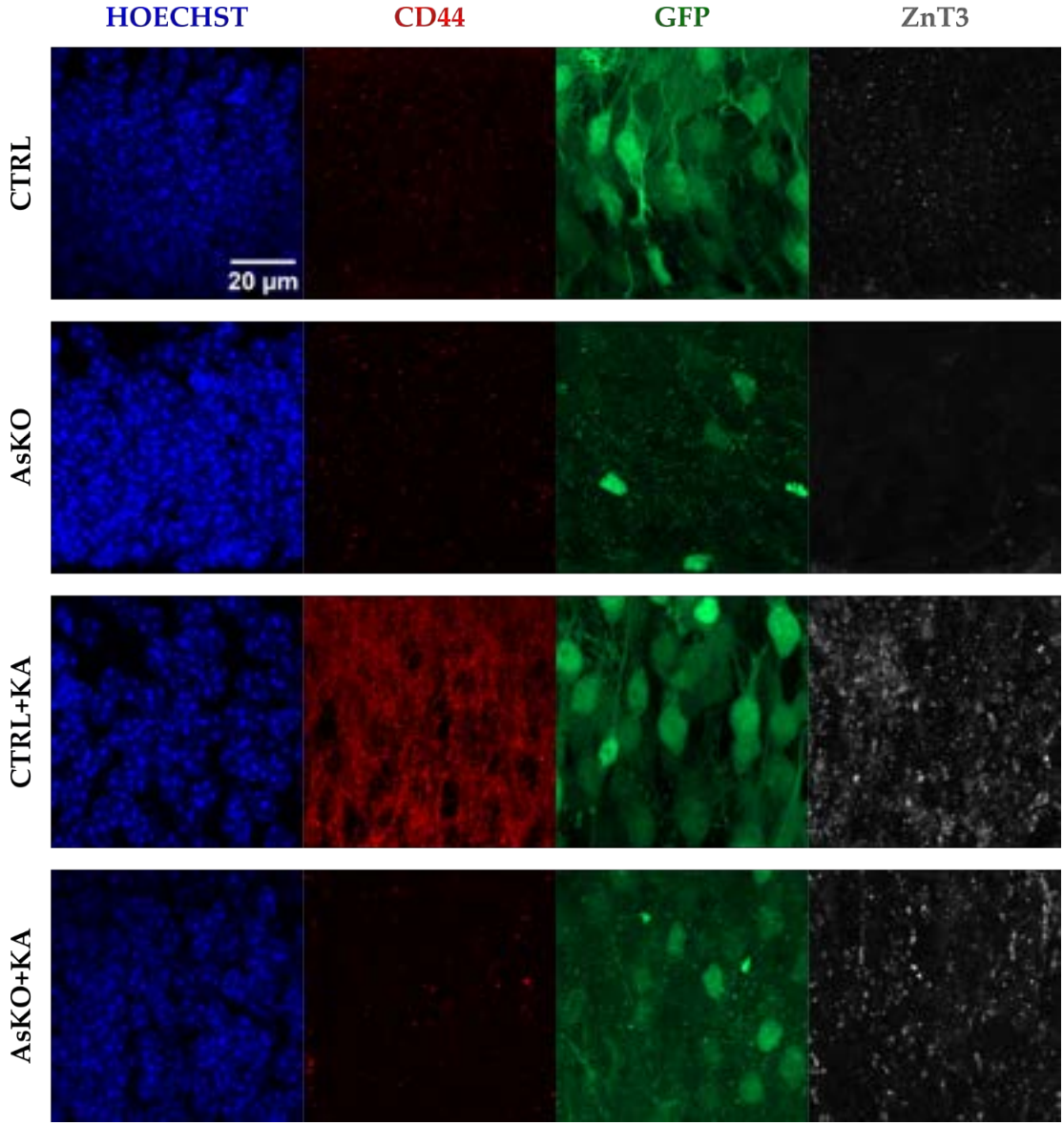

Figure 4.20. Mossy fiber sprouting in the GCL of the DG of CD44 AsKO mice. Representative images of the ZnT3 (MFS, white), CD44 (red), GFP (green), and Hoechst (nuclei, blue) expression in CTRL and AsKO mice 4 weeks after saline or KA administration. Scale bar: 20 μm.

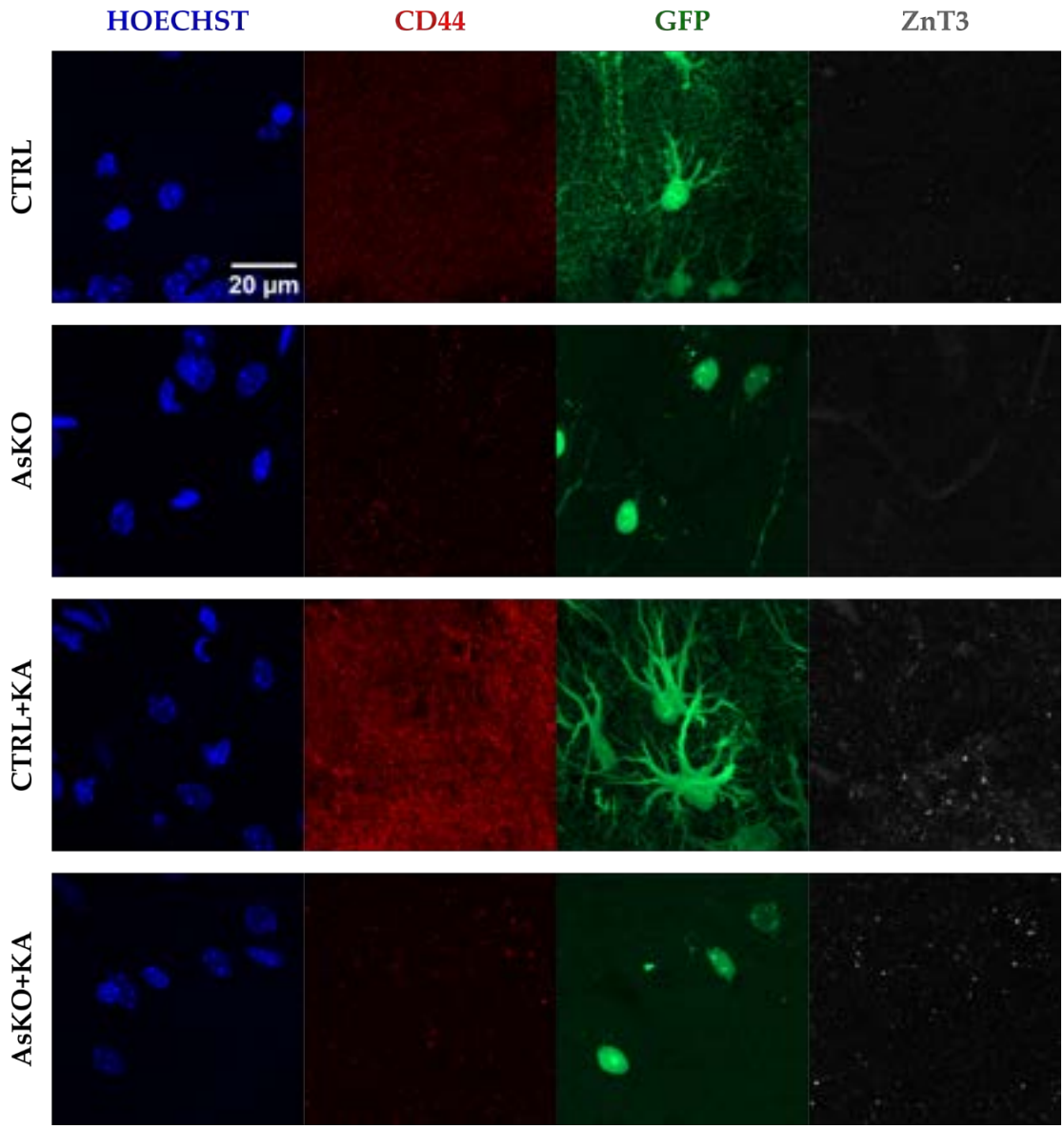

Figure 4.21. Mossy fiber sprouting in the ML of the DG in CD44AsKO mice. Representative images of the ZnT3 (MFS, white), CD44 (red), GFP (green), and Hoechst (nuclei, blue) expression in CTRL and AsKO mice 4 weeks after saline or KA administration. Scale bar: 20 µm.

ImageJ binary transformations of acquired immunofluorescence images allowed for the isolation of ZnT3-immunopositive puncta with a diameter ≥ 0.5 µm (Figure 4.22-A), which represents the minimum size of mossy fiber terminals [189]. Statistical analyses of transformed images showed that the number of ZnT3-immunopositive puncta (**p=0.003) and the MFS percentage (*p=0.021) were both lowered by 52% in the GCL of the ipsilateral side of the hippocampus (KA injection side) in the AsKO+KA animals when compared to CTRL+KA mice. Although not statistically significant, a 25% decrease was noticed in the contralateral side of the hippocampus between the groups (Figure 4.22-B,C).

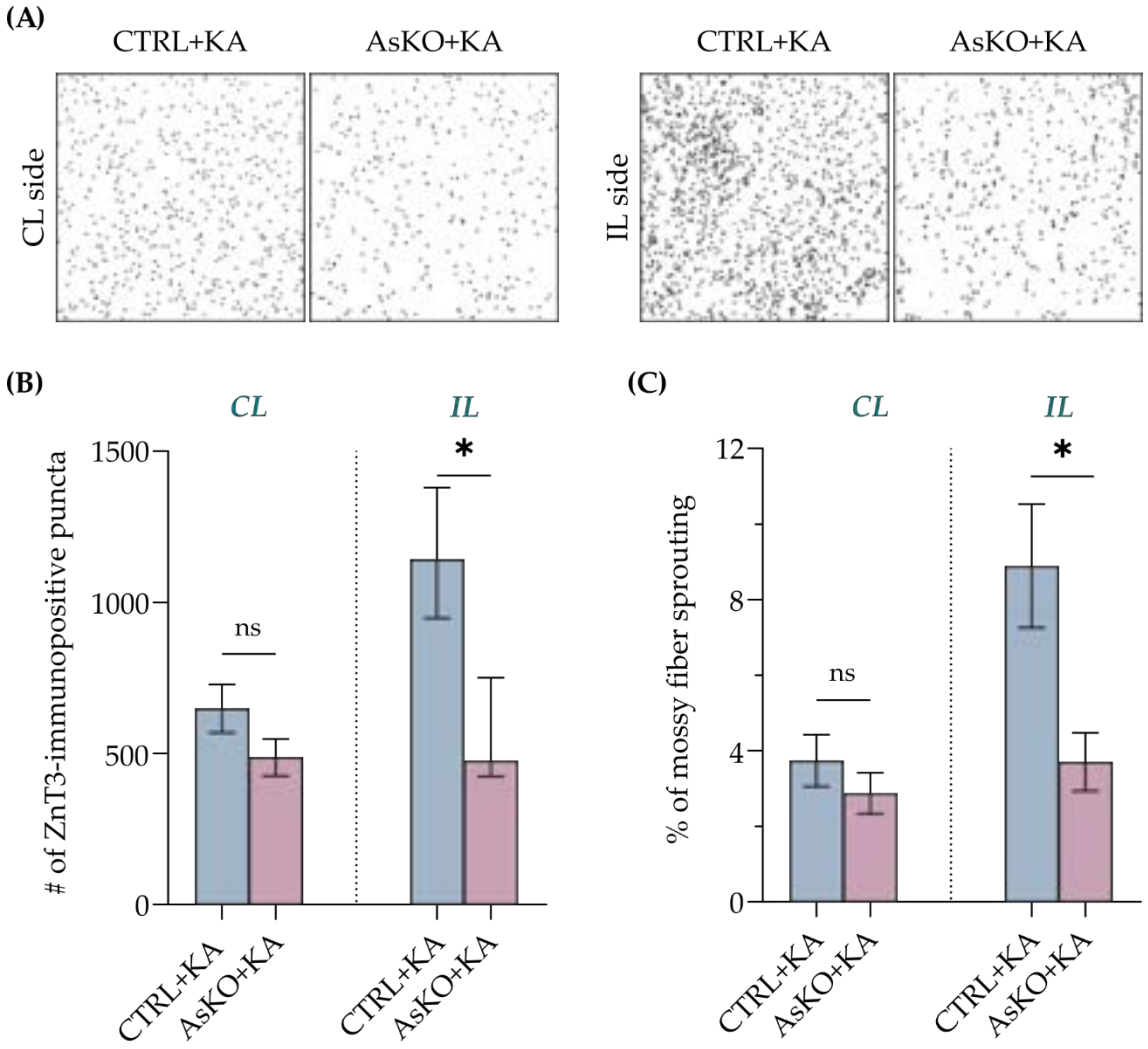

Figure 4.22. Quantitative analysis of ZnT3 immunoreactivity in the GCL of the DG. (**A**) Representative transformations of immunofluorescent micrographs used for particle counting of ZnT3-immunopositive puncta with a diameter ≥ 0.5 μm (the minimum size of a mossy fiber terminal). (**B**) The number of ZnT3-immunopositive puncta in the CL side (Student's t-test, p=0.144, data presented as mean ± S.E.M.) and the IL side (Mann-Whitney test, *p=0.020, data presented as median with IQR) and (**C**) the percentage of MFS in the CL side (Student's t-test, p=0.351, data presented as mean ± S.E.M.) and the IL side (Student's t-test, *p=0.021, data presented as mean ± S.E.M.) in the GCL in CTRL+KA and AsKO+KA groups.

There were no significant dissimilarities in the expression of the ZnT3 in the ML between CD44 knockout and control mice in either the ipsilateral or contralateral side of the hippocampus, with a 17% and 2% decrease respectively (Figure 4.23-B,C).

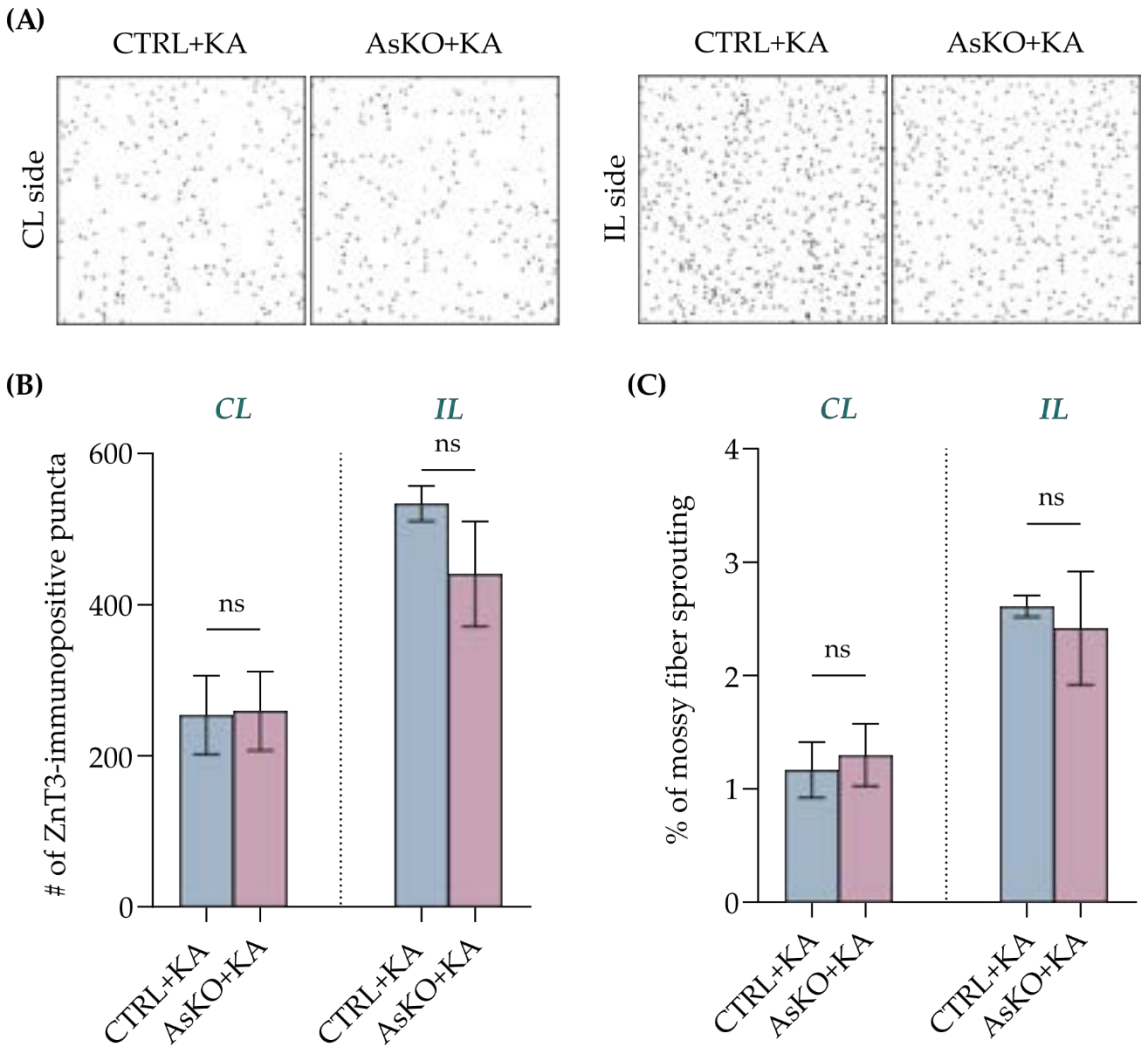

Figure 4.23. Quantitative analysis of ZnT3 immunoreactivity in the ML of the DG. (**A**) Representative transformations of immunofluorescent micrographs used for particle counting of ZnT3-immunopositive puncta with a diameter ≥ 0.5 μm (the minimum size of a mossy fiber terminal). (**B**) The number of ZnT3-immunopositive puncta in the CL side (Student's t-test, p=0.944, data presented as mean ± S.E.M.) and the IL side (Student's t-test, p=0.239, data presented as mean ± S.E.M.) and (**C**) the percentage of MFS in the CL side (Student's t-test, p=0.732, data presented as mean ± S.E.M.) and the IL side (Student's t-test with Welch's correction, p=0.720, data presented as mean ± S.E.M.) in the ML in CTRL+KA and AsKO+KA groups.

In the KA-injected CTRL hippocampi, I noted significant morphological alterations of the GCL (Figure 4.19). The typical dense arrangement of GCs within the GCL was disrupted, where GCs appeared to be more loosely organized, with some even scattered across the hilar region. Statistical analyses of GCL width in both IL and CL hippocampi in CTRL and AsKO mice showed substantial differences in KA-induced GCD between those groups. While the IL side in controls showed a significant 138% increase in the mean GCL width in comparison to the CL side (***$p<0.001$), no such effect was observed in AsKO mice – only a 7% increase (Figure 4.24).

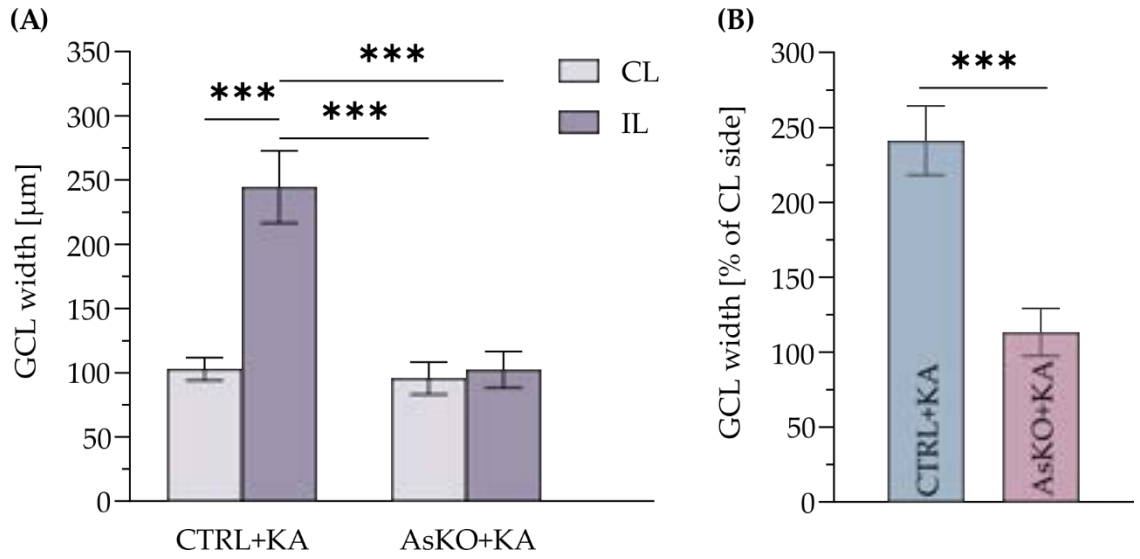

Figure 4.24. The effect of CD44 AsKO on KA-induced GCD in the hippocampal DG. (**A**) The GCL width in the IL compared to the CL side increased in the CTRL animals but did not change in AsKO mice (two-way ANOVA with Tukey's multiple comparison test, ***p<0.001, data presented as mean ± S.E.M.). Statistically non-significant differences were not labeled in the graph to maintain visual clarity. (**B**) GCL width on the IL side normalized to the CL side of the same sample. The KA-induced GCD was significantly higher in controls than in AsKO animals (Student's t-test, ***p<0.001, data presented as mean ± S.E.M.).

Those results show that the absence of CD44 in astrocytes lowers the number of zinc transporter 3 in the granular cell layer of the dentate gyrus and reduces granular cell dispersion during epileptogenesis.

4.3.6. Ultrastructural changes in the molecular layer of the hippocampal dentate gyrus of CD44 AsKO mice

To determine whether changes in seizure severity in CD44 astrocytic knockout mice are linked to structural alterations in the astrocyte-neuron relationship, I utilized electron microscopy to examine synapses and surrounding astrocytes at the ultrastructural level. SBEM was used to reconstruct synaptic connections and adjacent astrocytic terminal processes in 3D from the molecular layer of the dentate gyrus. Tissue samples of 6 µm × 6 µm × 6 µm were analyzed per animal using an unbiased sampling approach [194]. A volumetric analysis of postsynaptic densities was conducted to represent the postsynaptic regions of the synapse. Following kainate-induced seizures, I reconstructed 192 synapses with nearby astrocyte processes from the control group (CTRL+KA) and 472 synapses from CD44-deficient mice (AsKO+KA). The distances between PSDs and adjacent astrocytic processes in both groups were measured and, based

on the method of Ostroff et al. [195], synapses with astrocyte contacts were defined as those with a PSD-leaflet distance of ≤20 nm. Results show a lower proportion of such contacts in AsKO+KA mice compared to the CTRL+KA group (Figure 4.25-B).

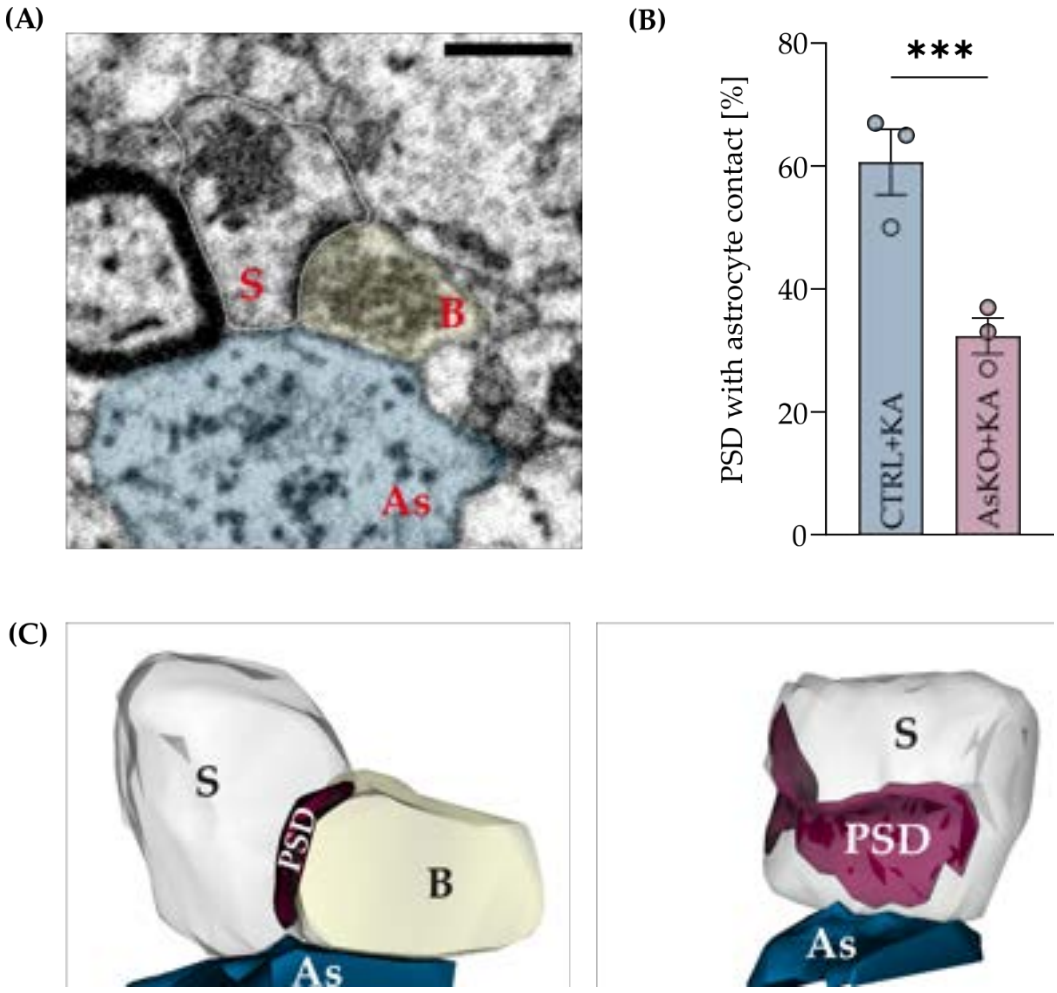

Figure 4.25. Astrocyte–synapse interaction in the ML of the DG in CD44 AsKO mice after KA-induced SE. (**A**) Representative image of a synaptic structure from SBEM. Astrocytic leaflet (A, blue) contacting presynaptic bouton (B, yellow) and postsynaptic dendritic spine (S, grey contour). Scale bar: 500 nm. (**B**) The proportion of synaptic clefts with astrocyte contacts. Displayed as a percentage of PSDs with astrocytic leaflets in a ≤20 nm proximity (Fisher's exact test, ***p<0.001, data presented as mean ± S.E.M.). (**C**) Example of a 3D reconstruction of the tripartite synapse structure with PSD (left panel) and the PSD surface in the same synapse (right panel).

Since previous studies have shown significant spine loss in the dendrites of DG granule cells following kainate-induced seizures [56], I also examined dendritic spine density in mice after saline (CTRL and AsKO) or kainate (CTRL+KA and AsKO+KA) injections. Dendritic spine density in the dentate gyrus' ML significantly decreased after seizures in controls (CTRL vs. CTRL+KA, ***p<0.001) but not in AsKO mice (Figure 4.26-C). Moreover, KA-treated AsKO animals had lower spine loss than those with

a normal CD44 expression (AsKO+KA vs. CTRL+KA, *p=0.01) which was slightly reduced compared to controls (AsKO+KA vs. CTRL, p=0.05).

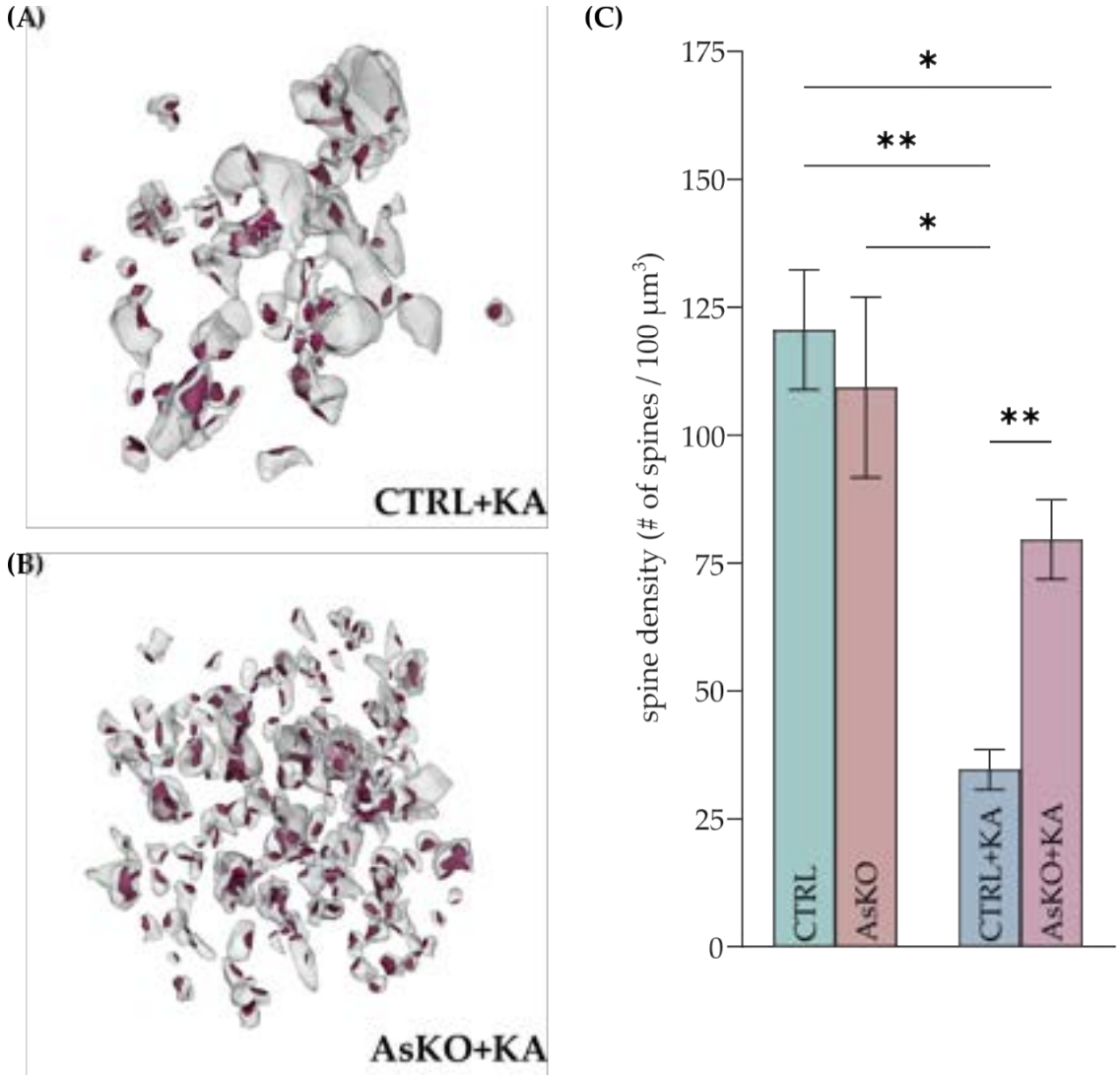

Figure 4.26. Spine loss in the ML of DG in CD44 AsKO mice after KA-induced SE. (**A,B**) Examples of 3D reconstructions of spines (white) with their PSD (red) from CTRL+KA and AsKO+KA mice (brick size: 6 µm × 6 µm × 6 µm). (**C**) Decreased spine density in CTRL mice following KA treatment. In CD44 AsKO animals the KA-induced reduction in spine density is diminished (Welch's ANOVA, ***p<0.001, data presented as mean ± S.E.M.). Statistically non-significant differences were not labeled in the graph to maintain visual clarity.

Aside from the differences seen on the spine level, additional analyses were done to determine possible changes in PSD. The average volume and surface area of PSD were significantly smaller (***p<0.001) in AsKO+KA mice compared to CTRL+KA animals (Figure 4.27).

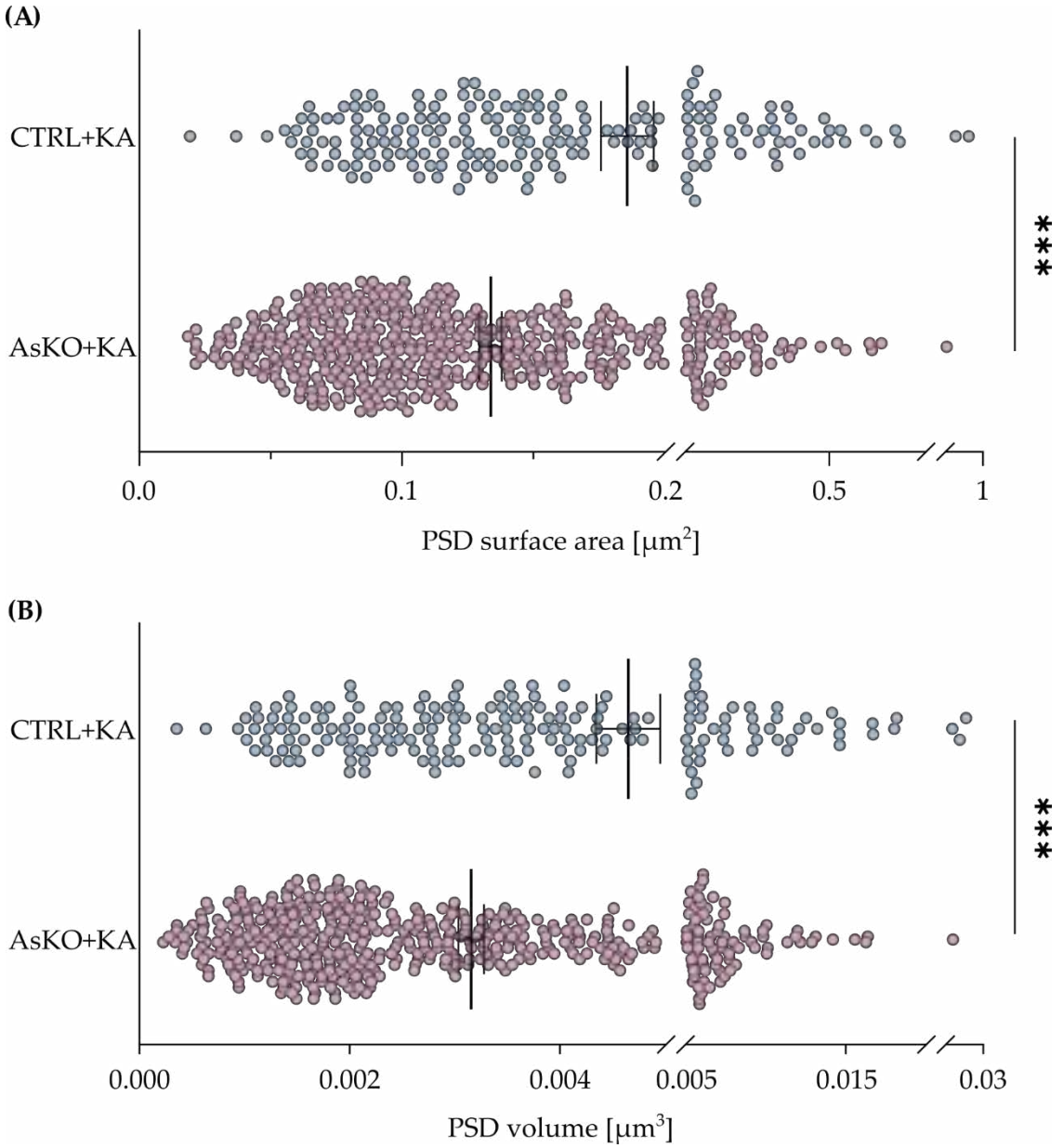

Figure 4.27. PSD area and volume decreased in the ML of DG in AsKO+KA mice after KA-induced SE. Both PSD surface area (**A**) and volume (**B**) are decreased in the AsKO+KA group following KA treatment (Student's t-test with Welch's correction, ***p<0.001, data presented as mean ± S.E.M.).

These findings demonstrate that the absence of CD44 in astrocytes results in decreased astrocyte-synapse contact, increased dendritic spine density, and reduced PSD size in the epileptic ML of the DG in the hippocampus.

5. DISCUSSION

5.1. Generation of a transgenic mouse line with astrocyte-specific conditional CD44 knockout allowing for temporal control of gene deletion

A properly functioning transgenic experimental animal model is crucial for any *in vivo* research. In the generation of any transgenic line, one needs to take into consideration not only the basic characteristics of the cells that are targeted (promoter, a receptor presence) but also the type of the system used and its limitations, e.g., the Cre-loxP system (inducible, non-inducible) or AAV vector transduction (serotype tropism).

Previous research showed, that CD44 loss during the late stages of development can have different implications than its absence from the beginning of the development process. The early elimination of CD44 during embryogenesis could potentially trigger the activation of a gene or set of genes that may compensate for the absence of CD44 in certain situations [101]. To study the role of CD44 in pathological conditions acquired during a lifetime, it is important to use models allowing for site- and time-specific gene modification.

5.1.1. Generation of tamoxifen-inducible total astrocyte-specific CD44 knockout mice using the Cre-loxP system

The use of the TAM-inducible Cre-loxP system to generate cell-specific CD44 depletion holds a lot of advantages. In this project, the induction of CD44 knockout by intraperitoneal TAM injections was intended to create a total depletion of CD44 in astrocytes in the brain allowing for a broad spectrum of possible analyses in different brain regions. It would also cut down the need for additional intracranial surgeries (e.g., intracranial injections of recombination agents) reducing the mortality risk coming with such procedures and additional mechanical brain tissue damage following needle insertion.

Nevertheless, this model also has its alarming yet not commonly known downsides. Several important caveats have been identified when using the Cre-lox system, including Cre-induced toxicity, mosaicism or inconsistent recombination activity, metabolic phenotypes resulting from illegitimate recombination, genetic background effects, and unintended Cre expression in undesirable cell types [199-202]. One particularly overlooked but significant issue is unintended germline recombination. If Cre recombinase activity occurs in germline cells, it may lead to excision of the floxed allele in all cells, rather than the intended cell-type or region-specific pattern. Many published studies involving conditional gene-knockout experiments lack sufficient details to assess whether authors were aware of potential issues related to unpredicted recombination when passing on Cre recombinase and floxed alleles through the germline [203]. Recognizing the potential for germline recombination in Cre driver lines, particularly those designed for nervous system specificity, seems to be critical for accurate genotyping and proper interpretation of experimental data. Moreover, understanding how parental sex influences germline recombination, and comparing this across related Cre driver lines, could help in the optimization of breeding strategies, saving both resources and time. Unfortunately, detailed information on affected Cre driver lines remains limited with only a few sporadic reports, and a comprehensive meta-analysis has yet to be conducted.

Researchers new to these techniques may be unaware of the germline problem, as it is rarely acknowledged by more experienced investigators. In this study, the germline issue was not initially considered and no additional confirmatory genotyping was performed at the time of the brain tissue extraction, which might have been the main reason for the insufficient results of the CD44 knockout in astrocytes. Both transgenic lines used to create a double transgenic conditional knockout were acquired externally with provided documentation and full genotyping information. $CD44^{fl/fl}$ line demonstrated the ability to provide a CD44 deletion phenotype when used with the non-inducible Cre-loxP system in the study of the epidermis [175]. Unfortunately, GFAP-Cre^{ERT2}x$CD44^{fl/fl}$ animals (the cross-breeding of $CD44^{fl/fl}$ and GFAP-Cre^{ERT2} lines) did not show differences in the CD44 expression in the hippocampus, neither in the immunohistochemical nor Western blot analysis, therefore there was a need to alternate for a different gene deletion method.

5.1.2. Astrocyte-specific CD44 depletion in the hippocampi of CD44$^{fl/fl}$ mice by the AAV5-mediated expression of Cre recombinase

The lack of CD44 depletion phenotype in GFAP-Cre^{ERT2}xCD44$^{fl/fl}$ animals was the primary reason for searching for another method of CD44 deletion in astrocytes. Alternatives to genetic strategies for achieving spatially and temporally controlled recombination include the introduction of Cre recombinase into floxed target lines or the use of viral vectors to deliver recombinase-dependent expression cassettes to Cre driver lines. This approach is broadly used and effectively avoids the risk of germline recombination present in the TAM-dependent Cre-loxP system. However, it has certain disadvantages. The most significant drawback is the variability in recombination efficiency and targeted brain regions between animals, which is often due to differences in the site of the viral vector administration. Additionally, AAV vectors, commonly used in the nervous system, have a limited capacity, restricting their ability to achieve cell-type specificity.

In this study, GFAP-mediated Cre recombinase was introduced into CD44$^{fl/fl}$ animals. This was opted as the best option, as both the CD44$^{fl/fl}$ line was already accessible in the laboratory and the eGFP-bound Cre recombinase under the control of the astrocyte-specific GFAP promoter (AAV5.*gfa*ABC1D::eGFP-Cre) was commercially available. Before starting the *in vivo* experiments, AAV5.*gfa*ABC1D::eGFP-Cre was tested *ex vivo*. Astrocytic cells were isolated from CD44$^{fl/fl}$ mice and immunohistochemically stained for the presence of CD44 protein. The results showed a decreased expression of CD44 in astrocytic cell cultures of CD44$^{fl/fl}$ animals after AAV5.*gfa*ABC1D::eGFP-Cre transduction (experiment run by Agnieszka Łabanowska, not shown).

The next step was to demonstrate the efficiency of the AAV5.*gfa*ABC1D::eGFP-Cre-mediated CD44 knockout *in vivo*. Recent reports have highlighted that the non-specific effects of Cre recombinase in the brain primarily affect neurons rather than astrocytes [204]. The potentially harmful effects of AAV-mediated Cre expression in these studies point to issues in the DNA repair machinery, leading to a significant reduction in neuronal populations. To better understand this phenomenon, including wild-type mice with a Cre injection as a control could provide valuable insights. However, since this study focuses on astrocytic CD44 and there was no extensive cell

death observed, the experiments did not include WT controls injected with AAV5.*gfa*ABC1D::eGFP-Cre to minimize the number of animals sacrificed. Nevertheless, to exclude the influence of the used AAV vector itself on the expression degree, a control AAV5.*gfa*ABC1D::eGFP vector was used on $CD44^{fl/fl}$ animals. A study by Orlinski et al. [205] showed that AAV viruses expressing eGFP under the control of the *gfa*ABC1D promoter can induce astrocyte reactivity depending on the viral titer. At lower titers (10^{10} genome copies per injection), eGFP-positive cells maintained normal astrocytic morphology with low GFAP levels, whereas higher titers (3×10^{10} genome copies) resulted in hypertrophic, reactive astrocytes. This experiment used low-titer injections (control: 4×10^{9} and Cre: 2.2×10^{9} genome copies per injection) that do not trigger astrocytosis.

Interestingly, following later KA treatment, GFP expression was also detected in the DG granule neurons, suggesting that AAV5 may also infect these cells. More surprisingly, KA appeared to influence neuronal gene expression, activating GFAP promoter-driven expression in granule neurons. This observation aligns with earlier findings where GFAP-driven transgenes were expressed in hippocampal neurons [206]. One possible explanation for this could be increased neurogenesis in the DG and the survival of new granule neurons. Seizure activity has been shown to transiently boost cell proliferation in the DG during the first two weeks post-SE [207]. New neurons in the DG emerge from radial neural stem cells, which, like astrocytes, express GFAP [208, 209] and can survive for at least six months [210]. Although the involvement of neurons in this study's results cannot be entirely ruled out, it is likely that the observed effects stem primarily from the CD44 knockout in astrocytes rather than neurons. This is supported by the low expression of CD44 in neurons in the adult brain and the fact that KA-induced CD44 expression occurs in astrocytes but not neurons.

Immunohistochemical and biochemical analyses of CTRL and AsKO animals both showed a significant reduction of the CD44 expression in the whole infected hippocampal area after AAV5.*gfa*ABC1D::eGFP-Cre injection into the molecular layer of the dentate gyrus. Those results, together with a high transduction efficiency, confirmed the expression of Cre recombinase and CD44 deletion in astrocytes in the used model.

5.2. The function of astrocytic CD44 protein in the seizure development during epileptogenesis

5.2.1. CD44 expression in the epileptic brain

CD44 has been predominantly identified in astrocytes in both rodent and human brains, where it plays a crucial role in regulating astrocyte morphology [115, 211]. Increased CD44 immunoreactivity has been observed in astrocytic processes in human patients with tuberous sclerosis and Alzheimer's disease, and in a mouse model of Alexander disease, all associated with seizures [130, 211, 212]. CD44 has also been identified in genome-wide transcriptome analyses as a therapeutic target for epilepsy in both rats and humans [131, 139]. These findings highlight the significance of CD44 in seizure-related conditions and its potential as a treatment target.

CD44 expression increases following brain injury [213], but findings regarding its role in epilepsy models have been inconsistent. In mice, CD44 was significantly upregulated in the molecular layer of the dentate gyrus three days after pilocarpine-induced *status epilepticus*, though its level declined over the next month [128]. Similarly, CD44 was one of the most highly induced proteins in the brain during kainate-induced epileptogenesis in a proteomic analysis [142]. Contrasting these observations, studies using hippocampal organotypic cultures showed reduced CD44 expression in the molecular layer following KA treatment [129]. In our temporal lobe epilepsy model, CD44 was overexpressed in hippocampal astrocytes, and this elevated expression persisted for the next four weeks. The discrepancy between studies may be attributed to the use of different epilepsy models, with our *in vivo* approach potentially capturing a more complex physiological response compared to the controlled environment of cell culture experiments.

5.2.2. The consequences of the astrocytic CD44 deletion in the hippocampus on epileptogenesis

In this study, CD44 astrocyte-specific knockout mice exhibited fewer spontaneous behavioral seizures following kainate-induced *status epilepticus* (TLE model) when

compared with control animals. Most seizures in CD44 AsKO mice were only electrographic, non-convulsant grade 0 episodes, meaning they were detectable via EEG but showed no visible behavioral symptoms. On the other hand, CD44 depletion does not seem to have any effect on the latency and duration of episodes, as well as the seizure score of behaviorally expressed episodes.

Temporal lobe epilepsy is associated with significant abnormal synaptic plasticity in the molecular layer of the dentate gyrus [214]. Recent research has shown that astrocytic deletion of Ezrin, a protein that binds to CD44, results in smaller astrocyte territories and decreased astrocytic coverage of excitatory synapses. This reduction leads to lower levels of synaptic glutamate and elevated diffusion of extrasynaptic glutamate and has notable effects on contextual fear memory [215]. Given that CD44's C-terminal cytoplasmic domain interacts with Ezrin, the reduced severity of seizures in CD44 AsKO mice could be linked to changes in glutamate uptake and diffusion. Supporting this hypothesis, increased CD44 expression in astrocytes has been associated with a reduction in the glutamate transporter-1 (GLT-1) on the cell membrane and a decrease in glutamate transporter current [211]. This suggests that astrocytes with elevated CD44 expression following KA-induced *status epilepticus* may be less efficient at buffering glutamate compared to non-reactive astrocytes.

Epilepsy arises from a disproportion between neuronal excitation and inhibition. Two key mechanisms that help reduce epilepsy occurrence are the conversion of polyamines into GABA and the subsequent release of GABA by astroglia [216-218]. While there is no straight evidence linking CD44 function to GABA release, the positive effect observed from CD44 deficit on seizure development could be associated with changes in the interaction between CD44 or CD44-dependent signaling pathways and astrocytic GABA release, or with mechanisms that control polyamine conversion to GABA in astrocytic cells. Additionally, the astrocytic knockout of CD44 may influence not only excitatory synapses but also the inhibitory ones formed by GABAergic neurons in the molecular layer of the hippocampus. This alteration in the balance between excitatory and inhibitory signaling could further explain the effect of CD44 depletion on seizure severity reduction.

The findings of this work confirm that CD44 depletion in astrocytes impairs the development of behavioral seizures, though the molecular mechanisms behind CD44's role in the seizure pattern change remain unclear.

5.3. The role of astrocytic CD44 protein on the typical structural changes in the hippocampus during temporal lobe epilepsy

5.3.1. Reactive astrogliosis in epileptic CD44 AsKO animals

Reactive astrocytes are vital in the pathophysiology of the central nervous system. Reactive astrogliosis, the activation of astroglia following brain injury such as epilepsy, is linked to changes in the astrocyte morphology. Previous research conducted in the Laboratory of Molecular and Systemic Neuromorphology demonstrated that CD44 regulates the shape of astrocytes in primary astrocyte cultures [115]. This study demonstrates the reduction in GFAP-ir profiles in CD44 AsKO mice during seizures suggesting that increased CD44 expression supports astrogliosis progression. These findings align with earlier studies presenting phenotypic conversion from typical protoplasmic to hypertrophic astrocytes in Alexander disease being associated with CD44 acquisition by normally CD44-negative astroglia [211]. This implies that CD44 may play a role in astrogliosis by influencing astrocyte morphology. Additionally, there is evidence that reactive astrogliosis itself can trigger seizures. Genetically or virally induced astrogliosis is sufficient to cause epileptic seizures in mice without other central nervous system pathologies [205, 219]. Therefore, CD44 might also influence seizure severity by promoting astrogliosis.

5.3.2. Mossy fiber sprouting and granule cell dispersion in epileptic CD44 AsKO animals

TLE is the most prevalent form of drug-resistant epilepsy. In the majority of TLE patients, histopathological analysis reveals unilateral hippocampal sclerosis characterized by selective neuronal loss and astrogliosis, predominantly in the CA1, CA3, and hilus regions of the hippocampus [220]. During TLE, granule cells undergo substantial axonal restructuring – the axons of these cells (mossy fibers) lose their target cells due to the death

of hilar mossy cells and neurons in CA3. Consequently, these fibers grow back through the GCL into the ML to replace the lost connections on the dendrites of the granule cells, the process known as mossy fiber sprouting [215, 216]. The typical compact structure of the GCL becomes disrupted, resulting in granule cell dispersion. All those architectural changes are linked to *status epilepticus* and the progression of epilepsy [221]. This study shows that astrocyte-specific deletion of CD44 influences mossy fiber sprouting and granule cell dispersion in mice with KA-induced SE.

The decrease in the expected mossy fiber sprouting is seen in the ipsilateral GCL of the epileptic CD44 AsKO mice but not in the ML or both of those structures in the contralateral dentate gyrus of those animals. Bouilleret et al. reported observing minimal MFS in the contralateral hippocampus 30 days following kainate injection in just one out of four animals. After 120 days, increased sprouting was detected in two animals, but it remained less prominent than the injected side [165]. Here, we assessed sprouting 28 days post-KA injection, which could potentially account for the differences in our findings. Another important variation in how MFS is recognized in hippocampal slices is the used model of TLE. The comparison of the p35 mutant model [222, 223] with the unilateral KA-injection model of TLE demonstrated immunofluorescent differences in the distribution of synaptoporin (SPO) labeling mossy fiber synapses across GCL and inner ML. In the p35 model, SPO-positive fibers extended through the mildly dispersed GCL toward the inner ML. In the hippocampus injected with kainate, SPO-positive fibers extensively sprouted extending into the ML through the significantly dispersed GCL. The SPO-ir in the GCL of the unilateral KA injection model was higher than in p35 knockout animals [224]. The GCD and MFS, seen in CD44 AsKO after the KA administration, show similar patterns as the kainate model in the study of Volz et. al. The high degree of GCL dispersion, together with the tissue examination time after KA injection, may serve as an explanation for the mossy fiber sprouting substantial difference only in the GCL of CD44 AsKO mice compared to controls.

The results of this study show that, in contrast to control animals, CD44 AsKO mice do not experience a robust GCD of their ipsilateral GCL. Zhang et al. demonstrated that the upregulation of CD44 is linked to the activation of the mechanistic target of rapamycin (mTOR) signaling pathway in neurons [225]. In the CNS, mTOR is found in neurons,

astrocytes, microglia, and brain endothelial cells. Under normal physiological conditions, the expression of mTOR within CNS cells, including astrocytes, is generally maintained at relatively low levels [226, 227]. Various factors, such as amino acids, hormones, mitogens, insulin, growth factors, and metabolic activity, regulate mTOR activity. However, its expression can significantly increase in response to CNS injury. The hyperactivation of one of the mTOR's multiprotein complexes, mTOR complex 1 (mTORC1), is believed to play a crucial role in mediating GCD in the kainic acid-induced model of TLE, contributing to the onset of spontaneous recurrent seizures [228, 229]. Inhibiting mTORC1 with rapamycin or narigin results in GCD suppression in the mouse model of TLE [230, 231]. As mTORC1 is a downstream component of the CD44-regulated phosphoinositide 3-kinase/protein kinase B (PI3K/AKT) pathway, its hyperactivity in the epileptic brain may be highly dependent on the expression of CD44 during KA-induced SE. Moreover, post-surgery brain samples from epileptic patients revealed that nonsclerotic hippocampi exhibit neuronal activation of mTOR whereas, within the context of hippocampal sclerosis in MTLE, mTOR activity is absent in the surviving neurons in damaged regions [232]. However, at the same time, reactive astrocytes in these areas of neuronal loss display significant mTOR activation. In the research with a transgenic mTOR knockout mouse model, the removal of mTOR from reactive astrocytes mitigated the characteristic progressive increase in seizure frequency associated with epileptogenesis and alleviated astrogliosis in the sclerotic hippocampus. Yet, this deletion did not affect the aberrant reorganization of mossy fibers. The mTOR inhibition enhanced the *in vitro* stability of GLT-1, thereby increasing the capacity of astrocytes to clear extracellular glutamate. This suggests that mTOR may regulate GLT-1 stability in astrocytes by preventing its degradation [233]. GLT-1 plays a critical role in maintaining extracellular glutamate at non-toxic levels, and its downregulation in reactive astrocytes can impair inhibitory synaptic transmission during epileptogenesis, contributing to heightened excitability [234, 235]. Consequently, hyperactivation of mTOR in reactive astrocytes may impede glutamate clearance, potentially exacerbating excitability and promoting the progression of temporal lobe epilepsy. A possible explanation for the reduction of GCD in epileptic CD44 AsKO mice could be the absence of CD44 in hippocampal astrocytes resulting in

a disturbed mTORC1 hyperactivation through the CD44/PI3K/AKT/mTOR pathway and consequently non-disturbed extracellular glutamate clearance by a stable GLT-1 protein.

5.4. The influence of astrocytic CD44 depletion on synaptic ultrastructure during epileptogenesis

Perisynaptic astrocytic processes play a key role in surrounding synapses and interacting with dendritic spines and axonal terminals, which helps maintain synaptic structure and function [84, 236, 237]. The communication between neurons and astrocytes is one factor that contributes to the development of epileptic discharges [238]. This study shows that CD44 deletion in astrocytes during epileptogenesis affects the structural connection between astrocytes and synapses, resulting in fewer synapses with astrocyte contacts. This may be partly due to reduced astrogliosis in AsKO mice. Similarly, the absence of Ezrin decreases the proximity between astrocytes and neurons, as well as the number of astrocyte-synapse contacts, leading to increased glutamate overflow and activation of NMDA receptors [215]. Therefore, changes in astrocytic coverage of synapses, driven by CD44 deficiency in CD44 AsKO mice, may be associated with lower synaptic glutamate levels, thereby decelerating seizure progression. In contrast, in CTRL+KA animals, synaptic glutamate levels may increase due to (i) lower GLT-1 levels in reactive astrocytes [239] impairing glutamate reuptake at the synapse and (ii) more astrocyte-synapse contacts, which reduces glutamate spillover outside the synaptic cleft.

My study demonstrated a significant reduction in spine density within the molecular layer of the dentate gyrus in CTRL mice after KA administration, which aligns with earlier findings of a great spine loss in granule cell dendrites during kainate-induced seizures [56]. However, in CD44 AsKO mice, similar spine loss was absent suggesting that the deletion of CD44 in astrocytes may protect against KA-induced synaptic loss in the hippocampus. Additionally, electron microscopy of the epileptic brain has previously revealed degenerated presynaptic profiles partially or fully engulfed by astrocytic processes [55, 240, 241], indicating that seizures could trigger active synaptic phagocytosis by reactive astrocytes. In CD44 AsKO animals, this higher synapse count may reflect reduced synaptic phagocytosis due to the absence of CD44 in astrocytes. The increased dendritic spine density and lowered postsynaptic density size observed in

CD44 knockouts post-seizure further suggest that CD44 deletion may have neuroprotective effects on brain ultrastructure after epilepsy-related trauma. One potential mechanism could be the prevention of the formation of aberrant giant spines, often linked to epileptic damage and thought to compensate for a loss of axonal boutons [56, 242]. However, in the studied knockout animals, that type of giant spines was not observed frequently enough to be statistically significant. Another possibility could be the transition of newly formed, thin, "immature" spines into "mature" mushroom spines, which are crucial for synaptic plasticity and memory formation. Despite this, the results not presented in this dissertation showed no change in the proportion of different dendritic spine shapes in the molecular layer of the dentate gyrus following KA-induced seizures in CD44 AsKO mice [243], indicating that all spine types may benefit equally from CD44 deletion in astrocytes.

6. SUMMARY AND CONCLUSIONS

This research implemented several techniques to determine the role of the CD44 protein in epileptogenesis. Transgenic $CD44^{fl/fl}$ animals provided a base for the *in vivo* study, while the kainate model of *status epilepticus* allowed for the examination of proceeding changes in the epileptic brain – immunohistochemical for structural and three-dimensional serial block-face scanning electron microscopy for the ultrastructural alterations.

Intrahippocampal injections of AAV-mediated vectors with GFAP-driven Cre recombinase generated animals with the astrocytic CD44 knockout in the whole transduced area. Mice with astrocyte-specific CD44 knockout showed fewer spontaneous seizures following kainate-induced *status epilepticus*. However, there was no significant effect on the latency and duration of seizures and average convulsive seizure score. The absence of CD44 influenced astrocyte morphology by reducing reactive astrogliosis during seizures. CD44 AsKO mice exhibited decreased mossy fiber sprouting and granule cell dispersion. CD44 deletion led to an increase in spine number, a reduction of the postsynaptic density size and the astrocytic ensheathment of synapses in the epileptic brain.

The following conclusions can be drawn based on the results of this dissertation:

1) The Cre-loxP system using intrahippocampally injected AAV-mediated vectors with GFAP-driven Cre recombinase provides a sufficient method for studying animals with astrocytic CD44 knockout.

2) The lack of CD44 in astrocytes changes seizure patterns leading to milder phenotypic epileptogenesis symptoms.

3) Astrocytic CD44 knockout reduces structural alterations in astrocytes and neurons in the hippocampus typically observed in temporal lobe epilepsy that may potentially affect seizure progression.

4) Astrocytic deficiency of CD44 in the epileptic hippocampus protects against synaptic loss following seizure activity typical for epileptogenesis.

Overall, the study concludes that astrocytic CD44 plays a critical role in both the development of seizures and the structural changes in the hippocampus during epileptogenesis, suggesting potential therapeutic implications for targeting CD44 in epilepsy.

7. REFERENCES

1. WHO. *Epilepsy*. 2019; Available from: https://www.who.int/news-room/fact-sheets/detail/epilepsy.
2. Fisher, R.S., et al., *ILAE official report: a practical clinical definition of epilepsy.* Epilepsia, 2014. **55**(4): p. 475-82.
3. Aaberg, K.M., et al., Seizures, syndromes, and etiologies in childhood epilepsy: The International League Against Epilepsy 1981, 1989, and 2017 classifications used in a population-based cohort. Epilepsia, 2017. **58**(11): p. 1880-1891.
4. Bosak, M., et al., *Implementation of the new ILAE classification of epilepsies into clinical practice - A cohort study.* Epilepsy Behav, 2019. **96**: p. 28-32.
5. Cloyd, J., et al., *Epidemiological and medical aspects of epilepsy in the elderly.* Epilepsy Res, 2006. **68 Suppl 1**: p. S39-48.
6. Neligan, A., W.A. Hauser, and J.W. Sander, *The epidemiology of the epilepsies.* Handb Clin Neurol, 2012. **107**: p. 113-33.
7. Scheffer, I.E., et al., *ILAE classification of the epilepsies: Position paper of the ILAE Commission for Classification and Terminology.* Epilepsia, 2017. **58**(4): p. 512-521.
8. Kiriakopoulos, E. *Types of Seizures*. Available from: https://www.epilepsy.com/what-is-epilepsy/seizure-types.
9. Wirrell, E.C., et al., *Methodology for classification and definition of epilepsy syndromes with list of syndromes: Report of the ILAE Task Force on Nosology and Definitions.* Epilepsia, 2022. **63**(6): p. 1333-1348.
10. Panebianco, M., A. Rigby, and A.G. Marson, *Vagus nerve stimulation for focal seizures.* Cochrane Database of Systematic Reviews, 2022(7).
11. Bergey, G.K., *Neurostimulation in the treatment of epilepsy.* Experimental Neurology, 2013. **244**: p. 87-95.
12. Rugg-Gunn, F., A. Miserocchi, and A. McEvoy, *Epilepsy surgery.* Pract Neurol, 2020. **20**(1): p. 4-14.
13. Excellence, N.I.f.H.a.C. *Epilepsies in children, young people and adults*. NICE guideline [NG217] 2022 27 April 2022 [cited 2024; Available from: https://www.nice.org.uk/guidance/ng217.
14. Martin-McGill, K.J., et al., *Ketogenic diets for drug-resistant epilepsy.* Cochrane Database of Systematic Reviews, 2020(6).
15. de Boer, H.M., *Epilepsy stigma: Moving from a global problem to global solutions.* Seizure - European Journal of Epilepsy, 2010. **19**(10): p. 630-636.

16. Reilly, C.J., *Attention deficit hyperactivity disorder (ADHD) in childhood epilepsy.* Research in Developmental Disabilities, 2011. **32**(3): p. 883-893.

17. Munger Clary, H.M., et al., *Who is willing to participate in research? A screening model for an anxiety and depression trial in the epilepsy clinic.* Epilepsy Behav, 2020. **104**(Pt A): p. 106907.

18. Kaplan, P.W., *Obsessive-compulsive disorder in chronic epilepsy.* Epilepsy & Behavior, 2011. **22**(3): p. 428-432.

19. Kanner, A.M., et al., *Depression and epilepsy: Epidemiologic and neurobiologic perspectives that may explain their high comorbid occurrence.* Epilepsy & Behavior, 2012. **24**(2): p. 156-168.

20. Boylan, L.S., et al., *Depression but not seizure frequency predicts quality of life in treatment-resistant epilepsy.* Neurology, 2004. **62**(2): p. 258-261.

21. Mula, M. and J.W. Sander, *Suicide risk in people with epilepsy taking antiepileptic drugs.* Bipolar Disorders, 2013. **15**(5): p. 622-627.

22. Bagary, M., *Epilepsy, antiepileptic drugs and suicidality.* Current Opinion in Neurology, 2011. **24**(2).

23. Al-Mufti, F. and J. Claassen, *Neurocritical care: status epilepticus review.* Crit Care Clin, 2014. **30**(4): p. 751-64.

24. Nashef, L., et al., *Unifying the definitions of sudden unexpected death in epilepsy.* Epilepsia, 2012. **53**(2): p. 227-233.

25. Ryvlin, P., L. Nashef, and T. Tomson, *Prevention of sudden unexpected death in epilepsy: A realistic goal?* Epilepsia, 2013. **54**(s2): p. 23-28.

26. Thapaliya, K., et al., *Volumetric differences in hippocampal subfields and associations with clinical measures in myalgic encephalomyelitis/chronic fatigue syndrome.* J Neurosci Res, 2022. **100**(7): p. 1476-1486.

27. *Hippocampus*. Medical dictionary 2011; Available from: https://medicine.en-academic.com/3923/Hippocampus.

28. Moser, E.I., et al., *Grid cells and cortical representation.* Nat Rev Neurosci, 2014. **15**(7): p. 466-81.

29. Y.Z. Pan, P.R., *Membrane Properties and Synaptic Circuitry of CA3 Pyramidal Neurons that Promote Epileptiform Neuronal Synchronization*. Encyclopedia of Basic Epilepsy Research. 2009.

30. Rolls, E.T., *Computational Models of Hippocampal Functions*. Second ed. Learning and Memory: A Comprehensive Reference. 2017.

31. Bartsch, T., et al., *CA1 neurons in the human hippocampus are critical for autobiographical memory, mental time travel, and autonoetic consciousness.* Proceedings of the National Academy of Sciences, 2011. **108**(42): p. 17562-17567.

32. Ji, J. and S. Maren, *Differential roles for hippocampal areas CA1 and CA3 in the contextual encoding and retrieval of extinguished fear.* Learning & Memory, 2008. **15**(4): p. 244-251.

33. O'Mara, S., *The subiculum: what it does, what it might do, and what neuroanatomy has yet to tell us.* Journal of Anatomy, 2005. **207**(3): p. 271-282.

34. Cooper, D.C., S. Chung, and N. Spruston, *Output-Mode Transitions Are Controlled by Prolonged Inactivation of Sodium Channels in Pyramidal Neurons of Subiculum.* PLoS Biology, 2005. **3**(6): p. e175.

35. Jacobs, J., et al., *A sense of direction in human entorhinal cortex.* Proceedings of the National Academy of Sciences, 2010. **107**(14): p. 6487-6492.

36. Bartsch, T. and P. Wulff, *The hippocampus in aging and disease: From plasticity to vulnerability.* Neuroscience, 2015. **309**: p. 1-16.

37. Mufson, E.J., et al., *Hippocampal plasticity during the progression of Alzheimer's disease.* Neuroscience, 2015. **309**: p. 51-67.

38. Cendes, F., et al., *Epilepsies associated with hippocampal sclerosis.* Acta Neuropathol, 2014. **128**(1): p. 21-37.

39. Sloviter, R.S. and A.V. Bumanglag, *Defining "epileptogenesis" and identifying "antiepileptogenic targets" in animal models of acquired temporal lobe epilepsy is not as simple as it might seem.* Neuropharmacology, 2013. **69**: p. 3-15.

40. O'Dell, C.M., et al., *Understanding the basic mechanisms underlying seizures in mesial temporal lobe epilepsy and possible therapeutic targets: a review.* J Neurosci Res, 2012. **90**(5): p. 913-24.

41. Sicotte, N.L., et al., *Regional hippocampal atrophy in multiple sclerosis.* Brain, 2008. **131**(4): p. 1134-1141.

42. Sacco, R., et al., *Cognitive impairment and memory disorders in relapsing-remitting multiple sclerosis: the role of white matter, gray matter and hippocampus.* J Neurol, 2015. **262**(7): p. 1691-7.

43. Wegner, C. and C. Stadelmann, *Gray matter pathology and multiple sclerosis.* Curr Neurol Neurosci Rep, 2009. **9**(5): p. 399-404.

44. Chen, B., et al., *Psychiatric and behavioral side effects of antiepileptic drugs in adults with epilepsy.* Epilepsy Behav, 2017. **76**: p. 24-31.

45. Tian, N., et al., *Active Epilepsy and Seizure Control in Adults - United States, 2013 and 2015.* MMWR Morb Mortal Wkly Rep, 2018. **67**(15): p. 437-442.

46. Tanaka, K., *Temporal Lobe.* International Encyclopedia of the Social & Behavioral Sciences, 2001: p. 15595-15599.

47. Lah, S. and M.L. Smith, *Semantic and episodic memory in children with temporal lobe epilepsy: do they relate to literacy skills?* Neuropsychology, 2014. **28**(1): p. 113-22.

48. Gonzalez Otarula, K.A. and S. Schuele, *Networks in Temporal Lobe Epilepsy.* Neurosurg Clin N Am, 2020. **31**(3): p. 309-317.

49. Charuta Joshi, H.K. *Temporal Lobe Epilepsy (TLE).* Available from: https://www.epilepsy.com/what-is-epilepsy/syndromes/temporal-lobe-epilepsy.

50. Tatum, W.O.t., *Mesial temporal lobe epilepsy.* J Clin Neurophysiol, 2012. **29**(5): p. 356-65.

51. Squire, L.R., *The legacy of patient H.M. for neuroscience.* Neuron, 2009. **61**(1): p. 6-9.

52. Ben-Ari, Y., *Cell death and synaptic reorganizations produced by seizures.* Epilepsia, 2001. **42 Suppl 3**: p. 5-7.

53. Isokawa, M., *Remodeling dendritic spines of dentate granule cells in temporal lobe epilepsy patients and the rat pilocarpine model.* Epilepsia, 2000. **41 Suppl 6**: p. S14-7.

54. Flores-Soto, M., et al., *Pentylenetetrazol-induced seizures in adult rats are associated with plastic changes to the dendritic spines on hippocampal CA1 pyramidal neurons.* Behav Brain Res, 2021. **406**: p. 113198.

55. Witcher, M.R., et al., *Three-dimensional relationships between perisynaptic astroglia and human hippocampal synapses.* Glia, 2010. **58**(5): p. 572-87.

56. Xie, L., et al., *Dynamic alteration of dendrites and dendritic spines in the hippocampus and microglia in mouse brain tissues after kainate-induced status epilepticus.* Int J Neurosci, 2021. **131**(11): p. 1045-1057.

57. Magloczky, Z., et al., *Changes in the distribution and connectivity of interneurons in the epileptic human dentate gyrus.* Neuroscience, 2000. **96**(1): p. 7-25.

58. Borges, K., et al., *Neuronal and glial pathological changes during epileptogenesis in the mouse pilocarpine model.* Exp Neurol, 2003. **182**(1): p. 21-34.

59. Bouilleret, V., et al., *Early loss of interneurons and delayed subunit-specific changes in GABA(A)-receptor expression in a mouse model of mesial temporal lobe epilepsy.* Hippocampus, 2000. **10**(3): p. 305-24.

60. Buckmaster, P.S. and F.E. Dudek, *Neuron loss, granule cell axon reorganization, and functional changes in the dentate gyrus of epileptic kainate-treated rats.* J Comp Neurol, 1997. **385**(3): p. 385-404.

61. Rao, M.S., et al., *Hippocampal neurodegeneration, spontaneous seizures, and mossy fiber sprouting in the F344 rat model of temporal lobe epilepsy.* J Neurosci Res, 2006. **83**(6): p. 1088-105.

62. Blümcke, I., et al., *Defining Clinico-Neuropathological Subtypes of Mesial Temporal Lobe Epilepsy with Hippocampal Sclerosis.* Brain Pathology, 2012. **22**(3): p. 402-411.

63. Hol, E.M. and M. Pekny, *Glial fibrillary acidic protein (GFAP) and the astrocyte intermediate filament system in diseases of the central nervous system.* Curr Opin Cell Biol, 2015. **32**: p. 121-30.

64. Thom, M., *Review: Hippocampal sclerosis in epilepsy: a neuropathology review.* Neuropathol Appl Neurobiol, 2014. **40**(5): p. 520-43.

65. Blümcke, I., et al., *Towards a clinico-pathological classification of granule cell dispersion in human mesial temporal lobe epilepsies.* Acta Neuropathologica, 2009. **117**(5): p. 535-544.

66. Wieser, H.G., *ILAE Commission Report. Mesial Temporal Lobe Epilepsy with Hippocampal Sclerosis.* Epilepsia, 2004. **45**(6): p. 695-714.

67. Cavarsan, C.F., et al., *Is Mossy Fiber Sprouting a Potential Therapeutic Target for Epilepsy?* Front Neurol, 2018. **9**: p. 1023.

68. Benarroch, E.E., *Neuron-Astrocyte Interactions: Partnership for Normal Function and Disease in the Central Nervous System.* Mayo Clinic Proceedings, 2005. **80**(10): p. 1326-1338.

69. Oberheim, N.A., S.A. Goldman, and M. Nedergaard, *Heterogeneity of Astrocytic Form and Function*. 2012, Humana Press. p. 23-45.

70. Ransom, B.R. and C.B. Ransom, *Astrocytes: multitalented stars of the central nervous system.* Methods Mol Biol, 2012. **814**: p. 3-7.

71. Vasile, F., E. Dossi, and N. Rouach, *Human astrocytes: structure and functions in the healthy brain.* Brain Structure and Function, 2017. **222**(5): p. 2017-2029.

72. Verkhratsky, A. and M. Nedergaard, *Physiology of Astroglia.* Physiol Rev, 2018. **98**(1): p. 239-389.

73. Khakh, B.S. and M.V. Sofroniew, *Diversity of astrocyte functions and phenotypes in neural circuits.* Nat Neurosci, 2015. **18**(7): p. 942-52.

74. Cabral-Costa, J.V. and A. Kowaltowski, *Mitochondrial Ca2+ handling as a cell signaling hub: lessons from astrocyte function*. 2022.

75. Halassa, M.M., et al., *Synaptic islands defined by the territory of a single astrocyte.* J Neurosci, 2007. **27**(24): p. 6473-7.

76. Bushong, E.A., et al., *Protoplasmic astrocytes in CA1 stratum radiatum occupy separate anatomical domains.* J Neurosci, 2002. **22**(1): p. 183-92.

77. Xu, H., et al., *Evaluation of neuron-glia integrity by in vivo proton magnetic resonance spectroscopy: Implications for psychiatric disorders.* Neurosci Biobehav Rev, 2016. **71**: p. 563-577.

78. Araque, A., et al., *Tripartite synapses: glia, the unacknowledged partner.* Trends Neurosci, 1999. **22**(5): p. 208-15.

79. Verhoog, Q.P., et al., *Astrocytes as Guardians of Neuronal Excitability: Mechanisms Underlying Epileptogenesis.* Front Neurol, 2020. **11**: p. 591690.

80. Harada, K., T. Kamiya, and T. Tsuboi, *Gliotransmitter Release from Astrocytes: Functional, Developmental, and Pathological Implications in the Brain.* Front Neurosci, 2015. **9**: p. 499.

81. Vezzani, A., et al., *Epilepsy and brain inflammation.* Exp Neurol, 2013. **244**: p. 11-21.

82. Devinsky, O., et al., *Glia and epilepsy: excitability and inflammation.* Trends Neurosci, 2013. **36**(3): p. 174-84.

83. Seifert, G., G. Carmignoto, and C. Steinhauser, *Astrocyte dysfunction in epilepsy.* Brain Res Rev, 2010. **63**(1-2): p. 212-21.

84. Halassa, M.M. and P.G. Haydon, *Integrated brain circuits: astrocytic networks modulate neuronal activity and behavior.* Annu Rev Physiol, 2010. **72**: p. 335-55.

85. Binder, D.K. and C. Steinhauser, *Astrocytes and Epilepsy.* Neurochem Res, 2021. **46**(10): p. 2687-2695.

86. Halassa, M.M., T. Fellin, and P.G. Haydon, *The tripartite synapse: roles for gliotransmission in health and disease.* Trends Mol Med, 2007. **13**(2): p. 54-63.

87. Perea, G., M. Navarrete, and A. Araque, *Tripartite synapses: astrocytes process and control synaptic information.* Trends Neurosci, 2009. **32**(8): p. 421-31.

88. Verkhratsky, A. and M. Nedergaard, *Astroglial cradle in the life of the synapse.* Philosophical Transactions of the Royal Society B: Biological Sciences, 2014. **369**(1654): p. 20130595.

89. Faissner, A., et al., *Contributions of astrocytes to synapse formation and maturation — Potential functions of the perisynaptic extracellular matrix.* Brain Research Reviews, 2010. **63**(1): p. 26-38.

90. Dityatev, A. and D.A. Rusakov, *Molecular signals of plasticity at the tetrapartite synapse.* Current Opinion in Neurobiology, 2011. **21**(2): p. 353-359.

91. Nedergaard, M. and A. Verkhratsky, *Artifact versus reality—How astrocytes contribute to synaptic events.* Glia, 2012. **60**(7): p. 1013-1023.

92. De Leo, J.A., V.L. Tawfik, and M.L. LaCroix-Fralish, *The tetrapartite synapse: Path to CNS sensitization and chronic pain.* PAIN, 2006. **122**(1).

93. Clasadonte, J. and P.G. Haydon, *Astrocytes and Epilepsy*, in *Jasper's Basic Mechanisms of the Epilepsies*, J.L. Noebels, et al., Editors. 2012: Bethesda (MD).

94. Sharma, K., G. Zhang, and S. Li, *Chapter 11 - Astrogliosis and Axonal Regeneration*, in *Neural Regeneration*, K.-F. So and X.-M. Xu, Editors. 2015, Academic Press: Oxford. p. 181-196.

95. Sofroniew, M.V., *Astrogliosis.* Cold Spring Harb Perspect Biol, 2014. **7**(2): p. a020420.

96. Wilhelmsson, U., et al., *Redefining the concept of reactive astrocytes as cells that remain within their unique domains upon reaction to injury.* Proc Natl Acad Sci U S A, 2006. **103**(46): p. 17513-8.

97. Engel, J., *Surgery for Seizures.* New England Journal of Medicine, 1996. **334**(10): p. 647-653.

98. Tian, G.F., et al., *An astrocytic basis of epilepsy.* Nat Med, 2005. **11**(9): p. 973-81.

99. Twible, C., R. Abdo, and Q. Zhang, *Astrocyte Role in Temporal Lobe Epilepsy and Development of Mossy Fiber Sprouting.* Front Cell Neurosci, 2021. **15**: p. 725693.

100. Dzwonek, J. and G.M. Wilczynski, *CD44: molecular interactions, signaling and functions in the nervous system.* Front Cell Neurosci, 2015. **9**: p. 175.

101. Ponta, H., L. Sherman, and P.A. Herrlich, *CD44: from adhesion molecules to signalling regulators.* Nat Rev Mol Cell Biol, 2003. **4**(1): p. 33-45.

102. Weng, X., et al., *The membrane receptor CD44: novel insights into metabolism.* Trends Endocrinol Metab, 2022. **33**(5): p. 318-332.

103. Thorne, R.F., J.W. Legg, and C.M. Isacke, *The role of the CD44 transmembrane and cytoplasmic domains in co-ordinating adhesive and signalling events.* J Cell Sci, 2004. **117**(Pt 3): p. 373-80.

104. Bouvier-Labit, C., et al., *CD44H is expressed by cells of the oligodendrocyte lineage and by oligodendrogliomas in humans.* J Neurooncol, 2002. **60**(2): p. 127-34.

105. Jones, L.L., et al., *Regulation of the cell adhesion molecule CD44 after nerve transection and direct trauma to the mouse brain.* J Comp Neurol, 2000. **426**(3): p. 468-92.

106. Resnick, D.K., et al., *Differential expressions of CD44 variants in tumors affecting the central nervous system.* Mol Diagn, 1999. **4**(3): p. 219-32.

107. Sherman, L., et al., *CD44 expression is aberrant in benign Schwann cell tumors possessing mutations in the neurofibromatosis type 2, but not type 1, gene.* Cancer Res, 1997. **57**(21): p. 4889-97.

108. Kaaijk, P., et al., *Expression of CD44 splice variants in human primary brain tumors.* J Neurooncol, 1995. **26**(3): p. 185-90.

109. Skandalis, S.S., *CD44 Intracellular Domain: A Long Tale of a Short Tail.* Cancers (Basel), 2023. **15**(20).

110. Yu, Q. and I. Stamenkovic, *Localization of matrix metalloproteinase 9 to the cell surface provides a mechanism for CD44-mediated tumor invasion.* Genes Dev, 1999. **13**(1): p. 35-48.

111. Nagano, O. and H. Saya, *Mechanism and biological significance of CD44 cleavage.* Cancer Sci, 2004. **95**(12): p. 930-5.

112. Okamoto, I., et al., *CD44 cleavage induced by a membrane-associated metalloprotease plays a critical role in tumor cell migration.* Oncogene, 1999. **18**(7): p. 1435-46.

113. Martin, T.A., et al., *The role of the CD44/ezrin complex in cancer metastasis.* Crit Rev Oncol Hematol, 2003. **46**(2): p. 165-86.

114. Bourguignon, L.Y., et al., *Hyaluronan-CD44 interaction with IQGAP1 promotes Cdc42 and ERK signaling, leading to actin binding, Elk-1/estrogen receptor transcriptional activation, and ovarian cancer progression.* J Biol Chem, 2005. **280**(12): p. 11961-72.

115. Konopka, A., et al., *Cleavage of Hyaluronan and CD44 Adhesion Molecule Regulate Astrocyte Morphology via Rac1 Signalling.* PLoS One, 2016. **11**(5): p. e0155053.

116. Roszkowska, M., et al., *CD44: a novel synaptic cell adhesion molecule regulating structural and functional plasticity of dendritic spines.* Mol Biol Cell, 2016. **27**(25): p. 4055-4066.

117. Skupien, A., et al., *CD44 regulates dendrite morphogenesis through Src tyrosine kinase-dependent positioning of the Golgi.* J Cell Sci, 2014. **127**(Pt 23): p. 5038-51.

118. Sosunov, A.A., et al., *Phenotypic heterogeneity and plasticity of isocortical and hippocampal astrocytes in the human brain.* J Neurosci, 2014. **34**(6): p. 2285-98.

119. Hassn Mesrati, M., et al., *CD44: A Multifunctional Mediator of Cancer Progression.* Biomolecules, 2021. **11**(12): p. 1850.

120. Duex, J. and D. Theodorescu, *CD44 in Bladder Cancer.* Cancers (Basel), 2024. **16**(6).

121. Ziranu, P., et al., *CD44: A New Prognostic Marker in Colorectal Cancer?* Cancers (Basel), 2024. **16**(8).

122. Weng, X., et al., *Deletion of CD44 promotes adipogenesis by regulating PPARgamma and cell cycle-related pathways.* J Endocrinol, 2024. **262**(1).

123. Sosunov, A.A., et al., *Cytoplasmic vacuolization and ectopic formation of perineuronal nets are characteristic pathologies of cytomegalic neurons in tuberous sclerosis.* J Neuropathol Exp Neurol, 2024.

124. Knittel, J., et al., *A microcarrier-based protocol for scalable generation and purification of human induced pluripotent stem cell-derived neurons and astrocytes.* STAR Protoc, 2022. **3**(3): p. 101632.

125. Zhang, S., et al., *Decellularised spinal cord matrix manipulates glial niche into repairing phase via serglycin-mediated signalling pathway.* Cell Proliferation, 2023. **56**(9).

126. Wang, Q., et al., *The link between neuroinflammation and the neurovascular unit in synucleinopathies.* Sci Adv, 2023. **9**(7): p. eabq1141.

127. Morisaki, Y., et al., *Selective Expression of Osteopontin in ALS-resistant Motor Neurons is a Critical Determinant of Late Phase Neurodegeneration Mediated by Matrix Metalloproteinase-9.* Sci Rep, 2016. **6**: p. 27354.

128. Borges, K., D.L. McDermott, and R. Dingledine, *Reciprocal changes of CD44 and GAP-43 expression in the dentate gyrus inner molecular layer after status epilepticus in mice.* Exp Neurol, 2004. **188**(1): p. 1-10.

129. Bausch, S.B., *Potential roles for hyaluronan and CD44 in kainic acid-induced mossy fiber sprouting in organotypic hippocampal slice cultures.* Neuroscience, 2006. **143**(1): p. 339-50.

130. Akiyama, H., et al., *Morphological diversities of CD44 positive astrocytes in the cerebral cortex of normal subjects and patients with Alzheimer's disease.* Brain Res, 1993. **632**(1-2): p. 249-59.

131. Li, S., H. Shao, and L. Chang, *The Important Role of Perituberal Tissue in Epileptic Patients with Tuberous Sclerosis Complex by the Transcriptome Analysis.* Biomed Res Int, 2020. **2020**: p. 4980609.

132. Razia, R., et al., *Analysis of the expression patterns of AVP, IGF-1, and TNF-α, APP, CD44, IFN-β IFN A β-6, α-syn, and NFL and CLU genes in generalized and focal seizures.* Heliyon, 2024. **10**(14): p. e34912.

133. Sadick, J.S., et al., *Astrocytes and oligodendrocytes undergo subtype-specific transcriptional changes in Alzheimer's disease.* Neuron, 2022. **110**(11): p. 1788-1805 e10.

134. Leng, K., et al., *Molecular characterization of selectively vulnerable neurons in Alzheimer's disease.* Nat Neurosci, 2021. **24**(2): p. 276-287.

135. Cain, A., et al., *Multicellular communities are perturbed in the aging human brain and Alzheimer's disease.* Nat Neurosci, 2023. **26**(7): p. 1267-1280.

136. Girgrah, N., et al., *Localization of the CD44 glycoprotein to fibrous astrocytes in normal white matter and to reactive astrocytes in active lesions in multiple sclerosis.* J Neuropathol Exp Neurol, 1991. **50**(6): p. 779-92.

137. Pinner, E., et al., *CD44 Splice Variants as Potential Players in Alzheimer's Disease Pathology.* J Alzheimers Dis, 2017. **58**(4): p. 1137-1149.

138. Rauramaa, T., et al., *Epilepsy in neuropathologically verified Alzheimer's disease.* Seizure, 2018. **58**: p. 9-12.

139. Lipponen, A., et al., *Analysis of Post-Traumatic Brain Injury Gene Expression Signature Reveals Tubulins, Nfe2l2, Nfkb, Cd44 and S100a4 as Treatment Targets.* Scientific Reports, 2016. **6**(1): p. 31570.

140. Blondiaux, A., et al., *Linking epileptic phenotypes and neural extracellular matrix remodeling signatures in mouse models of epilepsy.* Neurobiol Dis, 2023. **188**: p. 106324.

141. Keck, M., et al., *A systems level analysis of epileptogenesis-associated proteome alterations.* Neurobiol Dis, 2017. **105**: p. 164-178.

142. Tse, K., et al., *The impact of postsynaptic density 95 blocking peptide (Tat-NR2B9c) and an iNOS inhibitor (1400W) on proteomic profile of the hippocampus in C57BL/6J mouse model of kainate-induced epileptogenesis.* J Neurosci Res, 2019. **97**(11): p. 1378-1392.

143. Gama Sosa, M.A., R. De Gasperi, and G.A. Elder, *Animal transgenesis: an overview.* Brain Structure and Function, 2010. **214**(2-3): p. 91-109.

144. Bouabe, H. and K. Okkenhaug, *Gene Targeting in Mice: A Review*. 2013, Humana Press. p. 315-336.

145. Branda, C.S. and S.M. Dymecki, *Talking about a Revolution.* Developmental Cell, 2004. **6**(1): p. 7-28.

146. Nagy, A., *Cre recombinase: the universal reagent for genome tailoring.* Genesis, 2000. **26**(2): p. 99-109.

147. Meinke, G., et al., *Cre Recombinase and Other Tyrosine Recombinases.* Chemical Reviews, 2016. **116**(20): p. 12785-12820.

148. Kim, H., et al., *Mouse Cre-LoxP system: general principles to determine tissue-specific roles of target genes.* Lab Anim Res, 2018. **34**(4): p. 147-159.

149. Brocard, J., et al., *Spatio-temporally controlled site-specific somatic mutagenesis in the mouse.* Proceedings of the National Academy of Sciences, 1997. **94**(26): p. 14559-14563.

150. Metzger, D. and P. Chambon, *Site- and time-specific gene targeting in the mouse.* Methods, 2001. **24**(1): p. 71-80.

151. Indra, A.K., et al., *Temporally-controlled site-specific mutagenesis in the basal layer of the epidermis: comparison of the recombinase activity of the tamoxifen-inducible Cre-ERT and Cre-ERT2 recombinases.* Nucleic Acids Research, 1999. **27**(22): p. 4324-4327.

152. Dong, J.Y., P.D. Fan, and R.A. Frizzell, *Quantitative analysis of the packaging capacity of recombinant adeno-associated virus.* Hum Gene Ther, 1996. **7**(17): p. 2101-12.

153. Chirmule, N., et al., *Immune responses to adenovirus and adeno-associated virus in humans.* Gene Therapy, 1999. **6**(9): p. 1574-1583.

154. McCarty, D.M., S.M. Young, Jr., and R.J. Samulski, *Integration of adeno-associated virus (AAV) and recombinant AAV vectors.* Annu Rev Genet, 2004. **38**: p. 819-45.

155. Deyle, D.R. and D.W. Russell, *Adeno-associated virus vector integration.* Curr Opin Mol Ther, 2009. **11**(4): p. 442-7.

156. Haggerty, D.L., et al., *Adeno-Associated Viral Vectors in Neuroscience Research.* Molecular Therapy - Methods & Clinical Development, 2020. **17**: p. 69-82.

157. Tervo, D.G., et al., *A Designer AAV Variant Permits Efficient Retrograde Access to Projection Neurons.* Neuron, 2016. **92**(2): p. 372-382.

158. Luo, L., E.M. Callaway, and K. Svoboda, *Genetic Dissection of Neural Circuits: A Decade of Progress.* Neuron, 2018. **98**(2): p. 256-281.

159. Abdallah, K., et al., *Adeno-associated virus 2/9 delivery of Cre recombinase in mouse primary afferents.* Scientific Reports, 2018. **8**(1).

160. Lu, Q., et al., *Cre-mediated recombination efficiency and transgene expression patterns of three retinal bipolar cell-expressing Cre transgenic mouse lines.* Mol Vis, 2013. **19**: p. 1310-20.

161. Schauwecker, P.E., *Modulation of cell death by mouse genotype: differential vulnerability to excitatory amino acid-induced lesions.* Exp Neurol, 2002. **178**(2): p. 219-35.

162. Moneta, D., et al., *Somatostatin receptor subtypes 2 and 4 affect seizure susceptibility and hippocampal excitatory neurotransmission in mice.* Eur J Neurosci, 2002. **16**(5): p. 843-9.

163. Riban, V., et al., *Evolution of hippocampal epileptic activity during the development of hippocampal sclerosis in a mouse model of temporal lobe epilepsy.* Neuroscience, 2002. **112**(1): p. 101-11.

164. Groticke, I., K. Hoffmann, and W. Loscher, *Behavioral alterations in a mouse model of temporal lobe epilepsy induced by intrahippocampal injection of kainate.* Exp Neurol, 2008. **213**(1): p. 71-83.

165. Bouilleret, V., et al., *Recurrent seizures and hippocampal sclerosis following intrahippocampal kainate injection in adult mice: electroencephalography, histopathology and synaptic reorganization similar to mesial temporal lobe epilepsy.* Neuroscience, 1999. **89**(3): p. 717-29.

166. Henshall, D.C., *Chapter 35 - Focally Applied Chemoconvulsants*, in *Models of Seizures and Epilepsy (Second Edition)*, A. Pitkänen, et al., Editors. 2017, Academic Press. p. 513-527.

167. Titze, B. and C. Genoud, *Volume scanning electron microscopy for imaging biological ultrastructure.* Biol Cell, 2016. **108**(11): p. 307-323.

168. Denk, W. and H. Horstmann, *Serial block-face scanning electron microscopy to reconstruct three-dimensional tissue nanostructure.* PLoS Biol, 2004. **2**(11): p. e329.

169. Starborg, T., et al., *Using transmission electron microscopy and 3View to determine collagen fibril size and three-dimensional organization.* Nat Protoc, 2013. **8**(7): p. 1433-48.

170. Willingham, M.C. and A.V. Rutherford, *The use of osmium-thiocarbohydrazide-osmium (OTO) and ferrocyanide-reduced osmium methods to enhance membrane contrast and preservation in cultured cells.* J Histochem Cytochem, 1984. **32**(4): p. 455-60.

171. Malick, L.E. and R.B. Wilson, *Modified thiocarbohydrazide procedure for scanning electron microscopy: routine use for normal, pathological, or experimental tissues.* Stain Technol, 1975. **50**(4): p. 265-9.

172. Seligman, A.M., H.L. Wasserkrug, and J.S. Hanker, *A new staining method (OTO) for enhancing contrast of lipid--containing membranes and droplets in osmium tetroxide--fixed tissue with osmiophilic thiocarbohydrazide(TCH).* J Cell Biol, 1966. **30**(2): p. 424-32.

173. Staeubli, W., *A new embedding technique for electron microscopy, combining a water-soluble epoxy resin (Durcupan) with water-insoluble Araldite.* J Cell Biol, 1963. **16**(1): p. 197-201.

174. Chaffey, N., *Hayat MA. 2000. Principles and techniques of electron microscopy: biological applications. 4th edn. 543pp. Cambridge: Cambridge University Press. {pound}65 (hardback).* Annals of Botany, 2001. **87**.

175. Shatirishvili, M., et al., *Epidermal-specific deletion of CD44 reveals a function in keratinocytes in response to mechanical stress.* Cell Death Dis, 2016. **7**(11): p. e2461.

176. Brenner, M., *Structure and Transcriptional Regulation of the GFAP Gene.* Brain Pathology, 1994. **4**(3): p. 245-257.

177. Brenner, M., et al., *GFAP promoter directs astrocyte-specific expression in transgenic mice.* The Journal of Neuroscience, 1994. **14**(3): p. 1030-1037.

178. Ganat, Y.M., et al., *Early Postnatal Astroglial Cells Produce Multilineage Precursors and Neural Stem CellsIn Vivo.* The Journal of Neuroscience, 2006. **26**(33): p. 8609-8621.

179. Lee, Y., et al., *GFAP promoter elements required for region-specific and astrocyte-specific expression.* Glia, 2008. **56**(5): p. 481-93.

180. Racine, R.J., *Modification of seizure activity by electrical stimulation. II. Motor seizure.* Electroencephalogr Clin Neurophysiol, 1972. **32**(3): p. 281-94.

181. Schauwecker, P.E. and O. Steward, *Genetic determinants of susceptibility to excitotoxic cell death: Implications for gene targeting approaches.* Proceedings of the National Academy of Sciences of the United States of America, 1997. **94**(8): p. 4103-4108.

182. Ndode-Ekane, X.E. and A. Pitkanen, *Urokinase-type plasminogen activator receptor modulates epileptogenesis in mouse model of temporal lobe epilepsy.* Mol Neurobiol, 2013. **47**(3): p. 914-37.

183. Hagihara, H., et al., *Dissection of Hippocampal Dentate Gyrus from Adult Mouse.* Journal of Visualized Experiments, 2009(33).

184. Laemmli, U.K., *Cleavage of structural proteins during the assembly of the head of bacteriophage T4.* Nature, 1970. **227**(5259): p. 680-5.

185. Ohgane, K. and H. Yoshioka, *Quantification of Gel Bands by an Image J Macro, Band/Peak Quantification Tool.* protocols.io, 2019.

186. Schindelin, J., et al., *Fiji: an open-source platform for biological-image analysis.* Nature Methods, 2012. **9**(7): p. 676-682.

187. Kimelberg, H.K., *The problem of astrocyte identity.* Neurochem Int, 2004. **45**(2-3): p. 191-202.

188. Torres-Ceja, B. and M.L. Olsen, *A closer look at astrocyte morphology: Development, heterogeneity, and plasticity at astrocyte leaflets.* Curr Opin Neurobiol, 2022. **74**: p. 102550.

189. Hosford, B.E., J.P. Liska, and S.C. Danzer, *Ablation of Newly Generated Hippocampal Granule Cells Has Disease-Modifying Effects in Epilepsy.* J Neurosci, 2016. **36**(43): p. 11013-11023.

190. Danzer, S.C., et al., *Altered morphology of hippocampal dentate granule cell presynaptic and postsynaptic terminals following conditional deletion of TrkB.* Hippocampus, 2008. **18**(7): p. 668-678.

191. Deerinck, T.J., et al., *NCMIR methods for 3D EM: A new protocol for preparation of biological specimens for serial block face scanning electron microscopy*. Microscopy, 2010. **6-8**.

192. Belevich, I., et al., *Microscopy Image Browser: A Platform for Segmentation and Analysis of Multidimensional Datasets.* PLoS Biol, 2016. **14**(1): p. e1002340.

193. Fiala, J.C., *Reconstruct: a free editor for serial section microscopy.* J Microsc, 2005. **218**(Pt 1): p. 52-61.

194. Fiala, J.C. and K.M. Harris, *Extending unbiased stereology of brain ultrastructure to three-dimensional volumes.* J Am Med Inform Assoc, 2001. **8**(1): p. 1-16.

195. Ostroff, L.E., et al., *Synapses lacking astrocyte appear in the amygdala during consolidation of Pavlovian threat conditioning.* J Comp Neurol, 2014. **522**(9): p. 2152-63.

196. Keck, M., et al., *Proteomic profiling of epileptogenesis in a rat model: Focus on cell stress, extracellular matrix and angiogenesis.* Neurobiol Dis, 2018. **112**: p. 119-135.

197. Represa, A., et al., *Epilepsy induced collateral sprouting of hippocampal mossy fibers: does it induce the development of ectopic synapses with granule cell dendrites?* Hippocampus, 1993. **3**(3): p. 257-68.

198. Sloviter, R.S., et al., *Kainic acid-induced recurrent mossy fiber innervation of dentate gyrus inhibitory interneurons: possible anatomical substrate of granule cell hyper-inhibition in chronically epileptic rats.* J Comp Neurol, 2006. **494**(6): p. 944-60.

199. Schmidt, E.E., et al., *Illegitimate Cre-dependent chromosome rearrangements in transgenic mouse spermatids.* Proc Natl Acad Sci U S A, 2000. **97**(25): p. 13702-7.

200. Heffner, C.S., et al., *Supporting conditional mouse mutagenesis with a comprehensive cre characterization resource.* Nat Commun, 2012. **3**: p. 1218.

201. Harno, E., Elizabeth C. Cottrell, and A. White, *Metabolic Pitfalls of CNS Cre-Based Technology.* Cell Metabolism, 2013. **18**(1): p. 21-28.

202. Gil-Sanz, C., et al., *Lineage Tracing Using Cux2-Cre and Cux2-CreERT2 Mice.* Neuron, 2015. **86**(4): p. 1091-1099.

203. Song, A.J. and R.D. Palmiter, *Detecting and Avoiding Problems When Using the Cre–lox System.* Trends in Genetics, 2018. **34**(5): p. 333-340.

204. Rezai Amin, S., et al., *Viral vector-mediated Cre recombinase expression in substantia nigra induces lesions of the nigrostriatal pathway associated with perturbations of dopamine-related behaviors and hallmarks of programmed cell death.* J Neurochem, 2019. **150**(3): p. 330-340.

205. Ortinski, P.I., et al., *Selective induction of astrocytic gliosis generates deficits in neuronal inhibition.* Nature Neuroscience, 2010. **13**(5): p. 584-591.

206. Su, M., et al., *Expression specificity of GFAP transgenes.* Neurochem Res, 2004. **29**(11): p. 2075-93.

207. Jessberger, S. and J.M. Parent, *Epilepsy and Adult Neurogenesis.* Cold Spring Harb Perspect Biol, 2015. **7**(12).

208. Sierra, A., et al., *Neuronal hyperactivity accelerates depletion of neural stem cells and impairs hippocampal neurogenesis.* Cell Stem Cell, 2015. **16**(5): p. 488-503.

209. Fukuda, S., et al., *Two distinct subpopulations of nestin-positive cells in adult mouse dentate gyrus.* J Neurosci, 2003. **23**(28): p. 9357-66.

210. Bonde, S., C.T. Ekdahl, and O. Lindvall, *Long-term neuronal replacement in adult rat hippocampus after status epilepticus despite chronic inflammation.* Eur J Neurosci, 2006. **23**(4): p. 965-74.

211. Sosunov, A.A., et al., *Phenotypic Conversions of "Protoplasmic" to "Reactive" Astrocytes in Alexander Disease.* The Journal of Neuroscience, 2013. **33**(17): p. 7439-7450.

212. Arai, Y., S. Takashima, and L.E. Becker, *CD44 expression in tuberous sclerosis.* Pathobiology, 2000. **68**(2): p. 87-92.

213. Stylli, S.S., A.H. Kaye, and U. Novak, *Induction of CD44 expression in stab wounds of the brain: long term persistence of CD44 expression.* Journal of Clinical Neuroscience, 2000. **7**(2): p. 137-140.

214. Wenzel, H.J., et al., *Kainic acid-induced mossy fiber sprouting and synapse formation in the dentate gyrus of rats.* Hippocampus, 2000. **10**(3): p. 244-260.

215. Badia-Soteras, A., et al., *Retraction of Astrocyte Leaflets From the Synapse Enhances Fear Memory.* Biological Psychiatry, 2023. **94**(3): p. 226-238.

216. Kovács, Z., et al., *Putrescine Intensifies Glu/GABA Exchange Mechanism and Promotes Early Termination of Seizures.* International Journal of Molecular Sciences, 2022. **23**(15): p. 8191.

217. Kovács, Z., et al., *Critical Role of Astrocytic Polyamine and GABA Metabolism in Epileptogenesis.* Frontiers in Cellular Neuroscience, 2022. **15**.

218. Héja, L., et al., *Glutamate Uptake Triggers Transporter-Mediated GABA Release from Astrocytes.* PLoS ONE, 2009. **4**(9): p. e7153.

219. Robel, S., et al., *Reactive Astrogliosis Causes the Development of Spontaneous Seizures.* The Journal of Neuroscience, 2015. **35**(8): p. 3330-3345.

220. Blumcke, I., et al., *A distinct variant of focal cortical dysplasia type I characterised by magnetic resonance imaging and neuropathological examination in children with severe epilepsies.* Epileptic Disord, 2010. **12**(3): p. 172-80.

221. Lurton, D., et al., *Granule cell dispersion is correlated with early epileptic events in human temporal lobe epilepsy.* Journal of the Neurological Sciences, 1998. **154**(2): p. 133-136.

222. Patel, L.S., H.J. Wenzel, and P.A. Schwartzkroin, *Physiological and morphological characterization of dentate granule cells in the p35 knock-out mouse hippocampus: evidence for an epileptic circuit.* J Neurosci, 2004. **24**(41): p. 9005-14.

223. Wenzel, H.J., et al., *Abnormal morphological and functional organization of the hippocampus in a p35 mutant model of cortical dysplasia associated with spontaneous seizures.* J Neurosci, 2001. **21**(3): p. 983-98.

224. Volz, F., et al., *Stereologic estimation of hippocampal GluR2/3- and calretinin-immunoreactive hilar neurons (presumptive mossy cells) in two mouse models of temporal lobe epilepsy.* Epilepsia, 2011. **52**(9): p. 1579-89.

225. Zhang, J., et al., *Activation of the mTOR pathway promotes neurite growth through upregulation of CD44 expression.* J Int Med Res, 2023. **51**(6): p. 3000605231178510.

226. Xu, J.T., et al., *Expression and distribution of mTOR, p70S6K, 4E-BP1, and their phosphorylated counterparts in rat dorsal root ganglion and spinal cord dorsal horn.* Brain Res, 2010. **1336**: p. 46-57.

227. Codeluppi, S., et al., *The Rheb-mTOR pathway is upregulated in reactive astrocytes of the injured spinal cord.* J Neurosci, 2009. **29**(4): p. 1093-104.

228. Devinsky, O., et al., *Epilepsy.* Nature Reviews Disease Primers, 2018. **4**(1): p. 18024.

229. Kim, S.R., *Control of Granule Cell Dispersion by Natural Materials Such as Eugenol and Naringin: A Potential Therapeutic Strategy Against Temporal Lobe Epilepsy.* J Med Food, 2016. **19**(8): p. 730-6.

230. Leem, E., et al., *Inhibition of Granule Cell Dispersion and Seizure Development by Astrocyte Elevated Gene-1 in a Mouse Model of Temporal Lobe Epilepsy.* Biomolecules, 2024. **14**(3).

231. Jang, H., K.H. Jeong, and S.R. Kim, *Naringin attenuates granule cell dispersion in the dentate gyrus in a mouse model of temporal lobe epilepsy.* Epilepsy Res, 2016. **123**: p. 6-10.

232. Sosunov, A.A., et al., *The mTOR pathway is activated in glial cells in mesial temporal sclerosis.* Epilepsia, 2012. **53 Suppl 1**: p. 78-86.

233. Wang, X., et al., *Deletion of mTOR in Reactive Astrocytes Suppresses Chronic Seizures in a Mouse Model of Temporal Lobe Epilepsy.* Mol Neurobiol, 2017. **54**(1): p. 175-187.

234. Regan, M.R., et al., *Variations in promoter activity reveal a differential expression and physiology of glutamate transporters by glia in the developing and mature CNS.* J Neurosci, 2007. **27**(25): p. 6607-19.

235. Petr, G.T., et al., *Conditional deletion of the glutamate transporter GLT-1 reveals that astrocytic GLT-1 protects against fatal epilepsy while neuronal GLT-1 contributes significantly to glutamate uptake into synaptosomes.* J Neurosci, 2015. **35**(13): p. 5187-201.

236. Bernardinelli, Y., D. Muller, and I. Nikonenko, *Astrocyte-Synapse Structural Plasticity.* Neural Plasticity, 2014. **2014**: p. 1-13.

237. Araque, A., et al., *Gliotransmitters travel in time and space.* Neuron, 2014. **81**(4): p. 728-39.

238. Gómez-Gonzalo, M., et al., *An Excitatory Loop with Astrocytes Contributes to Drive Neurons to Seizure Threshold.* PLoS Biology, 2010. **8**(4): p. e1000352.

239. Price, B.R., L.A. Johnson, and C.M. Norris, *Reactive astrocytes: The nexus of pathological and clinical hallmarks of Alzheimer's disease.* Ageing Res Rev, 2021. **68**: p. 101335.

240. Clarkson, C., et al., *Ultrastructural and functional changes at the tripartite synapse during epileptogenesis in a model of temporal lobe epilepsy.* Exp Neurol, 2020. **326**: p. 113196.

241. Zhvania, M.G., et al., *Ultrastructural changes to rat hippocampus in pentylenetetrazol- and kainic acid-induced status epilepticus: A study using electron microscopy.* Micron, 2015. **74**: p. 22-9.

242. Fiala, J.C., J. Spacek, and K.M. Harris, *Dendritic Spine Pathology: Cause or Consequence of Neurological Disorders?* Brain Research Reviews, 2002. **39**(1): p. 29-54.

243. Kruk, P.K., et al., *Astrocytic CD44 Deficiency Reduces the Severity of Kainate-Induced Epilepsy.* Cells, 2023. **12**(11).

8. LIST OF FIGURES

9. LIST OF TABLES

10. SUPPLEMENTARY INFORMATION

10.1. Author's publications

Siemieniec, J. & **Kruk, P.K.**, *Synthesis of silver and gold nanoparticles using methods of green chemistry*. Chemik, 2013. **67**(10): 842–847.

Figiel, I. & **Kruk, P.K.**; Zaręba-Kozioł, M.; Rybak, P.; Bijata, M.; Wlodarczyk, J.; Dzwonek, J., *MMP-9 Signaling Pathways That Engage Rho GTPases in Brain Plasticity*. Cells, 2021. **10**(1): 166. https://doi.org/10.3390/cells10010166

Part of this dissertation's results was published in:

Kruk, P.K., Nader, K., Skupien-Jaroszek, A., Wójtowicz, T., Buszka, A., Olech-Kochanczyk, G., Wilczynski, G.M., Worch, R., Kalita, K., Włodarczyk, J., Dzwonek, J., *Astrocytic CD44 Deficiency Reduces the Severity of Kainate-Induced Epilepsy*. Cells, 2023. **12**(1483). https://doi.org/10.3390/cells12111483